(12) INTERNATIONAL APPLICATION PUBLISHED UNDER THE PATENT COOPERATION TREATY (PCT)

(19) **World Intellectual Property Organization**
International Bureau

(43) **International Publication Date**
22 January 2026 (22.01.2026)

WIPO | PCT

(10) **International Publication Number**
WO 2026/020152 A1

(51) International Patent Classification:
G06N 10/40 (2022.01) *G06N 10/20* (2022.01)
B82Y 10/00 (2011.01)

(21) International Application Number:
PCT/US2025/038342

(22) International Filing Date:
18 July 2025 (18.07.2025)

(25) Filing Language: English

(26) Publication Language: English

(30) Priority Data:
63/673,370 19 July 2024 (19.07.2024) US

(71) Applicants: YALE UNIVERSITY [US/US]; Two Whitney Avenue, New Haven, Connecticut 06510 (US). **UNIVERSITY OF MICHIGAN** [US/US]; 1109 Geddes Avenue, Ann Arbor, Michigan 48109 (US). **UNIVERSITY OF CONNECTICUT** [US/US]; 233 Glenbrook Road, Unit 4100, Storrs, Connecticut 06269 (US).

(72) Inventors: CORTINAS, Rodrigo; c/o Yale Ventures, 101 College Street, New Haven, Connecticut 06519 (US). **SCHAEFER, Max**; c/o Yale Ventures, 101 College Street, New Haven, Connecticut 06519 (US). **DE ALBORNOZ, Alejandro Cros Carrillo**; c/o Yale Ventures, 101 College Street, New Haven, Connecticut 06519 (US). **BATISTA, Victor**; c/o Yale Ventures, 101 College Street, New Haven, Connecticut 06519 (US). **CABRAL, Delmar Guido Azevedo**; c/o Yale Ventures, 101 College Street, New Haven, Connecticut 06519 (US). **VIDELA, Pablo**; c/o Yale Ventures, 101 College Street, New Haven, Connecticut 06519 (US). **ALLEN, Brandon**; c/o Yale Ventures, 101 College Street, New Haven, Connecticut 06519 (US). **GEVA, Eitan**; c/o University of Michigan, 1109 Geddes Avenue, Ann Arbor, Michigan 48109 (US). **KHAZAEI, Pouva**; c/o University of Michigan, 1109 Geddes Avenue, Ann Arbor, Michigan 48109 (US). **DOS SANTOS, Lea Ferreira**; c/o University of Connecticut, 233 Glenbrook Road, Unit 4100, Storrs, Connecticut 06269 (US).

(74) Agent: RITCHIE, Sean P. et al.; Saul Ewing LLP, 1200 Liberty Ridge Drive, Suite 200, Wayne, Pennsylvania 19087-5569 (US).

(81) Designated States *(unless otherwise indicated, for every kind of national protection available)*: AE, AG, AL, AM, AO, AT, AU, AZ, BA, BB, BG, BH, BN, BR, BW, BY, BZ, CA, CH, CL, CN, CO, CR, CU, CV, CZ, DE, DJ, DK, DM, DO, DZ, EC, EE, EG, ES, FI, GB, GD, GE, GH, GM, GT, HN, HR, HU, ID, IL, IN, IQ, IR, IS, IT, JM, JO, JP, KE, KG, KH, KN, KP, KR, KW, KZ, LA, LC, LK, LR, LS, LU, LY, MA, MD, MG, MK, MN, MU, MW, MX, MY, MZ, NA, NG, NI, NO, NZ, OM, PA, PE, PG, PH, PL, PT, QA, RO, RS, RU, RW, SA, SC, SD, SE, SG, SK, SL, ST, SV, SY, TH, TJ, TM, TN, TR, TT, TZ, UA, UG, US, UY, UZ, VC, VN, WS, ZA, ZM, ZW.

(84) Designated States *(unless otherwise indicated, for every kind of regional protection available)*: ARIPO (BW, CV, GH, GM, KE, LR, LS, MW, MZ, NA, RW, SC, SD, SL, ST, SZ, TZ, UG, ZM, ZW), Eurasian (AM, AZ, BY, KG, KZ, RU, TJ, TM), European (AL, AT, BE, BG, CH, CY, CZ, DE, DK, EE, ES, FI, FR, GB, GR, HR, HU, IE, IS, IT, LT, LU, LV, MC, ME, MK, MT, NL, NO, PL, PT, RO, RS, SE,

(54) Title: ARTICLES AND METHODS FOR SINGLE-TRANSMON PARAMETRIC SIMULATION OF QUANTUM CHEMICAL DOUBLE WELLS

(57) Abstract: Provided herein is a device for generating an asymmetric double well system. The device includes an oscillator; a parametric drive arranged and disposed to bifurcate the oscillator, creating a static effective double well; and an additive drive arranged and disposed to create an asymmetry between the wells. Also provided herein is a method of generating a double well system using the device.

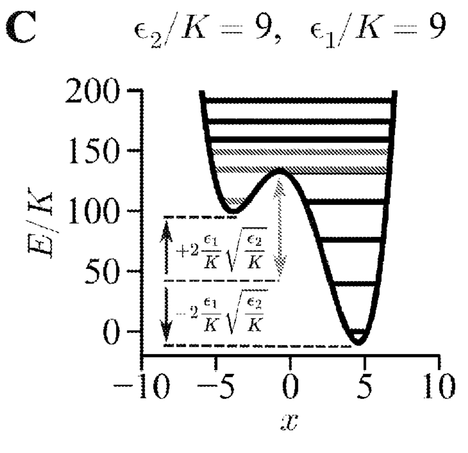

FIG. 2C

WO 2026/020152 A1

[Continued on next page]

SI, SK, SM, TR), OAPI (BF, BJ, CF, CG, CI, CM, GA, GN,
GQ, GW, KM, ML, MR, NE, SN, TD, TG).

Published:

— *with international search report (Art. 21(3))*

ARTICLES AND METHODS FOR SINGLE-TRANSMON PARAMETRIC SIMULATION OF QUANTUM CHEMICAL DOUBLE WELLS

CROSS-REFERENCE TO RELATED APPLICATIONS

The present application claims priority under 35 U.S.C. § 119(e) to U.S. Provisional Patent Application No. 63/673,370, filed July 19, 2024, which application is incorporated herein by reference in its entirety.

STATEMENT REGARDING FEDERALLY SPONSORED RESEARCH OR DEVELOPMENT

This invention was made with government support under grants 2302908 and 2124511 awarded by National Science Foundation (NSF). The government has certain rights in the invention.

BACKGROUND OF THE INVENTION

The Kerr parametric oscillator, a nonlinear oscillator made bi-stable by a parametric drive, is an elementary quantum optical model that has continuously received attention for decades because, despite its simplicity, it is surprisingly rich. In the early 1990s it was predicted that this system should exhibit quantum tunnelling between the two stable points, opening a pathway to engineer a highly controllable simulator for the physics involved in quantum chemistry, nuclear structure, two-level systems and other problems involving a double well energy surface. The physical implementation of such a promising model was, however, challenging and experiments in the quantum regime have been realized only recently.

Accordingly, there remains a need in the art for articles and methods that improve upon existing articles and methods for modeling chemical reactions in the quantum regime. The present disclosure meets this need.

SUMMARY

In one aspect, a device for generating an asymmetric double well system includes an oscillator; a parametric drive arranged and disposed to bifurcate the oscillator, creating a static effective double well; and an additive drive arranged and disposed to create an asymmetry between the wells.

In some embodiments, the oscillator is non-linear. In some embodiments, the oscillator is a transmon oscillator. In some embodiments, the transmon oscillator comprises two superconducting nonlinear asymmetric inductive elements (SNAILs) shunted by a capacitor.

In some embodiments, an asymmetry of the wells is controlled by ϵ_1. In some embodiments, $|\epsilon_1| = \frac{\Omega_1}{2}$; where Ω_1 is the amplitude of the additive drive. In some embodiments, a depth of the wells is controlled by ϵ_2. In some embodiments, $\epsilon_2 = g_3 \frac{4\Omega_2}{3\omega_a}$; where g_3 is the third-order non-linearity of the circuit; Ω_2 is the amplitude of the parametric drive; ω_a is the renormalized oscillator resonance frequency, which is Lamb- and Stark-shifted from ω_0; and ω_0 is the bare resonance frequency of the oscillator.

In some embodiments, the additive drive, the parametric drive, and the oscillator together form a continuously tunable asymmetric Kerr parametric oscillator.

In another aspect, a method of generating a double well system includes providing the device according to any of the embodiments disclosed herein, driving the oscillator with the parametric drive, the parametric drive bifurcating the oscillator and creating an effective double well; and driving the oscillator with an additive drive, the additive drive creating an asymmetry between the wells.

In some embodiments, a barrier height of the asymmetric double well is continuously tunable. In some embodiments, tuning the barrier height comprises adjusting ϵ_2 according to the equation $\epsilon_2 = g_3 \frac{4\Omega_2}{3\omega_a}$; where g_3 is the third-order non-linearity of the circuit; Ω_2 is the amplitude of the parametric drive; ω_a is the renormalized oscillator resonance frequency, which is Lamb- and Stark-shifted from ω_0; and ω_0 is the bare resonance frequency of the oscillator.

In some embodiments, the asymmetry of the asymmetric double well is continuously tunable. In some embodiments, tuning the asymmetry comprises adjusting ϵ_1 according to the equation $|\epsilon_1| = \frac{\Omega_1}{2}$; where Ω_1 is the amplitude of the additive drive.

In some embodiments, an activation of the system exhibits pronounced quantum resonances whole width alternates with both the depth and the asymmetry of the wells. In some embodiments, the asymmetric double well experiences an increased activation time from one well to the other as compared to a symmetric double well. In some embodiments, the asymmetric double well experiences the increased activation time when the system is initialized in a shallower well.

In some embodiments, the driven double well system simulates a static system. In some embodiments, the oscillator is non-linear and driven in the quantum regime.

In some embodiments, the method further includes modeling the dynamics of a chemical reaction with the asymmetric double-well. In some embodiments, the double-well comprises a Hamiltonian according to the equation:

$$\hat{H}_{DW} = \frac{\hat{p}^2}{2m} + k_4\hat{x}^4 - k_2\hat{x}^2 + k_1\hat{x}$$

where $\hat{x}$ is a position operator associated with motion along a reaction coordinate; $\hat{p}$ is a momentum operator associated with motion along the reaction coordinate; m is the mass associated with the motion along the reaction coordinate; and $\{k_1, k_2, k_4\}$ are positive and real parameters whose values define the double well free energy profile; and wherein $\hat{x}$ and $\hat{p}$ satisfy the equation $[\hat{x}, \hat{p}] = i\hbar$.

In some embodiments, the method further includes fitting the Hamiltonian to a fourth-order polynomial according to the equation:

$$V(x) = k_4x^4 - k_2x^2 + k_1x$$

where $k_4x^4 - k_2x^2$ relates to obtaining the double-well feature; and k_1x accounts for asymmetry between reactant and product wells.

In some embodiments, the method further includes mapping a Hamiltonian of a Kerr-Cat device onto the double-well Hamiltonian, the Kerr-Cat device Hamiltonian having the equation:

$$\hat{H}_{KC} = \Delta\hat{a}^\dagger\hat{a} - K(\hat{a}^\dagger)^2(\hat{a})^2 + \epsilon_2(\hat{a}^2 + \hat{a}^{\dagger 2}) + \epsilon_1(\hat{a} + \hat{a}^\dagger)$$

where $\hat{a}^\dagger$ and $\hat{a}$ are the device's ladder operators, associated with excitations and de-excitations, respectively, between the device's effective energy levels; K is the Kerr non-linearity; Δ is the detuning; and ϵ_1 and ϵ_2 are drive coefficients; and wherein $\hat{a}^\dagger$ and $\hat{a}$ satisfy the equation $[\hat{a}, \hat{a}^\dagger] = 1$. In some embodiments, the mapping of the Kerr-Cat device Hamiltonian onto the double-well Hamiltonian comprises mapping photonic operators $\{\hat{a}, \hat{a}^\dagger\}$ onto operators associated with motion along a reaction coordinate $\{\hat{x}, \hat{p}\}$ according to the equations:

$$\hat{a} = \frac{1}{\sqrt{2}}\left(\frac{1}{c}\hat{x} + \frac{ic}{\hbar}\hat{p}\right) \; ; \; \hat{a}^\dagger = \frac{1}{\sqrt{2}}\left(\frac{1}{c}\hat{x} - \frac{ic}{\hbar}\hat{p}\right)$$

$$\hat{x} = \frac{c}{\sqrt{2}}(\hat{a} + \hat{a}^\dagger) \ ; \ \hat{p} = \frac{\hbar}{i\sqrt{2}c}(\hat{a} - \hat{a}^\dagger);$$

where c is a constant parameter that has units of length.

In some embodiments, the method further includes recasting a negative of the Kerr-Cat Hamiltonian in terms of the $\hat{x}$ and $\hat{p}$ according to the following equation:

$$-\hat{H}_{KC} = \frac{c^2}{\hbar^2}(\epsilon_2 - K - \Delta/2)\hat{p}^2 + \frac{K}{4c^4}\hat{x}^4 - \frac{1}{c^2}(\epsilon_2 + K + \Delta/2)\hat{x}^2 - \frac{\epsilon_1\sqrt{2}}{c}\hat{x} + \frac{Kc^4}{4\hbar^4}\hat{p}^4 + \frac{K}{4\hbar^2}\hat{x}^2\hat{p}^2 + \frac{K}{4\hbar^2}\hat{p}^2\hat{x}^2$$

where $\hat{a}^\dagger$ and $\hat{a}$ are the device's ladder operators, associated with excitations and de-excitations, respectively, between the device's effective energy levels; K is the Kerr non-linearity; Δ is the detuning; and ϵ_1 and ϵ_2 are drive coefficients; and wherein $\hat{a}^\dagger$ and $\hat{a}$ satisfy the equation $[\hat{a}, \hat{a}^\dagger] = 1$.

In some embodiments, the method further includes mapping $\{\Delta, K, \epsilon_1, \epsilon_2\}$ onto $\{m, k_1, k_2, k_4\}$ using the following mapping relations:

$$K = 4c^4 k_4;$$

$$\epsilon_2 = \frac{\hbar^2 + 2c^4 k_2 m}{4c^2 m};$$

$$\Delta = \frac{2c^4 k_2 m - \hbar^2 - 16c^6 k_4 m}{2c^2 m}; \text{ and}$$

$$\epsilon_1 = \frac{c k_1}{\sqrt{2}}.$$

In some embodiments, c is selected to satisfy the following inequality:

$$\frac{\hbar^2}{m k_2 c^4} \gg 1.$$

BRIEF DESCRIPTION OF THE DRAWINGS

For a fuller understanding of the nature and desired objects of the present invention, reference is made to the following detailed description taken in conjunction with the accompanying drawing figures wherein like reference characters denote corresponding parts throughout the several views.

FIGS. 1A-D show images illustrating oscillators according to an embodiment of the disclosure. **A** Rendering of the half-aluminum, half-copper sample package containing two

Sapphire chips magnified in **B.** Each chip has a SNAIL-transmon, readout resonator, and Purcell filter. Applying a strong microwave drive at $\omega_2 \approx 2\omega_a$ transforms the SNAIL-transmon Hamiltonian into the parametric oscillator Hamiltonian. **C** Schematic of the SNAIL-transmon: a two-SNAIL array serves as the nonlinear element. The capacitor pads are shifted with respect to the axis of the array to couple it to the readout resonator. **D** Scanning electron micrograph of the two-SNAIL array. The SNAIL loops are biased with an external magnetic flux $\Phi/\Phi_0 = 0.31$, where Φ_0 is the magnetic flux quantum.

FIGS. 2A-D show graphs illustrating potential energies and spectrum of the parametric oscillator Hamiltonians of various double-wells. **A** Shows the semiclassical double well potential energy $V(x)$ and with the allowed quantum energies E/K obtained from the diagonalization of the parametric oscillator Hamiltonian. **B** Shows the spectrum of the parametric oscillator Hamiltonian as a function of ϵ_2 controlling the barrier height. **C** Shows the semiclassical double well potential energy for the asymmetric case and the Hamiltonian energies, and **D** shows the spectrum as a function of ϵ_1 controlling the asymmetry.

FIGS. 3A-B show graphs illustrating population dynamics. **A** Experimental population dynamics when initializing the system in the shallower well. The probability of survival P_{up} drops exponentially. The dashed line represents the half-lifetime of the state. Resonances with characteristic widths are apparent. Note that the half-lifetime at finite asymmetry ($\epsilon_1/K \approx 1$) is larger than for the symmetric case. Data is collected up to 900 μs (see SM). **B** Theory calculation modeling the experiment. The theory plot is obtained from independent calibration of all Hamiltonian parameters ($\omega_a, \epsilon_2, \epsilon_1$, and K). Without free parameters, the agreement between Hamiltonian theory and experiment is remarkable. The shift between the resonances is consistent with a 5% uncertainty in the calibration of ϵ_1/K and ϵ_2/K (see SM). Note the discrepancy in the Lindbladian timescale.

FIGS. 4A-C show graphs illustrating **A** Semiclassical Hamiltonian prediction for the resonance conditions (parabolic dashed lines) and Bohr's quantization condition for n and m allowed quantum orbits in the small (orange) and large (blue) lemniscate's lobes. The red circles mark tripe intersections labeled (n, m). **B** Measurement of activation time T as a function of ϵ_2/K (controlling the barrier height) and ϵ_1/K (controlling the asymmetry). The color scale is linear. **C** Theory prediction from a Lindbladian model including single photon loss and gain. The color scale is logarithmic. The green-black dashed lines shows the maxima of T at each value of ϵ_2/K.

FIGS. 5A-B show graphs illustrating experiment **A** and theory **B** for the activation time T as a function of ϵ_2/K, effectively controlling the barrier height. The symmetric case ($\epsilon_1 = 0$) is modulated by resonances in the quantized energies. Exploiting asymmetry, it is possible to avoid these resonances and substantially increase the activation time. The asymmetric optimum corresponds to the green-black dashed line in FIG. 4.

FIG. 6 shows a graph illustrating continuous-wave spectroscopy measurement showing the readout response as a function of the probe tone frequency. From left to right, the pronounced dips in the signal show the $gf/2$ and ge transitions of the SNAIL transmon. Those occur at $(\omega_{ge} - K)/2\pi$ and $\omega_{ge}/2\pi$ respectively. With $gf/2$, we refer to the two photon transition from ground state to second excited state. Fitting to the experimental data, we extract a Kerr value of $K/2\pi = (528 \pm 8)$ kHz.

FIGS. 7A-C show graphs illustrating **A** Time-resolved quantum coherent oscillation in $\hat{Y} = i|\alpha\rangle \langle -\alpha| - i| -\alpha\rangle\langle\alpha|$ as a function of relative phase ϕ between squeezing and linear drive. This measurement shows Rabi-like oscillation between the cat states created by superposing states in different wells. The oscillation frequency is a direct measure of the asymmetry. **B** Linear drive with relative phase of $\phi = 90°$. Symmetry between wells is preserved and no resonances are visible (compare to FIG. 3A). **C** Same experiment as depicted in FIG. 3A, but with a Rabi phase of 180° instead of 0°.

FIGS. 8A-B show graphs illustrating **A** Time-resolved quantum coherent Rabi-like oscillations as a function of squeezing amplitude. The squeezing amplitude is measured as the voltage of the digital controller. **B** Photon number $\langle\hat{a}^\dagger\hat{a}\rangle$ as function of applied voltage for the digital control of squeezing drive ϵ_2. The experimental data points are obtained from FIG. 8A using $\langle\hat{a}^\dagger\hat{a}\rangle = \epsilon_2/K = \Omega_{\mathrm{cat}}^2/16\epsilon_1^2$. A linear fit allows us to convert the voltage set by the digital control of ϵ_2 to the squeezing drive ϵ_2 in MHz. In the main text, we only present data measured with up to $\epsilon_2/K = 12$ (vertical dashed grey line).

FIGS. 9A-B show graphs illustrating activation and decay. **A** Pulse sequence for the determination of the activation time. **B** Decay of a coherent state initiated on the shallower well for different asymmetry values ϵ_1/K.

FIG. 10 shows images illustrating the reactions studied in an embodiment disclosed herein. Top left: the intramolecular proton transfer in the malonaldehyde. Top right: the cis-trans proton isomerization in malonaldehyde. Middle: the adenine-thymine double-proton transfer (amine, pyrimidine) between base pairs. Bottom: The guanine-cytosine double proton transfer (amine, pyrimidine) between base pairs.

FIGS. 11A-D show the Hamiltonian eigenstates obtained from matrix diagonalization for cis-cis malonaldehyde (A), cis-trans malonaldehyde (B), adenine-thymine (C) and guanine-cytosine (D) based on the chemical double-well Hamiltonian (blue) and the Kerr-Cat Hamiltonian (red) for c=0.1, superimposed on the potential energy surface along the reactive coordinate 'x'.

FIGS. 12A-D show the analysis of the Hamiltonian properties comparing the chemical double-well with the Kerr-Cat cQED device Hamiltonian for cis-cis malonaldehyde (A), cis-trans malonaldehyde (B), adenine-thymine (C) and guanine-cytosine (D). The chosen observables include the absolute difference of the eigenenergies (I), with the black dashed line indicating the chemical accuracy threshold based on electronic structure (1.5 mE$_h$) and the required magnitude of cQED device parameters (II) compared to current device capabilities (dashed horizontal lines). The vertical dashed lines indicate the value for c that gives reasonably accurate energy for the eigenstates required for kinetics (I) and the maximum experimental parameter values achievable with existing cQED Kerr-Cat platforms.

FIGS. 13A-D show the dependence of different observables on c at $\kappa = 0.1$, $n_{th} = 0.1$. (A) Cis-Cis Malonaldehyde. (B) Cis-Trans Malonaldehyde. (C) Adenine-Thymine. (D) Guanine-Cytosine. The time evolution of the product population for the four representative proton transfer reactions under consideration are shown in the top subpanels. Solid lines indicate the double-well dynamics and the diamonds the Kerr-Cat device dynamics (the same time grid was used for both but only a few points are plotted for clarity). The corresponding inverse reaction rate constants as a function of c, as obtained by fitting the to an exponential are shown in the bottom subpanels. The fit error is less than 2% for all systems and thus not visible in the plotted scale.

FIG. 14 shows a schematic view of a free energy double-well profile, $V(x)$, along the reaction coordinate, x, according to an embodiment of the disclosure. The reactant and product wells are designated by R and P , respectively. The transition state, which corresponds to the barrier top, is designated by TS. E_a and ΔG are the activation energy and reaction free energy, respectively. It should be noted that the reaction coordinate needs to be coupled to a thermal bath of nonreactive DOF (not shown) in order for rate kinetics to be emerge.

FIG. 15 shows graphs illustrating initial state selection for three different values of ϵ_1, ϵ_2 by applying a sigmoidal or Heaviside filtering function. The procedure is illustrated for the first 5 eigenstates, plotted with the metapotential on the background to showcase how the localization scheme performs. The right side showcases the effect of the different filter parameters as applied to the most suitable state that contains more than 50% density on the top well. Higher values of the sigmoidal tail value reduce initial state localization, while higher values introduce oscillatory motions due to the verticality of the filter function near its center.

FIGS. 16A-D show graphs illustrating convergence of Lindbladian eigenvalue timescale as a function of the number of Eigen-basis. (A) $n_{basis} = 5$. (B) $n_{basis} = 10$. (C) $n_{basis} = 20$. (D) $n_{basis} = 30$.

FIGS. 17A-B show graphs illustrating Relaxation timescales associated with the (A) Lindbladian maximal real eigenvalue and (B) the dynamical relaxation rates obtained by fitting the population traces as a function of the Kerr-Cat parameters ε_1 and ε_2. Both plots use dissipation parameters $\kappa = 0.1$, $n_{th} = 0.1$.

FIGS. 18A-C show graphs illustrating resonant and non-resonant regimes of the eigendensities between both sides of the double-well along the $p = 0$ metapotential cut. (A) Metapotential cut spanning $x \in [-10,10]$ Bohr. (B-C) Each state plotted as a function of position superimposed on the metapotential cut. The vertical axis denotes the absolute energy obtained by diagonalizing the Hamiltonian. (B) The asymmetric non-resonant regime (N1, N2) and a region where the double-well description is no longer valid (W). (C) The resonant regime falls along the white lines and reflect regimes with no asymmetry (S1, S2) as well as regions of increasing well asymmetry (A1-A2, A3-A4) by changing the minima-to-minima height.

FIGS. 19A-C show graphs illustrating dependence of timescale obtained by exact Lindbladian diagonalization on the dissipation parameter κ, for $n_{th} = 0.1$. (A) $\kappa = 0.05$. (B) $\kappa = 0.5$. (C) $\kappa = 5.0$.

FIGS. 20A-C show graphs illustrating dependence of timescale obtained by exact Lindbladian diagonalization on the dissipation parameter κ, for $\kappa = 0.001$. (A) $n_{th} = 0.05$. (B) $n_{th} = 0.5$. (C) $n_{th} = 1.0$.

FIGS. 21A-C show schematics illustrating incorporation of an oscillator into a circuit Quantum Electrodynamics (cQED) processor. (A) Capacitively shunted SNAIL with a series of stray inductance. (B-C) Modular assembly of capacitively shunted SNAILs for mapping 4 × 4 (B) and 8 × 8 (C; bottom) hermitian matrices.

FIG. 22 shows a Schematic representation of model systems for quantum dynamics simulations of energy transfer (top) and electron transfer (bottom).

FIG. 23 shows a scheme for simulating the SBM-SNAIL circuit that propagates energy transfer in the FMO 4-site model. The three parameters in the first circuit diagram are rotation angles that define the 1-qubit rotation operations. The four parameters in the bottom circuit diagram are the SNAIL gate parameters in eq 4.10. From left to right: oscillator frequency ω, third-order coupling term g_3, constant term H_{11}, and half of displacement R_{12}.

FIG. 24 shows graphs illustrating population dynamics for (top) spin-up state of the two-level system and (bottom) chlorophyll 1 of the 4-site FMO complex, obtained from single-boson-mapped Hamiltonians with simulated SNAIL circuit (eq 4.10, blue dots), benchmarked with results obtained from directly integrating the Schrödinger equation (red lines). Also shown (bottom panel) are the results obtained with the SBM mapping with qudit implementation (eqs 4.2−4.4, orange triangles).

FIG. 25 shows schematics illustrating transpiled circuit (top) and SNAIL circuit (down) for $\mathcal{U}_{\mathcal{P}^{\mathrm{pop}}}(t = 1\,\mathrm{a.u.})$.

FIG. 26 shows a graph illustrating Time dependent population of the electronic states, corresponding to the spin-boson model, obtained from the SBM-mapped $\mathcal{U}_{\mathcal{P}^{\mathrm{pop}}}(t)$ matrices with simulated SNAIL circuit implementation (red and blue dots), benchmarked with the dynamics obtained directly from the original $\mathcal{P}^{\mathrm{pop}}(t)$ matrices (red and blue lines).

DETAILED DESCRIPTION

Definitions

As used herein, each of the following terms has the meaning associated with it in this section. Unless defined otherwise, all technical and scientific terms used herein generally have the same meaning as commonly understood by one of ordinary skill in the art to which this disclosure belongs. Generally, the nomenclature used herein and the laboratory procedures in molecular biology, immunology, animal pharmacology, pharmaceutical science, peptide chemistry, and organic chemistry are those well-known and commonly employed in the art. It should be understood that the order of steps or order for performing certain actions is immaterial, so long as the present teachings remain operable. Any use of section headings is intended to aid reading of the document and is not to be interpreted as limiting; information that is relevant to a section heading may occur within or outside of that particular section. All publications, patents, and patent documents referred to in this document are incorporated by reference herein in their entirety, as though individually incorporated by reference.

In the application, where an element or component is said to be included in and/or selected from a list of recited elements or components, it should be understood that the element or component can be any one of the recited elements or components and can be selected from a group consisting of two or more of the recited elements or components.

In the methods described herein, the acts can be carried out in any order, except when a temporal or operational sequence is explicitly recited. Furthermore, specified acts can be carried out concurrently unless explicit claim language recites that they be carried out separately. For example, a claimed act of doing X and a claimed act of doing Y can be conducted simultaneously within a single operation, and the resulting process will fall within the literal scope of the claimed process.

As used herein, the singular form “a,” “an,” and “the” include plural references unless the context clearly dictates otherwise.

Unless specifically stated or obvious from context, as used herein, the term “about” is understood as within a range of normal tolerance in the art, for example within 2 standard deviations of the mean. “About” can be understood as within 10%, 9%, 8%, 7%, 6%, 5%, 4%, 3%, 2%, 1%, 0.5%, 0.1%, 0.05%, or 0.01% of the stated value. Unless otherwise clear from context, all numerical values provided herein are modified by the term about.

As used herein, the terms “comprises,” “comprising,” “containing,” “having,” and the like can have the meaning ascribed to them in U.S. patent law and can mean “includes,” “including,” and the like.

Unless specifically stated or obvious from context, the term “or,” as used herein, is understood to be inclusive.

Ranges provided herein are understood to be shorthand for all of the values within the range. For example, a range of 1 to 50 is understood to include any number, combination of numbers, or sub-range from the group consisting 1, 2, 3, 4, 5, 6, 7, 8, 9, 10, 11, 12, 13, 14, 15, 16, 17, 18, 19, 20, 21, 22, 23, 24, 25, 26, 27, 28, 29, 30, 31, 32, 33, 34, 35, 36, 37, 38, 39, 40, 41, 42, 43, 44, 45, 46, 47, 48, 49, or 50 (as well as fractions thereof unless the context clearly dictates otherwise).

As used herein, the term "ratio" refers to a relationship between two numbers (*e.g.*, scores, summations, and the like). Although, ratios can be expressed in a particular order (*e.g.*, *a* to *b* or *a*:*b*), one of ordinary skill in the art will recognize that the underlying relationship between the numbers can be expressed in any order without losing the significance of the underlying relationship, although observation and correlation of trends based on the ration may need to be reversed. For example, if the values of *a* over time are (4, 10) and the values of *b* over time are (2, 4), the ratio *a*:*b* will equal (2, 2.5), while the ratio *b*:*a* will be (0.5, 0.4). Although the values of *a* and *b* are the same in both ratios, the ratios *a*:*b* and *b*:*a* are inverse and increase and decrease, respectively, over the time period.

Detailed Description

Provided herein are devices for generating an asymmetric double well system. The device includes an oscillator; a parametric drive, and an additive drive. The parametric drive is arranged and disposed to bifurcate the oscillator, creating a double well, and the additive drive is arranged and disposed to create an asymmetry between the wells of the double well. FIG. 1A shows an example of the device 100 including a chip 110 on/in a support element 120. In some embodiments, the device 100 includes multiple chips 110. The support element 120 includes any suitable material and/or structure for supporting/housing the at least one chip 110. For example, as illustrated in FIG. 1A, the support element 120 includes a top portion 121 and a bottom portion 123. In some embodiments, the top portion 121 is aluminum and the bottom portion 123 is copper. Additionally or alternatively, in some embodiments, the top portion 121 includes at least one cavity 122 corresponding to the at least one chip 110 positioned on the bottom portion 123.

As illustrated in FIG. 1B, the oscillator 111 is formed on a surface of the chip 110. In some embodiments, the chip 110 includes multiple oscillators 111. For example, in some embodiments, the device 100 includes at least two chips 110, with at least one of the chips 110 having at least two oscillators 111. In some embodiments, the chip 110 also includes a filter 115 (*e.g.*, a Purcell filter) and/or a readout resonator 117. Referring again to FIG. 1A, in some embodiments, the support element 120 includes one or more drive lines 130 configured to couple the parametric drive 140 and the additive drive 150 to the at least one chip 110 and/or oscillator 111.

The oscillator 111 includes any suitable oscillator for generating an asymmetric double well when combined with the parametric 140 and additive 150 drives described herein. For example, in some embodiments, the oscillator 111 is a non-linear oscillator, such as, but not limited to, a transmon oscillator, a quantum Duffing oscillator, a trapped-ion oscillator, a neutral atom oscillator, or any other suitable oscillator. For example, in some embodiments, as illustrated in FIGS. 1C-D, the oscillator 111 includes two superconducting nonlinear asymmetric inductive elements (SNAILs) 112 shunted by a capacitor 114. In some such embodiments, the parametric drive 140 transforms the SNAIL-transmon Hamiltonian into a parametric oscillator Hamiltonian. Although discussed herein primarily with respect to two SNAILs, as will be appreciated by those skilled in the art, the disclosure is not so limited and includes any other suitable number of SNAILs (*e.g.*, 1, 3 or more, 4 or more, 5 or more, 6 or more, 7 or more, 8 or more, 9 or more, 10 or more, more than 10, or any suitable combination, sub-combination, range, or sub-range thereof).

The parametric drive 140 and the additive drive 150 include any suitable drive for generating the asymmetric double well described herein. For example, in some embodiments, the parametric drive 140 and/or the additive drive 150 includes a microwave drive. As will be appreciated by those skilled in the art, although discussed herein primarily with respect to microwave drives in connection with superconducting circuits, other drives (*e.g.*, laser) can be used with other oscillators/platforms (*e.g.*, trapped ion, neutral atom). In some embodiments, the parametric drive is twice or about twice the resonance frequency of the oscillator (*e.g.*, SNAIL). In some embodiments, the parametric drive creates the formation of the double well. Additionally or alternatively, in some embodiments, the additive drive is equal or about equal to the resonance frequency of the oscillator (*e.g.*, SNAIL). In some embodiments, the additive drive creates the asymmetry in the double well. In some embodiments, the drives include increased amplitude as compared to existing applications. For example, in some embodiments, the drive amplitude includes eps_1/K ~ 100 (i.e. absolute value of 0-100), eps_2/K ~ 40 (i.e. absolute value of 0-100), and/or delta/K ~ 20 (i.e. absolute value of 0-20). In some embodiments, the non-linear oscillator is parametrically and additively driven in the quantum regime.

In some embodiments, the asymmetric parametric oscillator can be described by the Hamiltonian:

$$\frac{H_{eff}}{\hbar} = -K\hat{a}^{\dagger 2}\hat{a}^2 + \epsilon_2(\hat{a}^2 + \hat{a}^{\dagger 2}) + |\epsilon_1|\left(e^{i\phi}\hat{a} + e^{-i\phi}\hat{a}^\dagger\right)$$

Where $\hat{a}$ is the bosonic annihilation operator, $K = -\frac{3g_4}{2} + \frac{10g_3^2}{3\omega_a}$ is the leading order Kerr non-linearity, g_3 and g_4 are the third- and fourth-order nonlinearities of the circuit, ϕ is the relative phase between the two drives, $\omega_d/2 = \omega_a$ with ω_a the renormalized transmon resonance frequency (which is Lamb-and the Stark-shifted from ω_0), and ω_0 is the bare resonance frequency of the oscillator. In such embodiments, the drive coefficients are given by $|\epsilon_1| = \frac{\Omega_1}{2}$ and $\epsilon_2 = g_3\frac{4\Omega_2}{3\omega_a}$, where Ω_1 is the amplitude of the additive drive and Ω_2 is the amplitude of the parametric drive. The relation to a double well becomes apparent in the classical limit by defining

$$\frac{V(x)}{\hbar} = \left.\frac{H_{eff}}{\hbar}\right|_{p=0} = k_4x^4 - k_2x^2 + k_1x$$

where $\hat{a} \mapsto \frac{1}{\sqrt{2}}(x + ip)$ is mapped together with $k_1 = \sqrt{2}|\epsilon_1|\cos\phi$, $k_2 = -\epsilon_2$, and $k_4 = -K/4$. In some embodiments, ϵ_1 controls the asymmetry of the wells and ϵ_2 controls their depth.

In some embodiments, the additive drive, the parametric drive, and the oscillator together form a continuously tunable asymmetric Kerr parametric oscillator. In some embodiments, the oscillator is a non-linear oscillator driven in the quantum regime. In some embodiments, the driven oscillator simulates a static system. In some embodiments, the oscillator is tunable by modifying how it is driven which, in contrast to existing devices which require weeks to tune, can be tuned in situ in milliseconds. Additionally, in contrast to existing digital quantum simulations requiring tens or hundreds of transmons, the device according to one or more of the embodiments disclosed herein can be formed with a single driven oscillator. Accordingly, in contrast to existing systems that require thousands or tens of thousands of transmons, a system can be scaled to simulate compound molecules in a hardware-efficient way with a few tens of coupled oscillators according to the embodiments disclosed herein.

In some embodiments, the device according to one or more of the embodiments disclosed herein is incorporated into a circuit Quantum Electrodynamic (cQED) processor. For example, in some embodiments, the cQED includes a modular assembly of oscillators. Referring to FIG.

21A, in some embodiments, the oscillator includes a capacitively shunted SNAIL with a series of stray inductance. As illustrated in FIGS. 21A, the cross-in-box symbol represents a Josephson tunnel junction, including an intrinsic shunt capacitance, while the circled arrow indicates a constant external flux Φ with tunable intensity. The phase operator $\hat{\varphi}$ associated with the active node of the circuit (white-filled circle) is related to ladder operators via $\hat{\varphi} = \varphi_{\mathrm{zpf}}(\hat{b} + \hat{b}^{\dagger})$. The oscillators can be modularly assembled for mapping of any suitable matrix, such as, but not limited to, a 4 × 4 hermitian matrix (FIG. 21B), a 8 × 8 hermitian matrix (FIG. 21C), or any other suitable matrix. In such embodiments, the dynamics of the i-th capacitively shunted SNAIL is described by a phase operator $\hat{\varphi}_i = \varphi_{\mathrm{zpf}_i}(\hat{b}_i + \hat{b}_i^{\dagger})$. The SNAILs are coupled via nearly quartic elements, represented as distorted cross-in-box symbols (in orange). Consequently, the eigenmodes can be assumed to be the same as those of the uncoupled system. In some embodiments, the molecular Hamiltonian of a model system can be mapped into the Hamiltonian of the modular cQED processor according to any of the embodiments disclosed herein. In some embodiments, the cQED processor could be run using a holographic approach, where the modes are measured and reset to represent other modes in the system.

In some embodiments, the device disclosed herein provides a highly unharmonic profile suitable for simulating the dynamics of a chemical reaction. For example, in some embodiments, one of the wells in the double well can be used for reactants while the other can be used for products. Additionally or alternatively, in some embodiments, the device is modular. In such embodiments, the device can have a single surface with two wells, or can be linked to form a surface with multiple split wells. In some embodiments, the device includes a low impedance oscillator to provide chemical accuracy in approximating the chemical potential by the bifurcated oscillator. In some embodiments, the oscillators' nonlinearity, parametric drive frequency, parametric drive amplitude, and linear drive amplitude are matched with the chemical Hamiltonian parameters. Additionally or alternatively, the Hamiltonian energy landscape and the dissipation parameters can all be tunable in situ over a large range of values containing many relevant molecules.

Also provided herein are methods of generating a double well system. In some embodiments, the method includes providing the device according to any of the embodiments disclosed herein; driving the oscillator with the parametric drive, the parametric drive bifurcating the oscillator and creating an effective double well; and driving the oscillator with an additive drive, the additive drive creating an asymmetry between the wells. In some embodiments, a barrier height of the asymmetric double well is continuously tuned and/or tunable by adjusting ϵ_2 according to the equation $\epsilon_2 = g_3 \frac{4\Omega_2}{3\omega_a}$, where g_3 is the third-order non-linearity of the circuit; Ω_2 is the amplitude of the parametric drive; ω_a is the renormalized oscillator resonance frequency, which is Lamb- and Stark-shifted from ω_0; and ω_0 is the bare resonance frequency of the oscillator. In some embodiments, the asymmetry of the asymmetric double well is continuously tuned and/or tunable by adjusting ϵ_1 according to the equation $|\epsilon_1| = \frac{\Omega_1}{2}$, where Ω_1 is the amplitude of the additive drive.

In some embodiments, an activation of the system exhibits pronounced quantum resonances whole width alternates with both the depth and the asymmetry of the wells. In some embodiments, the asymmetric double well experiences an increased activation time from one well to the other as compared to a symmetric double well. In some embodiments, the asymmetric double well experiences the increased activation time when the system is initialized in a shallower well. In some embodiments, the double well system formed by driving the oscillator according to the methods disclosed herein simulates a static system. In some embodiments, the method includes driving the non-linear oscillator in the quantum regime.

In some embodiments, the method includes modeling the dynamics of a chemical reaction with the asymmetric double-well. In some embodiments, the double-well comprises a Hamiltonian according to the equation:

$$\hat{H}_{DW} = \frac{\hat{p}^2}{2m} + k_4\hat{x}^4 - k_2\hat{x}^2 + k_1\hat{x}$$

where $\hat{x}$ is a position operator associated with motion along a reaction coordinate; $\hat{p}$ is a momentum operator associated with motion along the reaction coordinate; m is the mass associated with the motion along the reaction coordinate; and $\{k_1, k_2, k_4\}$ are positive and real parameters whose values define the double well free energy profile. In some embodiments, $\hat{x}$ and $\hat{p}$ satisfy the equation $[\hat{x}, \hat{p}] = i\hbar$. In some embodiments, the method further includes fitting the Hamiltonian to a fourth-order polynomial according to the equation:

$$V(x) = k_4x^4 - k_2x^2 + k_1x$$

where $k_4x^4 - k_2x^2$ relates to obtaining the double-well feature; and k_1x accounts for asymmetry between reactant and product wells.

In some embodiments, the method includes mapping a Hamiltonian of a Kerr-Cat device onto the double-well Hamiltonian, the Kerr-Cat device Hamiltonian having the equation:

$$\hat{H}_{KC} = \Delta\hat{a}^{\dagger}\hat{a} - K(\hat{a}^{\dagger})^2(\hat{a})^2 + \epsilon_2(\hat{a}^2 + \hat{a}^{\dagger 2}) + \epsilon_1(\hat{a} + \hat{a}^{\dagger})$$

where $\hat{a}^{\dagger}$ and $\hat{a}$ are the device's ladder operators, associated with excitations and de-excitations, respectively, between the device's effective energy levels; K is the Kerr non-linearity; Δ is the detuning; and ϵ_1 and ϵ_2 are drive coefficients. In some embodiments, $\hat{a}^{\dagger}$ and $\hat{a}$ satisfy the equation $[\hat{a}, \hat{a}^{\dagger}] = 1$. In some embodiments, mapping of the Kerr-Cat device Hamiltonian onto the double-well Hamiltonian includes mapping photonic operators $\{\hat{a}, \hat{a}^{\dagger}\}$ onto operators associated with motion along a reaction coordinate $\{\hat{x}, \hat{p}\}$ according to the equations:

$$\hat{a} = \frac{1}{\sqrt{2}}\left(\frac{1}{c}\hat{x} + \frac{ic}{\hbar}\hat{p}\right) \; ; \; \hat{a}^{\dagger} = \frac{1}{\sqrt{2}}\left(\frac{1}{c}\hat{x} - \frac{ic}{\hbar}\hat{p}\right)$$

$$\hat{x} = \frac{c}{\sqrt{2}}(\hat{a} + \hat{a}^{\dagger}) \; ; \; \hat{p} = \frac{\hbar}{i\sqrt{2}c}(\hat{a} - \hat{a}^{\dagger});$$

where c is a constant parameter that has units of length.

In some embodiments, the method includes recasting a negative of the Kerr-Cat Hamiltonian in terms of the $\hat{x}$ and $\hat{p}$ according to the following equation:

$$-\hat{H}_{KC} = \frac{c^2}{\hbar^2}(\epsilon_2 - K - \Delta/2)\hat{p}^2 + \frac{K}{4c^4}\hat{x}^4 - \frac{1}{c^2}(\epsilon_2 + K + \Delta/2)\hat{x}^2 - \frac{\epsilon_1\sqrt{2}}{c}\hat{x} + \frac{Kc^4}{4\hbar^4}\hat{p}^4 + \frac{K}{4\hbar^2}\hat{x}^2\hat{p}^2 + \frac{K}{4\hbar^2}\hat{p}^2\hat{x}^2$$

where $\hat{a}^{\dagger}$ and $\hat{a}$ are the device's ladder operators, associated with excitations and de-excitations, respectively, between the device's effective energy levels; K is the Kerr non-linearity; Δ is the detuning; and ϵ_1 and ϵ_2 are drive coefficients. In some embodiments, $\hat{a}^{\dagger}$ and $\hat{a}$ satisfy the equation $[\hat{a}, \hat{a}^{\dagger}] = 1$.

In some embodiments, the method includes mapping $\{\Delta, K, \epsilon_1, \epsilon_2\}$ onto $\{m, k_1, k_2, k_4\}$ using the following mapping relations:

$$K = 4c^4k_4;$$

$$\epsilon_2 = \frac{\hbar^2 + 2c^4k_2m}{4c^2m};$$

$$\Delta = \frac{2c^4k_2m - \hbar^2 - 16c^6k_4m}{2c^2m}; \text{ and}$$

$$\epsilon_1 = \frac{ck_1}{\sqrt{2}}.$$

In some embodiments, the method includes selecting c to satisfy the following inequality:

$$\frac{\hbar^2}{mk_2c^4} \gg 1.$$

In some embodiments, modeling the dynamics of a chemical reaction with the asymmetric double-well includes modeling chemical reactivity between reactants and products within the double-well energy surface. The particularities of the energy surface determine the system's dynamics. Quantum effects are relevant at the molecular level, and can be simulated using a quantum system. Among quotidian chemical reactions, these quantum effects have system-specific relevance and are controlled by dissipation. In some embodiments, the modeling is accomplished through modifying, in hardware and/or microwave operation regime, a quantum oscillator driven into bifurcation by a parametric modulation to mimic a chemically relevant double well and study reaction dynamics. In some embodiments, a direct analog simulation of the landscape of chemically relevant reactions is implemented via a single-driven transmon. The chemically relevant reactions include any suitable reactions, such as, but not limited to, proton transfer reactions between the DNA base pairs Guanine-Cytosine, Malonaldehyde (cis-cis proton tautomerization), Malonaldehyde (cis-trans proton tautomerization), and Adenine-Thymine (DNA).

Those skilled in the art will recognize, or be able to ascertain using no more than routine experimentation, numerous equivalents to the specific procedures, embodiments, claims, and examples described herein. Such equivalents are considered to be within the scope of this invention and covered by the claims appended hereto.

It is to be understood that wherever values and ranges are provided herein, all values and ranges encompassed by these values and ranges, are meant to be encompassed within the scope of the present invention. Moreover, all values that fall within these ranges, as well as the upper or lower limits of a range of values, are also contemplated by the present application.

The following examples further illustrate aspects of the present invention. However, they are in no way a limitation of the teachings or disclosure of the present invention as set forth herein.

EXAMPLES

EXAMPLE 1 - Increased lifetime in Kerr parametric oscillator for fine-tuned asymmetries

I. Introduction

The Kerr parametric oscillator, a nonlinear oscillator made bi-stable by a parametric drive, is an elementary quantum optical model that has continuously received attention for decades because, despite its simplicity, it is surprisingly rich. In the early 1990s it was predicted that this system should exhibit quantum tunnelling between the two stable points, opening a pathway to engineer a highly controllable simulator for the physics involved in quantum chemistry, nuclear structure, two-level systems and other problems involving a double well energy surface. The physical implementation of such a promising model was, however, challenging and experiments in the quantum regime have been realized only recently. The refinement of experiments, enabled by control of experimental parameters over a large range, not only verified a battery of longstanding theoretical predictions but also revealed new physics, like the modulation of the activation rate by the quantization of quasienergies and their resonances, which has direct implications for quantum chemistry and quantum computation.

This Example describes the exploration of the activation dynamics in the case of a continuously tunable asymmetric double well parametric oscillator. Two unexpected effects were found during this exploration. First, it was found that the asymmetric double well can experience a significantly longer activation time from one well to the other (well-switching) than the symmetric case, even when the system is initialized in the shallower well. This is counterintuitive because one would think that by reducing the barrier height, the activation time should decrease. This is not the case in the present system due to a fine-tuned quantum effect that can heuristically be explained: increasing asymmetry breaks resonances inside the double well, hindering tunneling. Yet, excessive asymmetry revives the resonances by aligning energy levels again. Thus, a sweet spot exists between these extremes, maximizing the activation time. This is in contrast to the resonant quantum tunnelling observed in the symmetric case. The second unexpected effect is only observable thanks to the simultaneous and continuous tunability of barrier height and asymmetry described herein: the activation of the system exhibits pronounced quantum resonances whose width alternates with both the depth and the asymmetry of the wells. The incoherent activation rate of the system reflects the width of the Hamiltonian anti-crossing of the energy levels close to the separatrix of the double well energy surface. The location and width of these resonances clearly reveal Hamiltonian properties and are remarkably well explained by a time-independent quantum model obtained from the parametrically driven system under a rotating wave approximation (RWA). Semiclassical predictions are also in excellent agreement with the data and provide a deeper insight. A basic Lindbladian model fails, however, to capture quantitatively the purely dissipative activation rates and it is argued, via control experiments presented in the Supplementary material (SM), that this is related to the breakdown of the RWA in the experimental conditions.

II. Setup and Model System

The present setup consists of two chips with superconducting circuits, shown in FIG. 1A, that are addressable by microwave drives via charge-coupling. In this experiment, use is made of only one of the two chips. The relevant chip contains an array of two superconducting nonlinear asymmetric inductive elements (SNAILs) shunted by a large capacitor, as depicted in FIGS. 1B-D.

The Hamiltonian of a SNAIL transmon with charge drives can be approximated as:

$$\frac{H(t)}{\hbar} = \omega_0 \hat{a}^\dagger \hat{a} + \frac{g_3}{3}(\hat{a} + \hat{a}^\dagger)^3 + \frac{g_4}{4}(\hat{a} + \hat{a}^\dagger)^4 - i\Omega_1 \sin(\omega_1 t + \phi)\,(\hat{a} - \hat{a}^\dagger) - i\Omega_2 \sin(\omega_2 t)\,(\hat{a} - \hat{a}^\dagger), \tag{1.1}$$

where ω_0 is the bare resonance frequency of the SNAIL transmon, g_3, g_4 are the third- and fourth-order nonlinearities of the circuit and $\hat{a}$ is the bosonic annihilation operator. Here, Ω_1 is the amplitude and ω_1 the frequency of the drive that will henceforth be referred to as the linear (additive) drive, while Ω_2 and ω_2 are the amplitude and frequency of what is referred to herein as the squeezing, or two-photon, parametric drive. This Hamiltonian is the so-called (asymmetric) parametric oscillator Hamiltonian when $\omega_2 \approx 2\omega_0$ and $\omega_1 \approx \omega_0$. The phase ϕ is the relative phase between the two drives. By applying displaced frame transformations, transforming into the rotating frame $\omega_2/2$ and keeping some terms beyond the RWA, the effective Hamiltonian describing the asymmetric parametric oscillator

$$\frac{H_{eff}}{\hbar} = -K\hat{a}^{\dagger 2}\hat{a}^2 + \epsilon_2(\hat{a}^2 + \hat{a}^{\dagger 2}) + |\epsilon_1|\left(e^{i\phi}\hat{a} + e^{-i\phi}\hat{a}^\dagger\right) \tag{1.2}$$

where $K = -\frac{3g_4}{2} + \frac{10g_3^2}{3\omega_a}$ is the leading order Kerr non-linearity, and $\omega_d/2 = \omega_a$ with ω_a the renormalized SNAIL transmon resonance frequency (which is Lamb-and the Stark-shifted from ω_0). The drive coefficients are given by $|\epsilon_1| = \frac{\Omega_1}{2}$ and $\epsilon_2 = g_3\frac{4\Omega_2}{3\omega_a}$. The relation to a double well becomes apparent in the classical limit by defining

$$\frac{V(x)}{\hbar} = \left.\frac{H_{eff}}{\hbar}\right|_{p=0} = k_4 x^4 - k_2 x^2 + k_1 x, \tag{1.3}$$

where we have mapped $\hat{a} \mapsto \frac{1}{\sqrt{2}}(x + ip)$ together with $k_1 = \sqrt{2}|\epsilon_1| \cos \phi$, $k_2 = -\epsilon_2$ and $k_4 = -K/4$. Two instances of $V(x)$ are shown in FIGS. 2A and C, while in FIGS. 2B and D the associated energy spectra are shown as a function of the control parameters ϵ_1 and ϵ_2 for $\phi = 0$. Rather transparently from Eq. (1.2) or Eq. (1.3), ϵ_1 controls the asymmetry of the wells and that ϵ_2 controls their depth. Note, however, that the parametric oscillator Hamiltonian cannot be written as a sum of kinetic $[T(p)]$ and potential $[V(x)]$ energy since cross terms like x^2p^2 are present. These terms can lead to interesting effects but they do not play a critical role in the current exposition.

For $\epsilon_1 = 0$, this is the conventional (symmetric) parametric oscillator Hamiltonian that creates a double well along the position axis. If $\epsilon_1 \neq 0$, then the phase ϕ becomes relevant. For $\phi = 90°$, the linear drive is momentum-like, thus not breaking the symmetry of the double well. For $\phi = 0$, this drive is position-like and lifts the degeneracy between the two wells (see FIGS. 2C-D). The main text focuses on the case $\phi = 0$ and leaves the experimental study of the phase dependence for the SM.

Lastly, to model the activation rate, an ordinary Lindbladian model is used, containing only single photon gain and single photon loss with phenomenological rates and temperature (see Section IV).

III. Experiment and Analysis

To measure the activation rate in this system, the states localized at the bottom of the wells need to be prepared and measured as a function of time. A number of steps are required for this. To ready the setup for the present experiments, the SNAIL loops are biased with an external magnetic field sourced by a solenoid lying below the copper part of the enclosure (orange block in FIG. 1A). This flux allows setting of the Hamiltonian parameters ω_a and K. In this work, a flux point was chosen at which $\omega_a/2\pi = 6.086$ GHz and $K/2\pi = (528 \pm 8)$ kHz are directly measured (see SM). From the flux dependence of both ω_a and K, a model can be fit for the SNAIL to extract $g_3/3 = 2\pi$ and $g_4/4 = 2\pi$. The values of Ω_1 and Ω_2 are directly proportional to the microwave amplitude applied to the sample and, therefore, precise control is provided over ϵ_1 and ϵ_2 (see SM). In the present system, dielectric loss sets the single-photon lifetime to 20 μs.

To prepare the oscillator in its steady state, the squeezing drive is turned on and allowed to run for 5 times the single photon lifetime (*e.g.*, waiting for 5 times the single photon lifetime after turning on the squeezing drive will allow the oscillator to reach steady state). The bifurcation of the SNAIL oscillator is observed by homodyning the emitted radiation (i.e. fluorescent readout). The fluorescence is microwave-activated by a tone parametrically coupling the parametric oscillator with the on-chip readout resonator coupled to the quantum-limited amplifier detection line. The homodyne signal clearly shows the typical pair of stable oscillations out-of-phase by 180°. Importantly, the photons emitted by the oscillator during readout are continuously replenished by the squeezing drive: the driven oscillator in presence of dissipation remains in one of its two (quasi-)steady states. Taking a single data point for the discrimination between parametric oscillator states, takes 4 μs. This is typically much shorter than the activation time across the double well parametric oscillator barrier. By performing a second measurement after a variable waiting time (see SM), one can detect activation events changing the state of the parametric oscillator from one stable state to the other. By repeating these measurements, one can determine the probability per unit time of having an activation event and therefore directly measure the activation rate for a given set of Hamiltonian parameters ϵ_1/K and ϵ_2/K.

To measure the activation rate in the parametric oscillator, the instances when the system is found initially in the shallower well are measured and post-selected. In FIG. 3A measurements of the population dynamics in between the two steady states are shown for different values of the asymmetry, controlled by ϵ_1/K. For these measurements the squeezing amplitude is set to $\epsilon_2/K = 7.7$. The probability as a function of time of remaining in the initial state is well approximated by an exponential decay (see SM). This timescale of these exponential T is a direct measurement of the activation rate ($1/T$). FIG. 3B shows a theory prediction computed from a Lindbladian model including single-photon loss at rate $\kappa/K = 0.025$ and gain corresponding to a finite temperature determined by a mean number of thermal photons $n_{th} = 0.05$. Resonances are observed for certain values of ϵ_1/K, where the activation rate is markedly increased. These are resonances between states in different wells. The resonance for levels deep within the wells behave effectively as level crossings since the coupling is exponentially small due to the suppressing of tunneling under the barrier. Therefore, these activation events are mediated by thermal and quantum heating from the ground state into the tunneling levels at the barrier top. This is observed from the data by noting that the alternating width of the different resonance in FIG. 2D correspond to the strength of the anti-crossings of the spectrum at the barrier top (purple levels in FIG. 2C). This interpretation of the data allows for prediction of the location in parameter space where resonant tunneling takes place. This happens when the uncoupled levels in the right and left well align. By realizing that the energy spacing of the states in the wells can be estimated by $S \approx 4\epsilon_2$ and that the asymmetry can be estimated from Eq. (1.3) as $A \approx 4\epsilon_1\sqrt{\epsilon_2/K}$, the resonance condition is written as $(A = nS)$

$$\frac{\epsilon_2}{K} \approx \left(\frac{\epsilon_1}{nK}\right)^2, \tag{1.4}$$

This simple formula predicts the location of the resonances with remarkable precision (see FIGS. 4A-C).

The dashed parabolas in FIGS. 4A-C are obtained from Eq. (1.4). This theoretical analysis is complemented with a semiclassical action quantization prescription dictating the number of allowed quantum orbits per well. The number of allowed quantum orbits is given by the number of action quanta enclosed by the asymmetric “figure eight” lemniscate delineating the phase space separatrix in between the wells. The orange and blue curves in FIG. 4A show the pairs ϵ_1/K and ϵ_2/K where the Einstein–Brillouin–Keller orbit quantization condition

$$\frac{1}{2\pi}\oint p dx \approx \frac{3}{2}\tilde{n}\hbar, \tag{1.5}$$

is satisfied. Here, $\tilde{n} = n, m$ is an odd number. The triple intersection points of the parabolas from Eq. (1.4) with the action quantization conditions mark the point in parameter space where a new level enters the wells in the tunneling resonances condition. They are marked with red circles labeled by (*n,m*), the quantum number of each well. At these points, where each well contains exactly $(n + 1)/2$ and $(m + 1)/2$ semiclassical orbits, the resonance is expected to broaden due to a new orbit contributing to the activation rate.

FIG. 4B shows the measured activation time for a fine scan of both ϵ_1/K and ϵ_2/K. The resonances are clearly shown to have width that changes as the broad anti-crossings are narrowed by the suppression of tunnel splitting up to the point that the tunneling through a given excited pair of states is relayed by the tunneling via the next pair of excited states, now at the top of the barrier and the new limiting processes setting the activation time. See this by following the purple energies and their tunnel splitting in FIG. 2D. The agreement of the Hamiltonian theory with the experiment is remarkable (see SM for a full quantum treatment). The Hamiltonian theory predicts, quantitatively, the resonance condition and, qualitatively, their widths.

FIG. 4C shows the Lindbladian prediction of the experiment. The agreement is excellent in regards to the location and behavior of the resonance in parameter space but falls short in quantitatively predicting the activation rates measured. However, many features of the data are correctly captured, like for example, the fact that an asymmetric system can have a longer activation lifetime than the symmetric system, even if one of the wells is markedly shallower. See this directly from FIGS. 3A-B at $\epsilon_1/K \approx 1$. The green-black dashed line in FIG. 4B shows the experimentally determined maxima of T as a function of the control parameters. The theoretical maxima are shown in FIG. 4D by the line of the same colors. The location of the maxima is nontrivial, and it is relevant because it can readily be used to extend the lifetime of a Kerr-cat qubit. The effect was unknown to us before the analysis of our experimental data.

FIGS. 5A-B show that the increase of T as a function of the asymmetry can be large. To provide physical insight into this effect it is noted that for the symmetric case ($\epsilon_1 = 0$), T is modulated in a step-like fashion by the orbits falling under the barrier. The linear drive can be exploited to break the (parity) symmetry of these orbits as shown in FIGS. 2A-D and therefore avoid altogether the resonant saturation seen for $\epsilon_1 = 0$ in FIGS. 5A-B. This observation explains the trajectory of the green-black curve in FIGS. 4B-C which snakes around “avoiding” the resonance conditions omened by the red circles. In other words, quantum tunneling produces a hybridization of the classically decoupled orbits under the barrier, so the asymmetry degree of freedom can be used to minimize that hybridization, reducing the tunneling rate via the excited states, and avoid the plateaus in FIGS. 5A-B almost completely.

IV. Conclusion

The measurement of the activation rate in a continuously tunable asymmetric Kerr parametric oscillator is reported and a fine structure that was previously unknown is observed. The quantized energy level structure is manifest in the activation dependence on the control parameters. The features in the activation times caused by this parameter dependence are captured by a simple model and a semiclassical analysis, which allowed for extension of the knowledge gained in this study beyond parametric oscillators.

The importance of this system is noted for quantum computation as qubits encoded in the well state. In this regard, two contributions of the present work deserve to be highlighted. The first one is a way to increase the activation timescale T in between the wells by a fine control of the asymmetry. This directly maps to a reduction of bit-flip errors with no extra hardware requirements. The second one is that the operation of a highly asymmetric parametric oscillator was demonstrated in the quantum regime. Direct evidence is provided that the static effective description is not compromised under strong linear drives, which are required for fast gates and new implementations of hardware efficient readout schemes.

To conclude, it is remarked that despite the rich literature and prior efforts by the present inventors, there is still a need for a comprehensive theoretical understanding of the measured activation rates in the experiments. This, in turn, forms part of a larger program attempting to engineer high-fidelity quantum computing gates and measurements and in particular, common to all other parametric oscillator experiments operating in the quantum regime reported in the literature.

V. Supplementary Material

A. Calibrations of Experimental Parameters

1. Measurement of Kerr coefficient

The Kerr coefficient *K*, as used in the parametric oscillator Hamiltonian Eq. (1.2), is extracted by spectroscopy. A saturating probe drive ω_{pr} is applied to the SNAIL transmon operated with $\epsilon_2 = 0$. Varying the probe drive frequency and measuring the response via dispersive readout, results in the data shown in FIG.6. The spectrum shows two clear dips, which correspond, from lower frequency to higher frequency, to the two-photon $gf/2$ transition and the ge transition (the SNAIL levels are labeled following the atomic physics convention in increasing energy order *g, e, f,* ...). We then extract Kerr by using the relation $\omega_{ge} - \omega_{gf/2} = K$. Fitting two Gaussian peaks to the spectrum in FIG. 6, we find $K/2\pi = (528 \pm 8)$ kHz.

2. Calibration of relative phase between squeezing drive and linear drive

Quantum coherent Rabi-like oscillations as a function of this phase ϕ are shown in FIG. 7A. For $\phi = 0$, this drive is position-like and lifts the degeneracy between the two wells (see FIG. 2C). This energy difference induces the Rabi-like oscillation. For $\phi = 90°$ (FIG. 7B), the linear drive is momentum-like (the Hamiltonian term is $\propto \hat{p}$), thus not breaking the symmetry of the double well. Turning to FIG. 7C, a $\phi = 180°$ flipped the phase as compared to $\phi = 0°$ (FIG. 3A), resulting in an exchange of the left and right well, meaning that now the left well is the deeper well. In the experiment, we still initialize in the shallower (now right) well, but now measure the time-resolved population of the deeper (now left) well. As a result, the population of the left well is initially zero and then increases over time. We again observe trends and features, such as the resonant-tunneling also seen in FIG. 3A. This confirms that the 180° phase shift only exchanges the roles of the wells, but otherwise exhibits the same physical phenomena.

3. *Calibration of squeezing (parametric) drive amplitude* ϵ_2 *and linear drive amplitude* ϵ_1

In the experimental setup, the drive amplitudes are directly controlled by a digital to analog voltage converter. To calibrate the strength of the drive in MHz we measure time-resolved Rabi oscillations as a function of the digital control of the squeezing drive ϵ_2. The experimental data is shown in FIG. 8A. The oscillations of the observable $\hat{X} = (|\alpha\rangle\langle\alpha| - |-\alpha\rangle\langle-\alpha|)/|\alpha|^2$ occur at a rate $\Omega_{\text{cat}}(\epsilon_2) \approx \Re(4\epsilon_1\alpha^*)$ where $\alpha = \sqrt{\epsilon_2/K}$ and the approximation is valid for $|\alpha| > 1$ $\alpha > 1$. Using, also, that for $\epsilon_2 = 0$ the oscillation has a frequency of $2\epsilon_1$, just like for an ordinary transmon, we obtain ϵ_1 in MHz completing the calibration of the drive amplitudes. To be clear, we can rewrite this relation as $\langle\hat{a}^\dagger\hat{a}\rangle = \epsilon_2/K = \Omega_{\text{cat}}(\epsilon_2)^2/16\epsilon_1^2$, where $\langle\hat{a}^\dagger\hat{a}\rangle$ is the average photon number of the coherent states. By extracting the Rabi rate Ω_{cat} for each voltage of the digital control of ϵ_2 and using the previously determined value of ϵ_1, we find $\langle\hat{a}^\dagger\hat{a}\rangle$ as a function of the digital control of ϵ_2. The data is shown in FIG. 8B and shows a clear linear relationship between the applied voltage for the drive and the average photon number. The slope of the linear fit (together with the previously extracted value of Kerr) determines the proportionality constant between the digital to analog converter in volts and the drive amplitude ϵ_2 in MHz as required by the Hamiltonian description.

FIG. 9A illustrates a pulse sequence for the determination of the activation time. The squeezing drive is turned on adiabatically. This is followed by a measurement of the which-well information, projecting the parametric oscillator into either of the wells. Then the linear drive is turned on adiabatically. Next, the state evolves for a variable time *t*, during which both the squeezing and linear dive remain on. After that, the linear drive is turned off adiabatically. Finally, the which-well information is measured again to find the remaining population. FIG. 9B shows decay of a coherent state initiated on the shallower well for different asymmetry values ϵ_1/K. Experimental data are dots, solid lines are exponential fits. For small well asymmetry ϵ_1/K, the probability to be in the shallower well decays to 0.5. For increasingly large asymmetry, the steady-state population is no longer equally distributed between both wells, becoming increasingly biased towards the deeper well.

EXAMPLE 2 – Quantum Dynamic Simulations On A Parametrically Driven Bosonic Quantum Device

Abstract

The dynamics of elementary chemical reactions correspond to crossing a free energy barrier to go from the reactant well to the product well along a reaction coordinate. The traditional approach to testing and validating chemical rate theories, aimed at describing the barrier crossing dynamics, calls for the labor-intensive performance of a large number of measurements on multiple chemical systems under different conditions, in an attempt to cover the relevant parameter space. In this paper, we propose an alternative approach to testing chemical rate theories, which is based on emulating the barrier crossing dynamics on a Kerr-Cat device. Within this approach, one has control over the parameters that define the double-well free energy profile, as well as external parameters such as the temperature and strength of coupling between the reaction coordinate and the thermal bath of non-reactive degrees of freedom. Simulating chemical dynamics on this platform thereby opens the door to exploring chemical dynamics in different regimes that range from the conventional classical transition-state-theory(TST)/Arrhenius rate theory to inherently quantum post-TST/non-Arrhenius rate theories. We showcase the utility of the new approach by showing how the chemical dynamics underlying four prototypical proton transfer reactions can be simulated on a Kerr-Cat device.

Introduction

The molecular dynamics underlying elementary chemical reactions are typically described as a process that takes the system from the reactant well to the product well along a reaction coordinate. The free energy profile along the reaction coordinate typically has a double-well shape, with the reactant and product wells, which correspond to local minima on the free energy surface and thereby stable molecular configurations, separated by a free energy barrier, such that the transition from reactant to product typically requires crossing the barrier. The metastable molecular configuration at the barrier top is known as the *transition state*. The barrier crossing dynamics is often described in terms of a reactant-to-product *reaction rate constant*, *k*. Within the framework of *transition-state theory (TST)*, the dependence of *k* on the barrier height (often referred to as the *activation energy*), E_a, is given by the Arrhenius law, $k = Ae^{-E_a/k_BT}$, where k_B is the Boltzmann constant, *T* is the absolute temperature, and *A* is the so-called pre-exponential factor (which corresponds to the rate constant in the activation-less case, $E_a = 0$).

Deviations from TST and Arrhenius law can occur when the assumptions underlying those rate theories are not valid. More specifically, a significant number of classical recrossing events can lead to deviations from TST, while quantum tunneling and zero-point energy effects can give rise to reactive pathways that do not rely on classical barrier crossing. Furthermore, the description of chemical dynamics in terms of a rate constant can become invalid in cases where the barrier height becomes comparable to or smaller than $k_B T$, or when the coupling between the reaction coordinate and the other non-reactive molecular degrees of freedom (DOF), which serve as a thermal bath, is weak. Thus, deviations from TST and Arrhenius law can often be traced back to the inherently quantum-mechanical nature of chemical dynamics.

An example of an elementary chemical reaction of fundamental biological importance that can be modeled in terms of the aforementioned double-well free energy profile is the adenine-thymine proton transfer reaction in DNA. The free energy profile in this case varies depending on physiological conditions. During the cell life, the free energy profile favors the hydrogen-bonded form. However, the hydrogen bond needs to be broken during cell replication in order for the DNA strands to be duplicated. Thus, simulating the chemical dynamics of the Adenine-thymine proton transfer reaction across a wide range of double-well free energy profiles is called for.

The traditional approach to testing and validating chemical rate theories (both TST/Arrhenius and post-TST/non-Arrhenius) is based on performing a large number of experimental measurements of chemical dynamics on a wide range of molecular systems under a similarly wide range of external conditions, which presumably cover both chemical space and the space of parameters that are known to affect chemical dynamics within a given molecular system, such as temperature and the type and strength of coupling between the reaction coordinate and the bath of non-reactive DOF. As a result, pursuing such an approach is often found to be highly challenging as well as labor-intensive, due to one's limited ability to experimentally monitor the reactant and product populations in real time and since changing from one chemical system to another implies changing multiple parameters, often in an uncontrollable manner. A prime example of the challenging nature of the traditional approach is the 30 year gap between the theoretical prediction of the inverted region in the Marcus rate theory for electron transfer reactions and its experimental validation.

A highly promising alternative approach to experimentally testing and validating chemical rate theories has recently become possible by the availability of controllable and highly tunable fully quantum-mechanical platforms that make it possible to explore quantum dynamics of various nontrivial model systems across extremely wide ranges of parameter space. Given that chemical dynamics is inherently quantum-mechanical in nature and the fact the most under-explored regimes of chemical dynamics exhibit pronounced quantum effects, such platforms provide a golden opportunity for advancing and enhancing chemical rate theory.

A recent example of this approach was recently reported, where using an ion-trap platform to perform analog simulations of the chemical dynamics underlying electron transfer (redox) reactions across an extremely wide range of parameter space was proposed. It should be noted that *Marcus theory* for the reaction rate constant of electron transfer reactions is analogous to TST for non-redox chemical reactions, since it is based on invoking a TST-like argument and gives rise to an Arrhenius-law type expression for the rate constant. More specifically, in the case of Marcus theory, the transition-state is identified with the molecular configuration at the crossing point between the donor state (reactant) and acceptor state (product) diabatic free energy profiles along the reaction coordinate (which corresponds to the collective nuclear motion associated with the reorganization of the nuclear DOF upon electron transfer). Similarly to TST, Marcus theory is based on treating the activation to the crossing point (transition state) as a classical process, and also assumes that the electronic coupling between the diabatic donor and acceptor states is weak. Schlawin et al. showed how the predictions of Marcus theory can be reproduced on their proposed ion-trap device, including in the inverted regime. They also showed how the proposed ion-trap device can be used to explore deviations from Marcus theory due to quantum (low temperature) and strong electronic coupling effects. As a result, the study of unconventional electron transfer regimes that are hard to study via the traditional approach became possible.

In this Example, a new general strategy for simulating the chemical dynamics of non-redox elementary chemical reactions on a fully quantum platform based on a circuit cavity quantum electrodynamics (cQED) Kerr-Cat device is proposed. We start out by introducing the Kerr-Cat device and highlighting features that make it suitable for analog simulation of chemical dynamics. We proceed by considering several prototypical examples of chemical dynamics that would be used to demonstrate the ability of the Kerr-Cat device to simulate chemical dynamics.

We then present a general-purpose protocol for simulating chemical dynamics on the Kerr-Cat device and demonstrate its utility on the aforementioned prototypical chemical examples.

Device Dynamics and Dissipator

We start out by considering a cQED Kerr-Cat device described by the following effective Hamiltonian:

$$\hat{H}_{KC} = \Delta\hat{a}^{\dagger}\hat{a} - K(\hat{a}^{\dagger})^{2}(\hat{a})^{2} + \epsilon_{2}(\hat{a}^{2} + \hat{a}^{\dagger 2}) + \epsilon_{1}(\hat{a} + \hat{a}^{\dagger}) \tag{2.1}$$

Here, $\hat{a}^{\dagger}$ and $\hat{a}$ are the device's ladder operators, associated with excitations and de-excitations, respectively, between the device's effective energy levels, which satisfy the commutator $[\hat{a}, \hat{a}^{\dagger}] = 1$. Importantly, the Kerr-Cat Hamiltonian in Eq. (2.1) is tunable via the four parameters that it depends on, namely, the Kerr non-linearity, K, the detuning, Δ, and the drive coefficients, ϵ_1 and ϵ_2, with the latter determining the squeezing amplitude. We assume that the dynamics of the device is described by a Lindblad equation of the following form:

$$\frac{\partial\hat{\rho}}{\partial t} = \frac{i}{\hbar}\left[\hat{H}_{KC}, \hat{\rho}\right] + \kappa(1 + n_{th})\left(\hat{a}\hat{\rho}\hat{a}^{\dagger} - \frac{1}{2}\{\hat{a}^{\dagger}\hat{a}, \hat{\rho}\}\right) + \kappa n_{th}\left(\hat{a}^{\dagger}\hat{\rho}\hat{a} - \frac{1}{2}\{\hat{a}\hat{a}^{\dagger}, \hat{\rho}\}\right) \tag{2.2}$$

Here, $\hat{H}_{KC}$ is as in Eq. (2.1), κ sets the photon-loss rate, and n_{th} sets the device temperature. It should be noted that similarly to $\{K, \Delta, \epsilon_1, \epsilon_2\}$, κ and n_{th} are also experimentally tunable parameters.

Chemical Mapping

Next, consider the following double-well Hamiltonian, which is suitable for modeling the dynamics of a wide range of elementary chemical reactions:

$$\hat{H}_{DW} = \frac{\hat{p}^{2}}{2m} + k_{4}\hat{x}^{4} - k_{2}\hat{x}^{2} + k_{1}\hat{x} \tag{2.3}$$

Here, $\hat{x}$ and $\hat{p}$ are the position and momentum operators associated with motion along the reaction coordinate, which satisfy $[\hat{x}, \hat{p}] = i\hbar$; m is the mass associated with the motion along the reaction coordinate; and $\{k_1, k_2, k_4\}$ are positive and real parameters whose values define the double well free energy profile, and thereby the specific chemical system, that the Hamiltonian describes. More specifically, given the double-well free energy profile for a specific chemical system, which can be obtained from electronic structure and MD simulations, we assume that it can befitted to a minimal fourth-order polynomial of the form $V(x) = k_4x^4 - k_2x^2 + k_1x$. The $k_4x^4 - k_2x^2$ term is necessary for obtaining the double-well feature, while the k_1x term is necessary in order to account for asymmetry between the reactant and product wells ($k_1 = 0$

gives rise to a symmetrical double-well free energy profile, which corresponds to an iso-energetic chemical reaction). It should be noted that a third order x^3 term is excluded. This is to facilitate mapping onto the Hamiltonian of currently accessible experimental Kerr-Cat devices (see below), and justified by the fact that adding a x^3 term is not necessary for capturing the main features associated with a chemical reaction, namely an asymmetrical double-well profile.

For context, we also provide in Table 1 the values of the parameters$\{k_1, k_2, k_4\}$ for four demonstrative realizations of the Hamiltonian in Eq. (2.3) that correspond to typical proton transfer reactions, with m= 1836 amu (see FIG. 10). In what follows, we will demonstrate the utility of our protocol by showing how it can be used to simulate the chemical dynamics of those four chemical systems on the Kerr-Cat device.

Table 1: Parameters used to simulate double-well potential of relevant chemical systems, according to the equation $V_{\text{fit}} = k_4x^4 - k_2x^2 + k_1x$.

System	$k_4[E_h/a_0^4]$	$k_2[E_h/a_0^2]$	$k_1[E_h/a_0]$
Adenine-Thymine (DNA)	0.000064	0.0032	0.0058
Guanine-Cytosine (DNA)	0.00077	0.0069	0.0045
Malonaldehyde (cis-trans)	0.000094	0.0030	0.0029
Malonaldehyde (cis-cis)	0.00071	0.0040	0

Noting that the double-well and Kerr-Cat Hamiltonians in Eqs. (2.3) and (2.1), respectively, are both given by fourth-order polynomials determined by four free parameters ($\{m, k_1, k_2, k_4\}$ and $\{\Delta, K, \epsilon_1, \epsilon_2\}$, respectively), our goal in the next step is to map the Kerr-Cat Hamiltonian in Eq. (2.1), onto the chemical double-well Hamiltonian in Eq. (2.3). To this end, we first need to map the photonic operators, $\{\hat{a}, \hat{a}^\dagger\}$ onto the operators associated with motion along the reaction coordinate, $\{\hat{x}, \hat{p}\}$. To generate the correct dynamics, the mapping needs to be consistent with the corresponding commutators: $[\hat{x}, \hat{p}] = i\hbar$ and $[\hat{a}, \hat{a}^\dagger] = \hat{1}$. A mapping that satisfies this is given by:

$$\hat{a} = \frac{1}{\sqrt{2}}\left(\frac{1}{c}\hat{x} + \frac{ic}{\hbar}\hat{p}\right), \qquad \hat{a}^\dagger = \frac{1}{\sqrt{2}}\left(\frac{1}{c}\hat{x} - \frac{ic}{\hbar}\hat{p}\right) \tag{2.4}$$

Here, c is a constant parameter that has units of length (same units as $\hat{x}$). Importantly, the value of c is arbitrary in the sense that the commutators $[\hat{x}, \hat{p}] = i\hbar$ and $[\hat{a}, \hat{a}^\dagger] = \hat{1}$ are invariant to the choice of c. In other words, the mapping of $\{\hat{a}, \hat{a}^\dagger\}$ onto$\{\hat{x}, \hat{p}\}$ is not unique. As we will see below, this flexibility with respect to the choice of c plays an crucial role in mapping the Kerr-Cat Hamiltonian in Eq. (2.1), onto the chemical double-well Hamiltonian in Eq. (2.3).

Substituting the expressions for $\hat{a}$ and $\hat{a}^\dagger$ in terms of $\hat{x}$ and $\hat{p}$ from Eq. (2.4) into Eq. (2.1), we can recast the *negative* of the Kerr-Cat Hamiltonian in terms of the $\hat{x}$ and $\hat{p}$ (dropping constant terms which do not impact the dynamics):

$$\begin{aligned} -\hat{H}_{KC} = &\frac{c^2}{\hbar^2}(\epsilon_2 - K - \Delta/2)\hat{p}^2 + \frac{K}{4c^4}\hat{x}^4 - \frac{1}{c^2}(\epsilon_2 + K + \Delta/2)\hat{x}^2 - \frac{\epsilon_1\sqrt{2}}{c}\hat{x} \\ &+ \frac{Kc^4}{4\hbar^4}\hat{p}^4 + \frac{K}{4\hbar^2}(\hat{x}^2\hat{p}^2 + \hat{p}^2\hat{x}^2) \end{aligned} \tag{2.5}$$

Comparing Eq. (2.5) with Eq. (2.3), we see that while $-\hat{H}_{KC}$ contains $\hat{p}^2$, $\hat{x}^4$, $\hat{x}^2$ and $\hat{x}$ terms which can be mapped onto the corresponding terms in the chemical double-well Hamiltonian in Eq. (2.3), it also contains spurious $\hat{p}^4$, $\hat{x}^2\hat{p}^2$, $\hat{p}^2\hat{x}^2$ terms that lack counterparts in Eq. (2.3).

In the next step, we map $\{\Delta, K, \epsilon_2, \epsilon_1\}$ onto $\{m, k_1, k_2, k_4\}$ by requiring consistency between the $\hat{p}^2$, $\hat{x}^4$, $\hat{x}^2$ and $\hat{x}$ terms in Eqs. (2.3) and (2.5), which leads to the following mapping relations:

$$K = 4c^4k_4 \tag{2.6}$$

$$\epsilon_2 = \frac{\hbar^2}{4c^2m} + \frac{c^2k_2}{2} \tag{2.7}$$

$$\Delta = -\frac{\hbar^2}{2c^2m} + c^2k_2 - 8c^4k_4 \tag{2.8}$$

$$\epsilon_1 = \frac{ck_1}{\sqrt{2}} \tag{2.9}$$

It should be noted that according to Eqs. (2.6-2.9), the value of c dictates the values of $\{K, \Delta, \epsilon_1, \epsilon_2\}$.

We also take advantage of the aforementioned flexibility in choosing the value of c to minimize the effect of the spurious $\hat{p}^4$, $\hat{x}^2\hat{p}^2$, $\hat{p}^2\hat{x}^2$ terms in Eq. (2.3). As we show in the SI, doing so requires that we choose a value of c small enough so that it satisfies the following inequality:

$$\frac{\hbar^2}{mk_2c^4} \gg 1 \tag{2.10}$$

In the next step, we compare the values of energy levels of the Kerr-Cat and double-well Hamiltonians, Eqs. (2.5) and (2.3), respectively. Generally speaking those energy levels are expected to be *different* due to the spurious $\hat{p}^4$, $\hat{x}^2\hat{p}^2$, $\hat{p}^2\hat{x}^2$ terms the Kerr-Cat Hamiltonian that are missing from the double-well Hamiltonian. However, the deviations between the energy levels of both Hamiltonians are expected to diminish with decreasing c [see Eq. (2.10) and FIGS. 12A-D]. To determine a criterion for what would be an acceptable value of$c$, we set the tolerance for deviations between the energy levels of the Kerr-Cat and double-well Hamiltonians at 1.5 mE_h = 0.941 kcal/mol, which is a commonly used measure of chemical accuracy. It should be noted that accurately capturing chemical barrier crossing dynamics requires this level of chemical accuracy for excited energy levels up to the vicinity of the barrier top and not just for the ground state.

For example, the number of states necessary for capturing chemical dynamics in the aforementioned prototypical proton transfer chemical reactions are 6 for cis-cis malonaldehyde (FIG. 11A), 24 for cis-trans malonaldehyde (FIG. 11B), 32 for adenine-thymine (FIG. 11C) and 14 for guanine-cytosine (FIG. 11D). Having the energy levels of the Kerr-Cat device and chemical double well Hamiltonians within chemical accuracy of each other was also found to correspond to excellent agreement between the corresponding eigenfunctions of the two Hamiltonians (the so-called stationary state, see FIGS. 11A-D and 12A-D, panels I).

Using the cQED device to encode $\hat{H}_{DW}$, requires a finite, non-zero value for the K parameter and thus the units of Δ, ϵ_2 and ϵ_1 are expressed in terms of K. We observe that for vanishingly small values of c, the values of $\frac{\Delta}{K}, \frac{\epsilon_2}{K}, \frac{\epsilon_1}{K}$ have large magnitude, beyond the experimental feasibility of currently available cQED platforms (FIGS. 12A-D, panels II). Nonetheless, for some value of c we have experimentally accessible parameters with some degree of accuracy for the energies and stationary states. In particular, the cis-cis malonaldehyde Hamiltonian is both experimentally accessible and fulfills the chemical accuracy criterion for the stationary states and energies. Naturally, the asymmetric chemical problems are more challenging partly due to the number of eigenstates required to answer a kinetics question. Increasing the upper magnitude bound of experimental parameters could enable the ability to accurately simulate these more challenging double-well problems, although this could also lead to the breakdown of the effective Hamiltonian approximation.

Device Dynamics vs Chemical Dynamics

While establishing self-consistency between the energy levels and stationary states of $\hat{H}_{KC}$ and $\hat{H}_{DW}$ is a necessary condition for being able to simulate chemical dynamics on the Kerr-Cat device, it is not a sufficient condition. This is because chemical dynamics is typically described in terms of a *reaction rate constant*, and the fact that establishing such rate kinetics requires coupling the reaction coordinate to a thermal bath of *nonreactive* DOF. As a result, the actual reaction rate constant is dictated not just by the energy levels and eigenfunctions of the Hamiltonian, but also by bath parameters such as temperature and dissipation rates.

Thus, being able to simulate chemical dynamics on the Kerr-Cat device actually requires that the dynamics of the device is dissipative and the ability to control dissipation parameters. Luckily, the dynamics of the Kerr-Cat device, which is described in terms of the Lindblad equation, Eq. (2.2), is also subject to dissipation, which can be controlled by adjusting the photon loss rate, κ, and device operating temperature, set by n_{th}.

In what follows, we therefore consider the case of a chemical system subject to the same kind of dissipation as the Kerr-Cat device. It should be noted that this turns out to be a reasonable choice, since it gives rise to chemical dynamics that can be characterized by a reaction rate constant. At the same time, it should also be pointed out that this choice of dissipation mechanism is not unique, in the sense that the dissipation that a chemical system is subject to is typically determined by the nature of its chemical environment and the way the reaction coordinate is coupled to it (e.g. liquid solution, biological environment, solid-state environment, etc.). Hence, characterizing the actual dissipation that a chemical system is subject to and replicating it on the Kerr-Cat device remain open challenges to be addressed by future studies that will focus on dissipation characterization and engineering.

Assuming that the chemical system is subject to the same kind of dissipation as the Kerr-Cat device, we use Eq. (2.4) to cast the dissipator in Eq. (2.2) in terms of the same $\hat{x}$ and $\hat{p}$ that form the operator basis of the chemical double-well Hamiltonian, Eq. (2.3). This leads to the following Lindblad equation for the chemical system:

$$\frac{\partial\hat{\rho}}{\partial t} = -\frac{i}{\hbar}\left[\hat{H}_{DW},\hat{\rho}\right] + \frac{\kappa(1+2n_{th})}{4}\left[\frac{1}{c^2}\left([\hat{x}\hat{\rho},\hat{x}] + [\hat{x},\hat{\rho}\hat{x}]\right) + \frac{c^2}{\hbar^2}\left([\hat{p}\hat{\rho},\hat{p}] + [\hat{p},\hat{\rho}\hat{p}]\right)\right] - \frac{i\kappa}{4\hbar}\left([\hat{x}\hat{\rho},\hat{p}] + [\hat{x},\hat{\rho}\hat{p}] - [\hat{p}\hat{\rho},\hat{x}] - [\hat{p},\hat{\rho}\hat{x}]\right). \tag{2.11}$$

We note that the initial state for the dynamics propagation is localized on the reactant well for the exergonic processes of the aforementioned reactions. To generate such a state, we diagonalize the system Hamiltonian and select the first eigenstate with more than 50% density on the reactant well and apply a sigmoidal filter function to remove the excess density outside of it (see Initial State in SI for additional implementation details). This localization scheme is general and bypasses an additional step of finding the critical points of each potential and generating a localized Gaussian state.

Thus, solving Eq. (2.11) for an initial state $\hat{\rho}(0)$ which is localized on the reactant well to obtain the state at a later time *t*, $\hat{\rho}(t)$, the product population at time *t* is given by:

$$P_P(t) = \mathrm{Tr}\{\hat{\rho}_t \widehat{\Theta}_X\} \qquad (2.12)$$

Here, $\widehat{\Theta}_X$ is Heaviside's function:

$$\langle x|\widehat{\Theta}_X|x'\rangle = \begin{cases} 0 & \text{for } x < 0 \\ \delta(x - x') & \text{for } x > 0 \end{cases} \qquad (2.13)$$

The reactant-to-product reaction rate constant, $k = 1/T_x$, can then be obtained by fitting $P_P(t)$ to an exponential (with a complete protocol outlined in the Observables section).

The time evolution of $P_P(t)$ for the aforementioned four representative proton transfer reactions, obtained by solving Eq. (2.11) for different values of *c* are shown in FIGS. 13A-D, alongside the dependence of the corresponding inverse reaction rate constant, T_x, as a function of *c* in the range (0.05, 1.0) (solid lines). Also shown on those plots are the corresponding results where the chemical double-well Hamiltonian in Eq. (2.11), $\widehat{H}_{DW}$, is replaced by the corresponding device Hamiltonian $-\widehat{H}_{KC}$ that includes the spurious $\hat{p}^4$, $\hat{x}^2\hat{p}^2$ and $\hat{p}^2\hat{x}^2$ terms (diamonds and dashed lines).

Close inspection of the results in FIGS. 13A-D shows that the dynamics of both the chemical system and Kerr-Cat device is consistent with rate kinetics that can be described in terms of a rate constant. Furthermore, the reaction rate constant is seen to be significantly less sensitive to the value of *c* compared to the energy levels and eigenfunctions of $\widehat{H}_{DW}$ and $\widehat{H}_{KC}$. More specifically, the rate constant predicted by the device is seen to coincide with that predicted for the chemical system at values of *c* which are larger than those necessary for the energy levels and eigenfunctions up to the vicinity of the barrier top to coincide.

While the results in FIGS. 13A-D are for the case κ= 0.1, n_{th} = 0.1, the trends observed are insensitive to the values of κ and n_{th}. To demonstrate this, the dependence of the rate constants for both the chemical double well and the Kerr-Cat device as obtained at different values of κ and n_{th} are shown in table 2 for the case *c*= 0.1. As expected, T_x increases (i.e. the reaction slows down) with decreasing κ and n_{th}. However, the actual values of T_x for the chemical double well and the Kerr-Cat device are the same for given values of κ and n_{th}.

Table 2: Table of inverse reaction rate constants for each chemical system and corresponding device simulation, for different values of dissipation parameters κ, n_{th} for c=0.1

Dissipation Constants (κ, n_{th})	(0.1,0.1)	(0.1,0.05)	(0.025,0.1)	(0.025,0.05)
Cis-cis Malonaldehyde (KC)	90.67±1.14	90.65±1.10	302.85±3.90	294.78±3.81
Cis-cis Malonaldehyde (DW)	90.68±1.14	90.66±1.10	302.86±3.90	294.79±3.81
Cis-trans Malonaldehyde (KC)	146.71±1.95	141.56±1.68	527.34±7.21	499.28±6.39
Cis-trans Malonaldehyde (DW)	146.86±1.95	141.73±1.69	527.58±7.22	499.53±6.39
Adenine-Thymine (KC)	234.78±2.55	200.80±1.77	948.98±10.54	825.08±7.36
Adenine-Thymine (DW)	235.05±2.56	201.03±1.77	949.98±10.55	825.89±7.36
Guanine-Cytosine (KC)	95.91±1.31	95.48±1.24	324.94±4.50	315.64±4.35
Guanine-Cytosine (DW)	95.91±1.31	95.49±1.24	324.95±4.50	315.65±4.35

Outlook

Proposed herein is a new approach to simulating chemical dynamics on a tunable Kerr-Cat device. Within this approach, one has control over the parameters that define the double-well free energy profile, as well as external parameters such as the temperature and dissipation rates. The new approach is also demonstrated on four prototypical proton transfer reactions by showing how the underlying chemical dynamics can be accurately simulated on a Kerr-Cat device.

Simulating chemical dynamics on a Kerr-Cat device requires overcoming several challenges. One challenge, which we focused on in this Example, is mapping the chemical double-well Hamiltonian onto the Kerr-Cat device Hamiltonian. This is nontrivial since the Kerr-Cat device Hamiltonian contains spurious $\hat{p}^4$, $\hat{x}^2\hat{p}^2$, $\hat{p}^2\hat{x}^2$ terms that are missing from the chemical Hamiltonian. In this Example, we proposed a way to minimize the effect of those spurious terms by adjusting the value of the parameter c within the mapping of the photonic operators $\hat{a}$ and $\hat{a}^\dagger$ onto the chemical operators $\hat{x}$ and $\hat{p}$. More specifically, we have shown that the energy levels and stationary states of the Kerr-Cat and chemical Hamiltonians can be made to coincide (within a certain level of tolerance that corresponds to chemical accuracy) by choosing a sufficiently small value of c. Furthermore, we have also found that the reaction rate constants were even less sensitive to the value of c than the energy levels and stationary states, and therefore easier to reproduce by simulating the chemical dynamics on the Kerr-Cat device.

EXAMPLE 3 – Supporting Information for Example 2

Mapping the Effective Device Hamiltonian to Chemical Double-Well

We start out by considering the following general Hamiltonian which is suitable for modeling the dynamics of a wide range of elementary chemical reactions:

$$\hat{H}_{DW} = \frac{\hat{p}^2}{2m} + k_4\hat{x}^4 - k_2\hat{x}^2 + k_1\hat{x} \tag{3.1}$$

Here, $\hat{x}$ and $\hat{p}$ are the position and momentum operators associated with motion along the reaction coordinate, which satisfy $[\hat{x}, \hat{p}] = i\hbar$; m is the mass associated with the motion along the reaction coordinate; and $\{k_1, k_2, k_4\}$ are positive and real parameters whose values define the double well free energy profile, and thereby the specific chemical system, that the Hamiltonian describes. More specifically, given the double-well free energy profile for a specific chemical system, which can be obtained from electronic structure and MD simulations, we assume that it can be fitted to a minimal fourth-order polynomial of the form $V(x) = k_4x^4 - k_2x^2 + k_1x$. A schematic of the free energy double-well profile, $V(x)$, along the reaction coordinate, x, is shown in FIG. 14. The $k_4x^4 - k_2x^2$ term is necessary for obtaining the double-well feature, while the k_1x term is necessary in order to account for asymmetry between the reactant and product wells ($k_1 = 0$ gives rise to a symmetrical double-well free energy profile, which corresponds to an iso-energetic chemical reaction for which $\Delta G = 0$). It should be noted that a third order x^3 term is excluded. This is necessary for mapping onto the Hamiltonian of currently accessible experimental Kerr-Cat devices (see below), and justified by the fact that adding a x^3 term is not necessary for capturing the main features associated with a chemical reaction, namely an asymmetrical double-well profile. It should also be noted that a description of the chemical dynamics in terms of a TST/Arrhenius-like rate constant requires coupling the reaction coordinate to a thermal bath of nonreactive DOF in order to make activation to the transition state and barrier crossing possible, followed by equilibration in the product well before significant recrossing can occur (see below). We consider the effective Hamiltonian for currently experimentally realizable parametrically-driven Kerr-Cat cQED devices, which is given by:

$$\hat{H}_{KC} = \Delta\hat{a}^\dagger\hat{a} - K(\hat{a}^\dagger)^2(\hat{a})^2 + \epsilon_2(\hat{a}^2 + \hat{a}^{\dagger 2}) + \epsilon_1(\hat{a} + \hat{a}^\dagger) \tag{3.2}$$

Here, $\hat{a}$ and $\hat{a}^\dagger$ are (unit-less) photonic creation and annihilation operators associated with the electromagnetic mode supported by the cavity, which satisfy $[\hat{a}, \hat{a}^\dagger] = \hat{1}$, and $\{\Delta, K, \epsilon_2, \epsilon_1\}$ are experimentally controllable parameters (all given in terms of energy units). Noting that the double-well and Kerr-Cat Hamiltonians in Eqs. (3.1) and (3.2), respectively, are both given by fourth-order polynomials determined by four free parameters ($\{m, k_1, k_2, k_4\}$ and $\{\Delta, K, \epsilon_2, \epsilon_1\}$, respectively), our goal in the next step is to map the Kerr-Cat Hamiltonian in Eq. (3.2), onto the chemical double-well Hamiltonian in Eq. (3.1).

To this end, we first need to map the photonic operators, $\{\hat{a}, \hat{a}^\dagger\}$ onto the operators associated with motion along the reaction coordinate, $\{\hat{x}, \hat{p}\}$. To generate the correct dynamics, the mapping needs to be consistent with the corresponding commutators: $[\hat{x}, \hat{p}] = i\hbar$ and $[\hat{a}, \hat{a}^\dagger] = \hat{1}$. A mapping that satisfies this is given by:

$$\begin{gathered} \hat{a} = \frac{1}{\sqrt{2}}\left(\frac{1}{c}\hat{x} + \frac{ic}{\hbar}\hat{p}\right) \ ; \ \hat{a}^\dagger = \frac{1}{\sqrt{2}}\left(\frac{1}{c}\hat{x} - \frac{ic}{\hbar}\hat{p}\right) \\ \hat{x} = \frac{c}{\sqrt{2}}(\hat{a} + \hat{a}^\dagger) \ ; \ \hat{p} = \frac{\hbar}{i\sqrt{2}c}(\hat{a} - \hat{a}^\dagger). \end{gathered} \tag{3.3}$$

Here, c is a constant parameter that has units of length (same units as $\hat{x}$). Importantly, the value of c is arbitrary in the sense that the commutators $[\hat{x}, \hat{p}] = i\hbar$ and $[\hat{a}, \hat{a}^\dagger] = \hat{1}$ are invariant to the choice of c. In other words, the mapping of $\{\hat{a}, \hat{a}^\dagger\}$ onto $\{\hat{x}, \hat{p}\}$ is not unique. As we will see below, this flexibility with respect to the choice of c plays an crucial role in mapping the Kerr-Cat Hamiltonian in Eq. (3.2), onto the chemical double-well Hamiltonian in Eq. (3.1).

Substituting the expressions for $\hat{a}$ and $\hat{a}^\dagger$ in terms of $\hat{x}$ and $\hat{p}$ from Eq. (3.3) into Eq. (3.2), we can recast the *negative* of the Kerr-Cat Hamiltonian in terms of the $\hat{x}$ and $\hat{p}$ (dropping constant terms which do not impact the dynamics):

$$\begin{aligned} -\hat{H}_{KC} = {} & \frac{c^2}{\hbar^2}(\epsilon_2 - K - \Delta/2)\hat{p}^2 + \frac{K}{4c^4}\hat{x}^4 - \frac{1}{c^2}(\epsilon_2 + K + \Delta/2)\hat{x}^2 - \frac{\epsilon_1\sqrt{2}}{c}\hat{x} \\ & + \frac{Kc^4}{4\hbar^4}\hat{p}^4 + \frac{K}{4\hbar^2}\hat{x}^2\hat{p}^2 + \frac{K}{4\hbar^2}\hat{p}^2\hat{x}^2 \end{aligned} \tag{3.4}$$

Comparing Eq. (3.4) with Eq. (3.1), we see that while $-\hat{H}_{KC}$ contains $\hat{p}^2$, $\hat{x}^4$, $\hat{x}^2$ and $\hat{x}$ terms which can be mapped onto the corresponding terms in the chemical double-well Hamiltonian in Eq. (3.1), it also contains spurious $\hat{p}^4$, $\hat{x}^2\hat{p}^2$, and $\hat{p}^2\hat{x}^2$ terms that lack counterparts in Eq. (3.1).

In the next step, we map $\{\Delta, K, \epsilon_2, \epsilon_1\}$ onto $\{m, k_1, k_2, k_4\}$ by requiring consistency between the $\hat{p}^2$, $\hat{x}^4$, $\hat{x}^2$ and $\hat{x}$ terms in Eqs. (3.1) and (3.4), which leads to the following mapping relations:

$$K = 4c^4k_4 \tag{3.5}$$

$$\epsilon_2 = \frac{\hbar^2 + 2c^4k_2m}{4c^2m} \tag{3.6}$$

$$\Delta = \frac{2c^4k_2m - \hbar^2 - 16c^6k_4m}{2c^2m} \tag{3.7}$$

$$\epsilon_1 = \frac{ck_1}{\sqrt{2}} \tag{3.8}$$

We also take advantage of the aforementioned flexibility in choosing the value of *c* to minimize the effect of the spurious $\hat{p}^4$, $\hat{x}^2\hat{p}^2$, and $\hat{p}^2\hat{x}^2$ terms in Eq. (3.1). As we show below, doing so requires that we choose a value of *c* small enough so that it satisfies the following inequality:

$$\frac{\hbar^2}{mk_2c^4} \gg 1 \tag{3.9}$$

To derive the inequality in Eq. (3.9), we note that the $\hat{x}^4$, $\hat{x}^2$ and $\hat{x}$ terms in Eq. (3.4) become *larger* relative to the other terms with *decreasing c*. This suggests that choosing a sufficiently small value of *c* can make the spurious p^4, x^2p^2 and x^2p^2 terms negligible. However, the fact the kinetic energy term in Eq. (3.4), $\frac{c^2}{\hbar^2}(\epsilon_2 - K - \Delta/2)\hat{p}^2$, also decreases with decreasing *c* implies that the value of *c* also needs to be chosen such that the spurious terms will be negligible compared to it. It must be noted that if one puts Eq. 3.5-3.8 in units of *K*, that being $\{\epsilon_1/K, \epsilon_2/K, \Delta/K\}$, these quantities diverge when $\lim c \to 0$, with these quantities getting quite large when c is small. So, it is necessary to pick a value of c which produces experimentally accessible values of $\{\epsilon_1/K, \epsilon_2/K, \Delta/K\}$ for a given chemical system while ensuring sufficient chemical accuracy.

To this end, we consider the symmetrical double-well case ($k_1 = 0$), for which it can be shown that the reactant and product equilibrium geometries are given by $\pm x_0$, where $x_0 = \sqrt{\frac{k_2}{2k_4}}$ and the activation energy is given by $E_a = \frac{k_2^2}{4k_4}$. Thus, $\{x_0, E_a\}$ are interchangeable with $\{k_2, k_4\}$ in this case, such that Eq. (3.5) becomes $K = \frac{4E_ac^4}{x_0^4}$. Hence,

$$\frac{K}{4\hbar^2}\left[\frac{c^4}{\hbar^2}\hat{p}^4 + \hat{x}^2\hat{p}^2 + \hat{p}^2\hat{x}^2\right] \to \frac{E_ac^4}{\hbar^2x_0^4}\left[\frac{c^4}{\hbar^2}\hat{p}^4 + \hat{x}^2\hat{p}^2 + \hat{p}^2\hat{x}^2\right] \tag{3.10}$$

Given that x_0 set the length scale of the chemical system, one can estimate the order of magnitude of the $\hat{x}^2\hat{p}^2$ and $\hat{p}^2\hat{x}^2$ terms to be $\frac{E_ac^4}{\hbar^2x_0^4}x_0^2\hat{p}^2 = \frac{E_ac^4}{\hbar^2x_0^2}\hat{p}^2$. Thus, requiring that the spurious $\hat{x}^2\hat{p}^2$ and $\hat{p}^2\hat{x}^2$ terms are negligible relative to the kinetic energy term, $\frac{\hat{p}^2}{2m}$gives rise to the inequality$\frac{E_a c^4}{\hbar^2 x_0^2}\hat{p}^2 \ll \frac{1}{2m}\hat{p}^2$, which can be rearranged to give $\frac{\hbar^2 x_0^2}{2mE_a c^4} \gg 1$. Noting that $k_2 = \frac{2E_a}{x_0^2}$ then leads to the inequality in Eq. (3.9).

The fact that the $\hat{p}^4$ term scales like c^4, while the $\hat{p}^2$ term scales like c^2, also implies that the $\hat{p}^4$ will becomes negligible for a sufficiently small value of c. In fact, the same inequality, Eq. (3.9), can be derived by nothing that $\frac{1}{2m}\hat{p}^2 \gg \frac{E_a c^8}{\hbar^4 x_0^4}\hat{p}^4$ is equivalent to $\frac{1}{2m} \gg \frac{E_a c^8}{\hbar^4 x_0^4}\hat{p}^2$ and noting that the momentum is maximal when the particle is around the minima, where the potential energy can be approximated as being harmonic. Invoking the virial theorem for the harmonic oscillator, according to which the expectation values of the kinetic energy is equal to that of the potential energy, and noting that E_a sets the potential energy scale for the chemical system, we can then estimate $\hat{p}^2$ by $2mE_a$ in the inequality $\frac{1}{2m} \gg \frac{E_a c^8}{\hbar^4 x_0^4}\hat{p}^2$, which turns it into the inequality $\left(\frac{\hbar^2 x_0^2}{2mE_a c^4}\right)^2 \gg 1$. Thus, satisfying the inequality in Eq. (3.9), which is equivalent to $\frac{\hbar^2 x_0^2}{2mE_a c^4} \gg 1$, also guarantees that the $\hat{p}^4$ term will becomes negligible compared the $\hat{p}^2$ kinetic energy term.

Finally, the argument for why the same argument would also hold for an *asymmetrical* double-well has to do with the expectation that the length and energy scales of the chemical system are not going to be significantly affected by the addition of the asymmetry.

Computational Methods

In this work, we examine the dissipative dynamics of the asymmetric Kerr-Cat Hamiltonian,

$$\frac{\hat{H}}{\hbar} = \Delta\hat{a}^\dagger\hat{a} - K(\hat{a}^\dagger)^2(\hat{a})^2 + \epsilon_2(\hat{a}^2 + \hat{a}^{\dagger 2}) + \epsilon_1(\hat{a} + \hat{a}^\dagger) \qquad (3.11)$$

where Δ, ϵ_2, ϵ_1 control the potential landscape parameters such as inter-well separation, barrier height, and well asymmetry, respectively. The entire Hamiltonian is scaled by K, which is taken to be a constant value throughout the manuscript, unless otherwise stated. The operators $a^\dagger, a$ are the quantum Harmonic oscillator excitation and de-excitation operators expressed in the basis of Fock states. To simulate the dissipative dynamics of this Hamiltonian, we use the Lindblad master equation:

$$\frac{\partial \hat{\rho}(t)}{\partial t} = -\frac{i}{\hbar}\left[\hat{H}, \hat{\rho}(t)\right] + \mathcal{D}[\hat{\rho}(t)], \tag{3.12}$$

where $\hat{H}$ is the Kerr-Cat Hamiltonian, $\hat{\rho}(t)$ is the time-dependent density matrix and $\mathcal{D}[\hat{\rho}(t)]$ is the dissipator defined as:

$$\mathcal{D}[\hat{\rho}(t)] = \kappa(1 + n_{th})\left(\hat{a}\hat{\rho}\hat{a}^{\dagger} - \frac{1}{2}\{\hat{a}^{\dagger}\hat{a}, \hat{\rho}\}\right) + \kappa n_{th}\left(\hat{a}^{\dagger}\hat{\rho}\hat{a} - \frac{1}{2}\{\hat{a}\hat{a}^{\dagger}, \hat{\rho}\}\right) \tag{3.13}$$

with $a^{\dagger}, a$ being excitation and deexcitation operators, whose effect is governed by the magnitude of the thermal parameters κ and n_{th}. To implement the Lindblad equation and simulate dissipative dynamics, we vectorize the density matrix and matricize the Lindbladian, using the relationship $\mathrm{vec}(AXB) = (B^T \otimes A)\mathrm{vec}(X)$, such that

$$\frac{\partial \hat{\rho}}{\partial t} = \hat{\mathcal{L}}\hat{\rho} \tag{3.14}$$

Thus, we must find a suitable representation for $\hat{\mathcal{L}}$. We introduce identity matrices to utilize the vectorization relationship and apply it to the Hamiltonian:

$$\begin{aligned}\left[\hat{H}, \hat{\rho}(t)\right] &= \hat{H}\hat{\rho}\mathbb{I} - \mathbb{I}\hat{\rho}\hat{H} && (3.15)\\ &= \left(\mathbb{I}\otimes\hat{H} - \hat{H}^T\otimes\mathbb{I}\right) && (3.16)\end{aligned}$$

Similarly, we can alter the dissipator:

$$\begin{aligned}\mathcal{D}[\hat{\rho}(t)] &= \kappa(1 + n_{th})\left(\hat{a}\hat{\rho}\hat{a}^{\dagger} - \frac{1}{2}(\hat{a}^{\dagger}\hat{a}\hat{\rho}\mathbb{I} + \mathbb{I}\hat{\rho}\hat{a}^{\dagger}\hat{a})\right)\\ &\quad + \kappa n_{th}\left(\hat{a}^{\dagger}\hat{\rho}\hat{a} - \frac{1}{2}(\hat{a}\hat{a}^{\dagger}\hat{\rho}\mathbb{I} + \mathbb{I}\hat{\rho}\hat{a}\hat{a}^{\dagger})\right) && (3.17)\\ &= \kappa(1 + n_{th})\left(\hat{a}^{*}\otimes\hat{a} - \frac{1}{2}(\mathbb{I}\otimes\hat{a}^{\dagger}\hat{a} + \hat{a}^{T}\hat{a}^{*}\otimes\mathbb{I})\right)\hat{\rho}\\ &\quad + \kappa n_{th}\left(\hat{a}^{T}\otimes\hat{a}^{\dagger} - \frac{1}{2}(\mathbb{I}\otimes\hat{a}\hat{a}^{\dagger} + \hat{a}^{*}\hat{a}^{T}\otimes\mathbb{I})\right)\hat{\rho} && (3.18)\end{aligned}$$

Reassembling the complete matricized Lindblad equation, we obtain

$$\begin{aligned}\dot{\hat{\rho}} = \Bigg(&\mathbb{I}\otimes\hat{H} - \hat{H}^{T}\otimes\mathbb{I}\\ &+ \kappa(1 + n_{th})\left(\hat{a}^{*}\otimes\hat{a} - \frac{1}{2}(\mathbb{I}\otimes\hat{a}^{\dagger}\hat{a} + \hat{a}^{T}\hat{a}^{*}\otimes\mathbb{I})\right)\\ &+ \kappa n_{th}\left(\hat{a}^{T}\otimes\hat{a}^{\dagger} - \frac{1}{2}(\mathbb{I}\otimes\hat{a}\hat{a}^{\dagger} + \hat{a}^{*}\hat{a}^{T}\otimes\mathbb{I})\right)\Bigg)\hat{\rho}\end{aligned} \tag{3.19}$$

To simulate the population dynamics, we integrate equation 3.14,

$$\hat{\rho}_t = \hat{\rho}(t) = e^{\hat{\mathcal{L}}t}\hat{\rho}_0 \tag{3.20}$$

and calculate the action of time-evolution of the Lindbladian operator on the propagated density matrix for a small time-step $\tau = 0.1$:

$$\hat{\rho}(t) = e^{\hat{\mathcal{L}}t}\hat{\rho}(t-\tau) \tag{3.21}$$

The matrix exponential operator is implemented using the scipy.linalg.expm routine, which implements a scaling and squaring algorithm based on Pade's approximation.

Initial State

The initial state of the system is crucial to the dynamics. We start by diagonalizing the Hamiltonian *H* to find the eigenstate matrix Φ of the system in the harmonic oscillator Fock basis:

$$H\Phi = \lambda\Phi \tag{3.22}$$

We then find the grid-based position representation (*x*) of the individual eigenstates, ϕ_i, using the quantum Harmonic oscillator basis set:

$$\phi_i = \sum_{n}^{N} c_{n,i}\psi_n(x) \tag{3.23}$$

Where $c_{n,i}$ indicate the expansion coefficients associated with eigenstate *i* and using *N* harmonic oscillator functions of the form

$$\psi_n(x) = \frac{1}{\sqrt{2^n n!}}\left(\frac{m\omega}{\pi\hbar}\right)^{1/4} e^{-\frac{m\omega x^2}{2\hbar}} H_n\left(\sqrt{\frac{m\omega}{\hbar}}x\right), \qquad n = 0,1,2,\ldots \tag{3.24}$$

In this expression, *n* indicates the order of the basis function, *m* represents the mass, ω is the fundamental frequency of the oscillator, $\hbar$ is the reduced Planck's constant and H_n are the physicist's Hermite polynomials of order *n*, which follow the following recurrence relation:

$$\begin{cases} H_0(x) = 1 \\ H_1(x) = 2x \\ \vdots \\ H_{n+1}(x) = 2xH_n(x) - 2nH_{n-1}(x) \end{cases}$$

We select a suitable initial state by finding the first state with more than 50% amplitude on the desired portion of the potential energy surface (FIG. 15, left panel) and then convolve it with a sigmoidal filter function of the form:

$$S(x; x_0, t) = \frac{1}{1+e^{-(x-x_0)/t}}, \tag{3.25}$$

where x indicates the position, x_0 indicates the cutoff position and t the smoothness of the function near the cutoff. We observe that the Heaviside function, $\Theta(x; x_0) = 1$ if $x \geq x_0$ else $\Theta(x; x_0) = 0$, is recovered when taking $\lim_{t \to 0} S(x; x_0, t)$. This allows localization of the initial state in position space which we then convert it back to the Fock basis representation (FIG. 15, right panel). All dynamics trajectories use eigenstate selection with a sigmoidal filter with a tail of 0.5.

Dynamics Subspace

The accuracy of the dynamics is dependent on the number of Fock basis states used. However, the size of the Lindbladian matrix scales as $\mathcal{O}(N^4)$ with the number of Fock states as compared to the Hamiltonian $\mathcal{O}(N^2)$, which makes matrix exponentiation (performed once for each set of Hamiltonian parameters) and multiplication (performed for each timestep in a trajectory) a limiting factor in simulation. Thus, we generate the complete Hamiltonian with a large number of Fock states (N=300) and numerically diagonalize to obtain accu- rate eigenvalues and eigenvectors and use the first M=20 states to perform as similarity transformation matrix to reduce the dynamics computational space:

$$H_{N\times N} C_{N\times N} = \lambda_{N\times N} C_{N\times N} \rightarrow D_{N\times M} \equiv C_{N\times M} \tag{3.26}$$

Where $\lambda_{N\times N}$, $C_{N\times N}$ contains the eigenvalues, eigenvectors of the Hamiltonian $H_{N\times N}$ in the full N-dimensional space and $C_{N\times M}$ represent the reduced dimensionality eigenvector matrix containing the first M eigenstates which is defined as the transformation matrix $D_{N\times M}$. Then the initial state ($\hat{\rho}_0$), the Hamiltonian (H) and the Lindbladian ladder operators ($a^\dagger$, a) are transformed into the reduced Hilbert space according to the transformation,

$$A'_{M\times M} = D^T_{M\times N} A_{N\times N} D_{N\times M} \tag{3.27}$$

As a consequence of this, the ladder operators now encode information about the properties of the Hamiltonian and thus can better simulate the dynamics of the system.

Observables

For this work, we focus on observables corresponding to traces with the time-evolved state. These include traces with the initial state corresponding to the lowest-lying state on the initial well, $\mathrm{Tr}\{\hat{\rho}_t \hat{\rho}_0\}$, and traces with the Heaviside function to obtain the population on the right side, $P_R = \mathrm{Tr}\{\hat{\rho}_t \Theta(x; x_0)\}$ or traces with the complement of the Heaviside function to obtain the population on the left, $P_L = \mathrm{Tr}\{\hat{\rho}_t (1 - \Theta(x; x_0))\}$. Finally, we look at the eigenvalues obtained by exact diagonalization of the Lindbladian to assess the principal modes/mechanisms of population transfer as well as the long-time final equilibrium state. We focus on the maximum amplitude non-zero real eigenvalue, to compute the decay time defined as follows:

$$T_X = -[\Re\lambda]^{-1} \tag{3.28}$$

which represents the slower decaying timescale of the Lindbladian. Note that this gives qualitative insight into the relaxation rate, while bypassing the more expensive requirement of performing dynamics propagation.

Basis Set Convergence

In this section, we explore the convergence of the Hamiltonian parameters to the number of Eigen-basis used. In FIGS. 16A-D, we present the timescales obtained from the exact diagonalization of the Lindblabian as a function of Hamiltonian parameters ε_1 and ε_2, for a different number of Eigen-basis. As can be appreciated, with $n_{basis} > 10$ the timescales are semi-quantitative converged, and with $n_{basis} > 20$ quantitative agreement is found. Unless otherwise stated, we used $n_{basis} = 20$.

Simulating barrier crossing dynamics on a Kerr-Cat device

Barrier crossing dynamics of the type typically observed in chemical systems requires coupling the reaction coordinate to a bath of non-reactive DOFs which acts both as an energy source for activating the chemical system from the bottom of the reactant well to the vicinity of the barrier top and as an energy sink for stabilizing the system in the product well once barrier crossing occurred. Since the Kerr-Cat Hamiltonian in Eq. (3.2) only describes the dynamics along the reaction coordinate, treating it as a closed quantum system undergoing unitary dynamics would not generate the desirable chemical dynamics. Coupling the reac- tion coordinate to a thermal bath of nonreactive DOFs takes us to the domain of *nonunitary* open quantum systems dynamics. In what follows, we will assume that this dynamics is described by the following Lindblad quantum master equation:

$$\frac{\partial\hat{\rho}(t)}{\partial t} = -\frac{i}{\hbar}\left[\hat{H}_{KC}, \hat{\rho}(t)\right] \tag{3.29}$$

$$+\kappa(1 + n_{th})\left[\hat{a}\hat{\rho}(t)\hat{a}^{\dagger} - \frac{1}{2}\{\hat{a}^{\dagger}\hat{a}, \hat{\rho}(t)\}\right] \tag{3.30}$$

$$+\kappa n_{th}\left[\hat{a}^{\dagger}\hat{\rho}(t)\hat{a} - \frac{1}{2}\{\hat{a}\hat{a}^{\dagger}, \hat{\rho}(t)\}\right] \tag{3.31}$$

$$\equiv \mathcal{L}\hat{\rho}(t) \tag{3.32}$$

Here, $\hat{\rho}(t)$ is the density operator that describes the state of the reactive system, $\hat{H}_{KC}$ is the Kerr-Cat Hamiltonian of the reactive system [Eq. (3.2)], $\{\kappa n_{th}, \kappa(n_{th}+1)\}$are parameters that determine the rates of bath-induced uphill and downhill transitions, respectively, and thereby the coupling strength between the reaction coordinate and the bath of non-reactive DOFs and $\mathcal{L}$ is the Lindbladian superoperator.

Simulating the dissipative dynamics described by Eq. (3.32) was accomplished by vectorizing the density operator and matricizing the Lindbladian superoperator, followed by diagonalizing $\mathcal{L}$ and propagating the vectorized density operator according to

$$\hat{\rho}(t) = e^{\mathcal{L}t}\hat{\rho}(0) \tag{3.33}$$

The initial state was chosen so that it is localized in the reactant well. To this end, we picked the first eigenstate of the Kerr-Cat Hamiltonian with more than 50% probablity of being in the reactant well and then multiplied it by a sigmoidal function that filtered out the part of the wave function that resides in the product well. Given this reactant-well-localized wave function, $|\psi_R\rangle$, the initial density operator is given by $\hat{\rho}(0) = |\psi_R\rangle\langle\psi_R|$ (a pure state).

The barrier crossing rate constant is given by $k = 1/T_X$, where T_X defines the barrier crossing time scale. T_X was determined in two ways:

1. As the inverse of the real value of the smallest singular value of the Lindbladian supermatrix, obtained via diagonalization, as in FIG. 17A.
2. As the time scale of decay of $Tr\{\hat{\rho}_t \Theta_X\}$, obtained via fitting to an exponential, as in FIG. 17B.

The two methods for determining T_X gave similar results and found to exhibit the same behavior when it comes to the dependence of T_X on the Kerr-Cat parameters. The results reported in the text were obtained via method 1 unless otherwise noted (FIG. 17B).

The following analysis is for the case of $\Delta = 0$, and using the convention $\hbar = 1$ and K as a unit of energy. A complete description of the methodology is included in the supporting information (SI Section Computational Methods).

The dependence of T_X on the Kerr-Cat parameters ε_1 and ε_2 is shown in FIGS. 17A-B. The plot shows a rich structure including (a) a zone in the lower right corner where the barrier crossing is very fast, which corresponds to a low barrier or a complete lack of a barrier, (b) Fast barrier crossing in the upper left corner for particular values of $(\varepsilon_1, \varepsilon_2)$ where the energy levels in the reactant and product wells are in resonance (see white lines in FIGS. 17A-B and SI), and (c) alternation between "broad" and "thin" resonance transitions both as a function of ε_1 for fixed ε_2 and along the (ε_1, ε_2) resonance line.

The fast barrier crossing regimes correspond to resonances between the energy levels in the reactant and product wells which lead to efficient tunneling through the barrier. The aforementioned "thin" regions correspond to eigenstate overlap close the top of the barrier as well as a high state density at the barrier top, providing a transient state to retain population before decaying to the global ground state (see FIG. 18A and corresponding panels S1, 2, 3 of FIG. 18C). By contrast the "broad" regimes contain degenerate states but no density centered at the top of the barrier, thus reducing the overall population transfer rate (see FIG. 18A and corresponding panels S2, 1, 4 of FIG. 18C). However, the rate is nonetheless enhanced due to the presence of quasi-degenerate states near the barrier top, providing a pathway for barrier crossing. Furthermore, the intermediate states without resonant states have longer lifetimes due to lack of overlap between eigenstates or localized state density on either side of the well (see FIG. 18A and corresponding panels N1 and N2 of FIG. 18B). Going along each of the resonance lines showcases an increasing number of degenerate pairs of states with increasing ε_2 (FIG. 18A and FIG. 18C: S1-S2; 1-2; 3-4). Going between different resonance lines with increasing ε_1 changes the first state index in resonance between the two wells (S1: first and second, 1: second and third, 3: third and fourth).

Finally, a decrease in the minimum-to-minimum height decreases the barrier height until the double-well is destroyed (FIG. 18B, W). This decreases the relaxation lifetime as the kinetics driving the process is merely vertical de-excitation to the ground state. Although there can be a relaxation timescale associated with the process this is not a measurement of the kinetics of population transfer between the wells, as this is an ill-defined process in this parameter regime.

FIGS. 19A-C show how the dependence of T_X on ϵ_1 and ϵ_2 is impacted by the strength of coupling between the reaction coordinate and the bath of nonreactive DOFs, as measured by κ. As expected, T_X shows an overall trend of increasing with decreasing coupling strength, which can be traced back to the fact that the rate of activation from the bottom of the reactant well to to the vicinity of the barrier top and stabilization in the product well after barrier crossing are determined by κ. Additionally, the dependence of T_X on ϵ_1 and ϵ_2 is seen to become less structured with increasing κ, which can be traced back to ability of dissipation to wash out resonance effects. More specifically, while tunnelling dominates the kinetics at low values of κ, classical-like barrier crossing and thereby TST/Arrhenius-like kinetics is observed at larger values of κ. A more extensive set of data that showcases this

Finally, FIGS. 20A-C show how the dependence of T_X on ϵ_1 and ϵ_2 is impacted by the bath temperature, as measured by n_{th}. While T_X shows an overall increase with decreasing n_{th}, the structure is seen to be minimally impacted by changing n_{th}.

EXAMPLE 4 – “Mapping Molecular Hamiltonians into Hamiltonians of Modular cQED Processors”

ABSTRACT: We introduce a general method based on the operators of the Dyson-Masleev transformation to map the Hamiltonian of an arbitrary model system into the Hamiltonian of a circuit Quantum Electrodynamics (cQED) processor. Furthermore, we introduce a modular approach to programming a cQED processor with components corresponding to the mapping Hamiltonian. The method is illustrated as applied to quantum dynamics simulations of the Fenna-Matthews-Olson (FMO) complex and the spin-boson model of charge transfer. Beyond applications to molecular Hamiltonians, the mapping provides a general approach to implement any unitary operator in terms of a sequence of unitary transformations corresponding to powers of creation and annihilation operators of a single bosonic mode in a cQED processor.

1. Introduction

The development of quantum computing simulations for modeling chemical systems is a subject of immense interest. Recent studies have already explored the potential of quantum computing as applied to electronic structure calculations, quantum dynamics simulations, and simulations of molecular spectroscopy. Currently quantum computing facilities are often called noisy intermediate-scale quantum (NISQ) computers, due to their intrinsic limitations, including architectures based on superconducting circuits, trapped ions, and nuclear magnetic resonance. To achieve moderate accuracy and reliability in spite of noise and decoherence, simulations of chemical systems have relied on hybrid quantum-classical algorithms, including the variational quantum eigensolver (VQE) method and quantum machine learning methods where only part of the computation is performed on the quantum computer, sometimes applied with the aid of error mitigation techniques, while the rest of the calculation is run on a conventional computer.

New hardware settings that can fundamentally reduce the aforementioned errors in quantum computing architectures are necessary to enable fault-tolerant quantum computations of chemical systems. A promising paradigm-shifting technology involves the development of bosonic circuit Quantum Electrodynamics (cQED) processors, where information is stored as microwave photons in the unbounded Hilbert space of oscillator modes. The nonlinearity necessary for control and readout procedures is provided by quantum circuits based on ancillary Josephson junctions. Bosonic cQED devices offer favorable platforms for quantum error correction codes as a result of the well understood dominant source of errors in oscillator modes, namely, the single-photon loss. Moreover, encoding information in multiple levels of an oscillator can be more efficient compared to conventional cQED architectures, where the storage of information utilizes only the first two- levels of a transmon.

Bosonic cQED devices have already been shown to offer unparalleled capabilities for simulations of vibronic spectra of small molecules such as water, ozone, nitrogen dioxide, and sulfur dioxide, when mapping the calculation of Franck– Condon factors into a boson sampling problem. The corresponding calculations on a conventional quantum computer would require 8 qubits and $\mathcal{O}(10^3)$ gates, exceeding the capabilities of current technologies. Therefore, it is natural to anticipate that bosonic cQED devices could be applied to solve other classes of interesting problems in chemistry and offer advantages beyond the capabilities of conventional quantum computers. However, a general approach to design a quantum circuit to simulate an arbitrary molecular system has yet to be established. Here, we address the fundamental question regarding how to map the Hamiltonian of a molecular system to the corresponding Hamiltonian of a programmable bosonic cQED simulator. We introduce the single-bosonic-mode (SBM) mapping, allowing us to represent any square matrix as a polynomial of creation and annihilation operators of a bosonic mode. The mapping thus provides a general protocol for transforming any Hamiltonian into the Hamiltonian of a cQED device, since the Hamiltonian of a cQED device can be written as a polynomial of creation and annihilation operators of a single bosonic mode. Additionally, we introduce a modular approach to program a cQED processor according to the SBM mapping Hamiltonian. In particular, we identify circuits with Superconducting Nonlinear Asymmetric Inductive eLements (SNAILs) that could be coupled by beam splitters, or by nearly quartic elements for programming one-qubit gates and the two-qubit controlled-Z gate that enable universal computing.

We illustrate the SBM mapping in conjunction with SNAIL gates as applied to model simulations of quantum dynamics in the photosynthetic Fenna-Matthews-Olson (FMO) complex, a system that mediates excitation energy transfer from light-harvesting chlorosomes to the bacterial reaction center. Additionally, we illustrate the SBM mapping as applied to simulations of charge or energy transfer processes with dissipation according to the spin-boson model. Beyond applications to molecular Hamiltonians, the SBM mapping provides a general approach for implementing any unitary operator in terms of a sequence of unitary transformations corresponding to powers of creation and annihilation operators of single-bosonic modes in a cQED processor.

The rest of the article is organized as follows. Section 2 introduces the SBM mapping method. Section 3 provides the implementation of one-qubit gates with capacitively shunted SNAILs, and the two-qubit controlled-Z gate with nearly quartic elements. Section 4 demonstrates the SBM mapping with SNAIL circuit implementation, as applied to quantum dynamics simulations of a series of models typically employed to simulate charge and energy transfer processes. Conclusions are outlined in section 5.

2. Single-Bosonic Mode Mapping

The SBM mapping transforms an arbitrary Hermitian operator,

$$\hat{H} = \sum_{\alpha=0}^{k-1} \sum_{\alpha'=0}^{k-1} H_{\alpha\alpha'} |\alpha\rangle\langle\alpha'| \tag{4.1}$$

in the basis set $\{|\alpha\rangle\}$ of the system of interest, into the following polynomial of products of powers of operators of a single bosonic mode $(\hat{a}, \hat{a}^{\dagger})$, as follows:

$$\hat{H}_{\mathrm{sbm}} = \sum_{m=0}^{k-1} \sum_{n=0}^{k-1} H_{nm} \hat{P}_{nm} \tag{4.2}$$

where

$$\hat{P}_{nm} \equiv \frac{1}{(k-1)!^2} \sqrt{\frac{m!}{n!}} (\hat{a}^{\dagger})^n \hat{\Gamma}_k^{k-1} (\hat{a}^{\dagger})^{k-1-m} \tag{4.3}$$

with

$$\hat{\Gamma}_k = ((k-1) - \hat{N})\hat{a} \tag{4.4}$$

Where $\hat{N} = \hat{a}^\dagger \hat{a}$. Appendix A shows that $\hat{\Gamma}_k$ corresponds to the operator $\hat{S}_+^\dagger$ of the Dyson-Maleev transformation.

To derive the mapping introduced by eq 4.2, we map the operators $|a\rangle\langle a'|$ introduced by eq 4.1 into the corresponding transition operators $|m\rangle\langle n|$ in the basis of the 1-dimensional harmonic oscillator (HO), satisfying

$$\hat{a}|m\rangle = \sqrt{m}|m-1\rangle,\ \hat{a}^\dagger|m\rangle = \sqrt{m+1}|m+1\rangle$$

We can verify that

$$|0\rangle\langle k-1| = \frac{\hat{\Gamma}_k^{k-1}}{(k-1)!^{3/2}} \tag{4.5}$$

in the subspace of the first k eigenstates of the HO (Appendix B). Therefore, $\frac{\hat{\Gamma}_k^{k-1}}{(k-1)!^{3/2}}$ effectively acts as the transition operator $|0\rangle\langle k-1|$. As shown in Appendix B, the definition of $\hat{\Gamma}_k$ leads to a block diagonal representation of operators. For example, for $k = 3$, we obtain

$$\frac{\hat{\Gamma}_3^2}{2^{3/2}} = \left(\begin{array}{ccc|ccccc}
0 & 0 & 1 & 0 & 0 & 0 & 0 & \dots \\
0 & 0 & 0 & 0 & 0 & 0 & 0 & \dots \\
0 & 0 & 0 & 0 & 0 & 0 & 0 & \dots \\
\hline
0 & 0 & 0 & 0 & 0 & \sqrt{10} & 0 & \dots \\
0 & 0 & 0 & 0 & 0 & 0 & 3\sqrt{15} & \dots \\
0 & 0 & 0 & 0 & 0 & 0 & 0 & \dots \\
0 & 0 & 0 & 0 & 0 & 0 & 0 & \dots \\
\dots & \dots & \dots & \dots & \dots & \dots & \dots & \ddots
\end{array}\right),$$

showing that the matrix representation of $|0\rangle\langle 2|$ is indeed recovered from the top 3×3 diagonal block.

Next, substituting eq 4.5 into the expression of $|n\rangle\langle m|$, and considering that $|n\rangle = \frac{(\hat{a}^\dagger)^n}{\sqrt{n!}}|0\rangle$ and $\langle m| = \langle k-1|(\hat{a}^\dagger)^{k-m-1}\sqrt{\frac{m!}{(k-1)!}}$, we obtain that any operator $\hat{P}_{nm} = |n\rangle\langle m|$, with $n, m < k$ can be represented according to eq 4.3.

Note that eq 4.2 is an operator of a single bosonic mode, which corresponds to a single k-qudit gate for the mapping of a $k \times k$ Hamiltonian. In particular, when $k = 2$, eq 4.2 provides the mapping of any 2×2 hermitian operator into an operator of a single bosonic mode, allowing for construction of any bosonic 1-qubit gate with readily available superconducting devices.

Appendix A describes the relationship between the SBM mapping and the established Dyson-Maleev (DM) and Holstein-Primakoff (HP) mappings used to map spin operators into bosonic operators. The DM and HP mappings use one bosonic mode per spin site so they do not allow for the possibility of a single k-qudit gate. Furthermore, although both DM and HP mappings use bosonic operators, they are not able to construct the well-restricted bosonic Hamiltonian necessary for a quantum computing scheme. The DM mapping uses non- Hermitian bosonic operators that do not directly transfer to be unitary quantum gates upon exponentiation, while the operator square root term in the HP mapping is known to be hard to represent without a perturbative approach, which restricts implementation into quantum gates.

3. MODULAR QUANTUM CIRCUITS

This section introduces a modular design of quantum circuits based on driven Superconducting Nonlinear Asymmetric Inductive eLements (SNAIL) with a capacitive shunt, parametrized according to SBM Hamiltonians.

We begin by introducing the SBM mapping of 2×2 hermitian matrices describing 1-qubit gates. The operator $\hat{\Gamma}_k$ introduced by eq 4.4, with $k = 2$, is defined as follows:

$$\begin{aligned}\hat{\Gamma}_2 &= (1 - \hat{a}^\dagger\hat{a})\hat{a},\\ &= \hat{a} - \hat{a}^\dagger\hat{a}^2\end{aligned} \tag{4.6}$$

so any 2×2 matrix can be written according to eq 4.2, as follows:

$$\hat{H}_{sbm} = \sum_{j,k=1}^{2} H_{jk}\hat{P}_{jk} \tag{4.7}$$

where $\hat{P}_{12} = \hat{a} - \hat{a}^\dagger\hat{a}^2$, $\hat{P}_{22} = \hat{a}^\dagger - \hat{a}$, $\hat{P}_{11} = 1 - \hat{a}^\dagger - \hat{a}$, and $\hat{P}_{21} = \hat{a}^\dagger - (\hat{a}^\dagger)^2\hat{a}$.

Defining $H_{12} = R_{12}\mathrm{e}^{i\phi_{12}}$ with real valued R_{12} and ϕ_{12}, and introducing the substitution $\hat{b} = \hat{a}\mathrm{e}^{i\phi_{12}}$, we obtain

$$\begin{aligned}\hat{H}_{sim} &= H_{11} + (H_{22} - H_{11})\hat{b}^\dagger\hat{b} + R_{12}(\hat{b} + \hat{b}^\dagger) - R_{12}(\hat{b}^\dagger\hat{b}^2 + (\hat{b}^\dagger)^2\hat{b}),\\ &= H_{11} + (H_{22} - H_{11})\hat{b}^\dagger\hat{b} + R_{12}(\hat{b} + \hat{b}^\dagger)\\ &\quad - R_{12}\left(\frac{(\hat{b}^\dagger + \hat{b})^3}{3} - (\hat{b}^\dagger + \hat{b}) - \frac{\hat{b}^{\dagger 3} + \hat{b}^3}{3}\right), \qquad (4.8)\\ &= H_{11} + \hbar\omega\hat{b}^\dagger\hat{b} + 2R_{12}(\hat{b} + \hat{b}^\dagger) + g_3(\hat{b} + \hat{b}^\dagger)^3 + g_3(\hat{b}^{\dagger 3} + \hat{b}^3)\end{aligned}$$

where $\hbar\omega = H_{22} - H_{11}$, and $g_3 = -\frac{R_{12}}{3}$

In circuit QED, the charge and magnetic flux variables of a superconducting circuit are quantized and identified as polynomials of bosonic creation and annihilation operators. For the implementation of eq 4.8, we consider the Hamiltonian of a capacitively shunted SNAIL (FIG. 21A):

$$\hat{H}_{SPA} = \hbar\omega\hat{b}^\dagger\hat{b} + g_3(\hat{b} + \hat{b}^\dagger)^3 + g_4(\hat{b} + \hat{b}^\dagger)^4 \qquad (4.9)$$

we can readily identify the Hamiltonian $\hat{H}$, introduced by eq 4.8, as the Hamiltonian of a linearly driven (displaced) SNAIL,

$$\hat{H}_{sim} = H_{11} + 2R_{12}(\hat{b} + \hat{b}^\dagger) + \hat{H}_{SPA} + g_3(\hat{b}^{\dagger 3} + \hat{b}^3) \qquad (4.10)$$

with the fourth-order term turned off ($g_4 = 0$).

Note that the term $g_3(\hat{b}^{\dagger 3} + \hat{b}^3)$ in eq 4.10 can be produced by driving the SNAIL at a frequency of $\omega_3 \approx 3\omega$. Indeed, a four-wave mixing interaction would be able to implement such terms in a frame rotating at $\omega_3/3$. We want to emphasize that, despite the assumption of $g_4 = 0$, four-wave mixing can still be implemented by cascaded three-wave mixing processes.

More generally, a SNAIL can be substituted by an arbitrary flux-biased Josephson circuit, providing additional freedom for the choice of ω and g_3 coefficients in the Hamiltonian introduced by eq 4.9. Consequently, a wide range of combinations of coefficients H_{ij} can be engineered at the hardware level. We note that despite the generality of eqs 4.8 and 4.10, cases with $\omega \leq 0$ for a physical oscillator might be energetically unstable, which would impose limitations on the construction of arbitrary 2×2 hermitian matrices. However, it is verified in Appendix C that all of the $\hat{\mathrm{R}}_z$ and $\hat{\mathrm{R}}_x$ gates can be implemented under this restriction. As these gates constitute a one-qubit universal set, the hardware setting proposed in FIG. 21A can be used to construct arbitrary 1-qubit gates.

To establish a universal set of quantum gates, a 2-qubit entangling gate (e.g., a controlled-Z gate) is required. This requirement can be fulfilled by a modular design of driven SNAIL circuits nonlinearly coupled by nearly quartic elements, effectively described by a 4×4 Hamiltonian, as shown in FIG. 21B.

A nearly quartic element can be implemented, for instance, by a SNAIL designed with an unusual combination of Josephson junctions or a dc-SQUID. More in general, any superconducting two-terminal circuit whose potential energy function U can be approximated as

$$U(\varphi) \approx \frac{a}{4!}(\varphi - \varphi_0)^4 + O((\varphi - \varphi_0)^5) \tag{4.11}$$

can implement such a nearly quartic element. In eq 4.11, φ is the phase difference across the terminals of the superconducting circuit implementing the potential energy U and $a = \left.\frac{d^4U}{d\varphi^4}\right|_{\varphi_0}$ is the fourth-order Taylor expansion coefficient of the function U, evaluated at the point φ_0 which minimizes U. While it is possible to implement the potential energy in eq 4.11 exactly, in practice, any two-terminal circuit including one or more Josephson tunnel junctions is shunted by an intrinsic capacitance that introduces a weak linear coupling between the two terminals. Such linear capacitive coupling arises from the intrinsic capacitance of the Josephson tunnel junctions and can be neglected when the fourth order nonlinearity implemented by U is the dominant coupling mechanism between the two terminals (i.e., the “nearly quartic” coupling limit).

A nearly quartic element can be used to implement ultrastrong cross-Kerr couplings between photonic modes described by the interaction Hamiltonian,

$$\hat{H}_{\text{cross-Kerr}} = \chi \hat{b}_1^\dagger \hat{b}_1 \hat{b}_2^\dagger \hat{b}_2 \tag{4.12}$$

where $\hat{b}_1$ and $\hat{b}_2$ are the annihilation operators of the two coupled photonic modes. The nearly pure and ultrastrong cross-Kerr coupling can enable the construction of many photonic 2-qubits gates, including a controlled-Z gate as shown in Appendix D. Therefore, with a combination of one-qubit gates and the two-qubit gate, constructed as quartic-connected SNAILs, it is possible to map any physical Hamiltonian into a modular cQED processor.

Design of a multiple-qubit entangling gate is realized by the circuit of multiple SNAILs coupled with nearly quartic elements. As an example, FIG. 21C illustrates the circuit that effectively maps the 8 × 8 Hamiltonian corresponding to a 3-qubit entangling gate. Alternatively, bilinear couplings can also be established by beams splitters, as previously investigated for transmons. The 4 × 4 and 8 × 8 circuits in FIGS. 21B-C can be generalized as well to include arbitrary flux-biased Josephson circuits as a replacement for the SNAILs and the nearly quartic couplers.

4. DYNAMICS OF CHARGE AND ENERGY TRANSFER

A variety of important dynamical processes in molecular systems of chemical, biological, and technological importance involve electronic energy and charge transfer. The simulation of the inherently quantum-mechanical electronic dynamics underlying these processes is a subject of great interest. In this section, we illustrate the SBM mapping based on the SNAIL circuit as applied to quantum dynamics simulations of energy and charge transfer in model systems, including a multilevel system describing energy transfer in the FMO light-harvesting complex, and a spin-boson model that describes charge transfer in the presence of dissipation, schematically represented in FIG. 22.

4.1. Two-Level System (TLS). The simplest model of energy or charge transfer is given by the 2 × 2 donor−acceptor Hamiltonian,

$$\hat{H}_{TLS} = \begin{pmatrix} -\varepsilon & \Delta \\ \Delta & \varepsilon \end{pmatrix} \tag{4.13}$$

describing two coupled electronic states, with $\varepsilon = 50\ \text{cm}^{-1}$ and $\Delta = 20\ \text{cm}^{-1}$ for a typical charge transfer process in molecules. To map the 2 × 2 Hamiltonian into the circuit of FIG. 21A, the SNAIL parameters are obtained according to eq 4.10, with oscillator frequency $\omega = 100\ \text{cm}^{-1}$, linear displacement $R_{12} = 50\ \text{cm}^{-1}$ and third-order coupling $g_3 = -16.7\ \text{cm}^{-1}$. With these parameters, the right side of eq 4.10 is programmed on a classical computer and numerically exponentiated to obtain the corresponding propagator for dynamics simulations. FIG. 24 (top) shows the simulation results for the time-dependent population of the donor state. The exact agreement with benchmark calculations obtained by numerically integrating the Schrödinger equation demonstrates the SBM mapping and the proposed SNAIL-based circuit.

4.2. Fenna-Matthews-Olson Complex. Energy transfer through the chlorophyll pigments of the Fenna-Matthews-Olson (FMO) complex corresponds to exciton transfer across chromophore sites. FIG. 22 shows the seven chromophores in each monomer of the FMO complex, where the arrows depict the energy transfer pathways. For the sake of simplicity, we consider energy transfer through sites 1-4. The excitons are modeled as hard-core bosons, according to the Frenkel exciton Hamiltonian,

$$H = E_j \sum_{j}^{4} \sigma_j^+ \sigma_j^- + J_{jk} \sum_{j,k}^{4} \left(\sigma_j^+ \sigma_k^- + \sigma_k^+ \sigma_j^-\right) \tag{4.14}$$

where σ_j^+ and σ_j^- are the Pauli-raising operator and lowering operators, corresponding to the creation and annihilation of an excitation in chromophore j, with commutation rules $[\sigma_j^-, \sigma_k^+] = \delta_{jk}(\sigma_j^+ \sigma_k^-)$.

The parameters of the 4-site Hamiltonian are contained in the following 4 × 4 Hamiltonian matrix:

$$\hat{H}_{FMO} = \begin{pmatrix} 310.0 & -97.9 & 5.5 & -5.8 \\ -97.9 & 230.0 & 30.1 & 7.3 \\ 5.5 & 30.1 & 0.0 & -58.8 \\ -5.8 & 7.3 & -58.8 & 180.0 \end{pmatrix} \tag{4.15}$$

with parameters in cm^{-1}. Diagonal terms correspond to the energies of the chromophore (E_j in eq 4.14) while off-diagonal terms are the couplings between them (J_{jk} in eq 4.14).

To parametrize the superconducting circuit for dynamics simulations, with an integration time-step τ, we obtain the propagator $\hat{U}_{FMO} = e^{-i\tau\hat{H}_{FMO}/\hbar}$ as a 4 × 4 unitary matrix. This 2-qubit gate is then transpiled in terms of SNAILs parametrized according to the set of elementary gates including 1-qubit rotations and controlled-Z gates. Note that we are able to convert the Pauli operators into single boson operators based on the SBM mapping, offering advantages over conventional bosonization methods such as the Holstein−Primakoff or the Dyson−Maleev transformation (Appendix A). Analogous implementations could also be applied to model Fermionic Hamiltonians commonly encountered in quantum chemistry, when converted into sums of tensor products of Pauli operators in conjunction with the Jordan-Wigner transformation and then mapped into bosonic gates.

To obtain the SNAIL parameters for a 1-qubit rotation $\hat{U}_{1-qubit}$ 1-qubit, we compute the effective Hamiltonian $\hat{H}_{\text{eff}} = -i\log(\hat{U}_{1-qubit})$, then we map that Hamiltonian as $\hat{H}_{\text{eff,sbm}}$ according to eq 4.10, and we obtain the corresponding rotation gate, as follows: $\hat{U}_{\text{eff,SBM}} = \mathrm{e}^{-i\hat{H}_{\text{eff,sbm}}}$. The circuit is simulated by arranging the gates $\hat{U}_{\text{eff,SBM}}$ according to the transpiled circuit diagram, with CZ gates corresponding to two SNAILs coupled by a nearly quartic element, as described in Section 3. FIG. 23 shows a schematic representation of the resulting simulation.

FIG. 24 (bottom) shows the results of simulations of the exciton dynamics for site 1, which is initially fully populated and becomes depopulated according to the energy transfer process. The agreement between the results obtained with the SBMmapped Hamiltonian and the reference calculations further demonstrates the capabilities of the SBM-SNAIL circuit design. We also simulated the SBM mapping with the qudit implementation according to eqs 4.2−4.6. The agreement with reference calculations shows the potential of SBM mapping in conjunction with multiple bosonic excitations. We note that the energy transfer process in the FMO complex is dissipative. Coupling to the environment is important for stabilizing energy transfer. However, dissipation has not been included in our calculations (FIG. 24 (bottom)) since the main purpose of our analysis was to show the capabilities of the quantum circuit to simulate fully quantum coherent dynamics.

4.3. Dynamics of Open Quantum Systems. This section demonstrates the capabilities of the modular design of quantum circuits based on SBM-mapping, as applied to dynamics simulations of open quantum systems. We focus on the spin-boson model including two electronic states coupled to a bath of displaced harmonic oscillators, described in Appendix E, recently analyzed with tensor-train thermo-field memory kernels for generalized quantum master equations.

Our propagation scheme is based on the so-called population-only Liouville space superoperator $\mathcal{P}^{\mathrm{pop}}(t)$ that satisfies the following equation:

$$\hat{\sigma}^{\mathrm{pop}}(t) = \mathcal{P}^{\mathrm{pop}}(t)\hat{\sigma}^{\mathrm{pop}}(0) \tag{4.16}$$

where $\hat{\sigma}(t) = \mathrm{Tr}_n[\hat{\rho}(t)]$ is the reduced density matrix for the electronic DOFs, with $\hat{\rho}(t)$ being the density matrix for the full vibronic system. Here, $\hat{\sigma}^{\mathrm{pop}}(t) = (\sigma_{00}(t), \sigma_{11}(t))^T$ includes only the diagonal elements of $\hat{\sigma}(t)$, which are necessary to describe the electronic population dynamics. The preparation of the superoperator $\mathcal{P}^{\mathrm{pop}}(t)$ is described in Appendix E.

We compare the elements of $\hat{\sigma}^{\mathrm{pop}}(t)$ obtained according to eq 4.16 with the corresponding time-dependent populations obtained according to the quantum computational scheme based on the SBM-mapping. To perform quantum computing simulations based on eq 4.16, we first transform $\mathcal{P}^{\mathrm{pop}}(t)$ into a unitary matrix using the Sz.-Nagy dilation theorem, as follows:

$$\mathcal{U}_{\mathcal{P}^{\mathrm{pop}}}(t) = \begin{pmatrix} \mathcal{P}^{\mathrm{pop}}(t) & \sqrt{I - \mathcal{P}^{\mathrm{pop}}(t)\mathcal{P}^{\mathrm{pop}\dagger}(t)} \\ \sqrt{I - \mathcal{P}^{\mathrm{pop}}(t)\mathcal{P}^{\mathrm{pop}\dagger}(t)} & -\mathcal{P}^{\mathrm{pop}\dagger}(t) \end{pmatrix} \tag{4.17}$$

The vectorized $v_{\sigma(0)}$ is dilated by appending ancillary zero elements as follows:

$$\begin{aligned} \hat{\sigma}^{\mathrm{pop}}(0) = (\sigma_{00}(0),\ \sigma_{11}(0))^T &\rightarrow \tilde{\sigma}^{\mathrm{pop}}(0) \\ &= (\sigma_{00}(0),\ \sigma_{11}(0),\ 0,\ 0)^T \end{aligned} \tag{4.18}$$

The dilated time-updated population-only density matrix is obtained as follows:

$$\tilde{\sigma}^{\mathrm{pop}}(t) = \mathcal{U}_{\mathcal{P}^{\mathrm{pop}}}(t)\tilde{\sigma}^{\mathrm{pop}}(0) \tag{4.19}$$

The dilation scheme thus provides the unitary matrix $\mathcal{U}_{\mathcal{P}^{\mathrm{pop}}}(t)$ governing the time-evolution of $\tilde{\sigma}^{\mathrm{pop}}(t)$, the first two digits of which agree with those of $\hat{\sigma}^{\mathrm{pop}}(t)$. Therefore, eqs 4.19 and 4.16 describe the same dynamics, with eq 4.19 allowing for simulations on a quantum device. For the spin-boson model of interest $\mathcal{U}_{\mathcal{P}^{\mathrm{pop}}}(t)$ is a 4×4 unitary matrix, corresponding to a 2-qubit gate. Therefore, the SBM-SNAIL circuit is analogous to that of the FMO 4-site model. The simulation of the circuit thus follows the scheme in FIG. 23. The transpiled circuit and the corresponding SNAIL gate parameters for $\mathcal{U}_{\mathcal{P}^{\text{pop}}}(t = 1\,\text{a.u.})$ are given in FIG. 25.

FIG. 26 shows the comparison of time-dependent populations for the two electronic states corresponding to the spin-boson model, as described by elements of $\tilde{\sigma}_{\text{sbm}}^{\text{pop}}(t)$ obtained with the SBM-mapping with SNAIL circuit scheme, and the corresponding populations $\tilde{\sigma}^{\text{pop}}(t)$ obtained directly with eq 4.19, with initial condition $\tilde{\sigma}^{\text{pop}}(0) = (1,0,0,0)^T$. The excellent agreement demonstrates the capabilities of the SBM mapping as applied to a model of electron transfer with dissipation due to coupling to a surrounding environment.

5. Concluding Remarks

We have introduced a general method to map the Hamiltonian of molecular systems to the Hamiltonian of quantum circuits for cQED simulations. Additionally, we have identified the nonlinear bosonic components that need to be assembled for a modular implementation of the corresponding circuit Hamiltonians. We have illustrated the SBM mapping, in conjunction with SNAIL circuits, as applied to simulations of energy transfer in the photosynthetic FMO model system and charge transfer in donor−acceptor systems coupled to a dissipative environment.

Beyond the modular design based on SNAILs, we have shown that the SBM mapping allows for implementation of Hamiltonians on the basis of qudits (i.e., eq 4.2, with $N > 2$), corresponding to continuous-variable (CV) modes represented as N-dimensional discrete-variable (DV) states. These DV states could naturally implement the well-known Discrete Variable Representation (DVR), extensively used for the representation of molecular Hamiltonians. The SBM, therefore, offers a convenient mapping for simulations of chemical systems on the cQED platforms.

For circuits with multiple qudits, the cross-Kerr Hamiltonian may also be generalized to perform a qudit controlled-Z gate, allowing for construction of a universal set of gates for simulations on bosonic devices. The hardware efficiency of a qudit-based cQED can significantly reduce the circuit depth and simplify the experimental setup.

EQUIVALENTS

Although preferred embodiments of the invention have been described using specific terms, such description is for illustrative purposes only, and it is to be understood that changes and variations may be made without departing from the spirit or scope of the following claims.

INCORPORATION BY REFERENCE

The entire contents of all patents, published patent applications, and other references cited herein are hereby expressly incorporated herein in their entireties by reference.

CLAIMS

What is claimed is:

1. A device for generating an asymmetric double well system comprising:

an oscillator;

a parametric drive arranged and disposed to bifurcate the oscillator, creating a static effective double well; and

an additive drive arranged and disposed to create an asymmetry between the wells.

2. The device of claim 1, wherein the oscillator is non-linear.

3. The device of claim 1, wherein the oscillator is a transmon oscillator.

4. The device of claim 3, wherein the transmon oscillator comprises two superconducting nonlinear asymmetric inductive elements (SNAILs) shunted by a capacitor.

5. The device of claim 1, wherein an asymmetry of the wells is controlled by ϵ_1.

6. The device of claim 5, wherein $|\epsilon_1| = \frac{\Omega_1}{2}$;

where:

Ω_1 is the amplitude of the additive drive.

7. The device of claim 1, wherein a depth of the wells is controlled by ϵ_2.

8. The device of claim 7, wherein $\epsilon_2 = g_3 \frac{4\Omega_2}{3\omega_a}$;

where:

g_3 is the third-order non-linearity of the circuit;

Ω_2 is the amplitude of the parametric drive;

ω_a is the renormalized oscillator resonance frequency, which is Lamb- and Stark-shifted from ω_0; and

ω_0 is the bare resonance frequency of the oscillator.

9. The device of claim 1, wherein the additive drive, the parametric drive, and the oscillator

together form a continuously tunable asymmetric Kerr parametric oscillator.

10. A method of generating a double well system, the method comprising:

providing the device according to any one of claims 1-9;

driving the oscillator with the parametric drive, the parametric drive bifurcating the oscillator and creating an effective double well; and

driving the oscillator with an additive drive, the additive drive creating an asymmetry between the wells.

11. The method of claim 10, wherein a barrier height of the asymmetric double well is continuously tunable.

12. The method of claim 11, wherein tuning the barrier height comprises adjusting ϵ_2 according to the equation $\epsilon_2 = g_3 \frac{4\Omega_2}{3\omega_a}$;

where:

g_3 is the third-order non-linearity of the circuit;

Ω_2 is the amplitude of the parametric drive;

ω_a is the renormalized oscillator resonance frequency, which is Lamb- and Stark-shifted from ω_0; and

ω_0 is the bare resonance frequency of the oscillator.

13. The method of claim 10, wherein the asymmetry of the asymmetric double well is continuously tunable.

14. The method of claim 13, wherein tuning the asymmetry comprises adjusting ϵ_1 according to the equation $|\epsilon_1| = \frac{\Omega_1}{2}$;

where:

Ω_1 is the amplitude of the additive drive.

15. The method of claim 10, wherein an activation of the system exhibits pronounced quantum resonances whole width alternates with both the depth and the asymmetry of the wells.

16. The method of claim 10, wherein the asymmetric double well experiences an increased

activation time from one well to the other as compared to a symmetric double well.

17. The method of claim 16, wherein the asymmetric double well experiences the increased activation time when the system is initialized in a shallower well.

18. The method of claim 10, wherein the driven double well system simulates a static system.

19. The method of claim 10, wherein the oscillator is non-linear and driven in the quantum regime.

20. The method of claim 10, further comprising modeling the dynamics of a chemical reaction with the asymmetric double-well.

21. The method of claim 20, wherein the double-well comprises a Hamiltonian according to the equation:

$$\hat{H}_{DW} = \frac{\hat{p}^2}{2m} + k_4\hat{x}^4 - k_2\hat{x}^2 + k_1\hat{x}$$

where:

$\hat{x}$ is a position operator associated with motion along a reaction coordinate;

$\hat{p}$ is a momentum operator associated with motion along the reaction coordinate;

m is the mass associated with the motion along the reaction coordinate; and

$\{k_1, k_2, k_4\}$ are positive and real parameters whose values define the double well free energy profile; and

wherein $\hat{x}$ and $\hat{p}$ satisfy the equation $[\hat{x}, \hat{p}] = i\hbar$.

22. The method of claim 21, further comprising fitting the Hamiltonian to a fourth-order polynomial according to the equation:

$$V(x) = k_4x^4 - k_2x^2 + k_1x$$

where:

$k_4x^4 - k_2x^2$ relates to obtaining the double-well feature; and

k_1x accounts for asymmetry between reactant and product wells.

23. The method of claim 21, further comprising mapping a Hamiltonian of a Kerr-Cat device onto the double-well Hamiltonian, the Kerr-Cat device Hamiltonian having the equation:

$$\hat{H}_{KC} = \Delta\hat{a}^\dagger\hat{a} - K(\hat{a}^\dagger)^2(\hat{a})^2 + \epsilon_2(\hat{a}^2 + \hat{a}^{\dagger 2}) + \epsilon_1(\hat{a} + \hat{a}^\dagger)$$

where:

$\hat{a}^\dagger$ and $\hat{a}$ are the device's ladder operators, associated with excitations and de-excitations, respectively, between the device's effective energy levels;

K is the Kerr non-linearity;

Δ is the detuning; and

ϵ_1 and ϵ_2 are drive coefficients; and

wherein $\hat{a}^\dagger$ and $\hat{a}$ satisfy the equation $[\hat{a}, \hat{a}^\dagger] = 1$.

24. The method of claim 23, wherein the mapping of the Kerr-Cat device Hamiltonian onto the double-well Hamiltonian comprises:

mapping photonic operators $\{\hat{a}, \hat{a}^\dagger\}$ onto operators associated with motion along a reaction coordinate $\{\hat{x}, \hat{p}\}$ according to the equations:

$$\hat{a} = \frac{1}{\sqrt{2}}\left(\frac{1}{c}\hat{x} + \frac{ic}{\hbar}\hat{p}\right) \; ; \; \hat{a}^\dagger = \frac{1}{\sqrt{2}}\left(\frac{1}{c}\hat{x} - \frac{ic}{\hbar}\hat{p}\right)$$

$$\hat{x} = \frac{c}{\sqrt{2}}(\hat{a} + \hat{a}^\dagger) \; ; \; \hat{p} = \frac{\hbar}{i\sqrt{2}c}(\hat{a} - \hat{a}^\dagger);$$

where:

c is a constant parameter that has units of length.

25. The method of claim 24, further comprising recasting a negative of the Kerr-Cat Hamiltonian in terms of the $\hat{x}$ and $\hat{p}$ according to the following equation:

$$-\hat{H}_{KC} = \frac{c^2}{\hbar^2}(\epsilon_2 - K - \Delta/2)\hat{p}^2 + \frac{K}{4c^4}\hat{x}^4 - \frac{1}{c^2}(\epsilon_2 + K + \Delta/2)\hat{x}^2 - \frac{\epsilon_1\sqrt{2}}{c}\hat{x} + \frac{Kc^4}{4\hbar^4}\hat{p}^4 + \frac{K}{4\hbar^2}\hat{x}^2\hat{p}^2 + \frac{K}{4\hbar^2}\hat{p}^2\hat{x}^2$$

where:

$\hat{a}^\dagger$ and $\hat{a}$ are the device's ladder operators, associated with excitations and de-excitations, respectively, between the device's effective energy levels;

K is the Kerr non-linearity;

Δ is the detuning; and

ϵ_1 and ϵ_2 are drive coefficients; and

wherein $\hat{a}^\dagger$ and $\hat{a}$ satisfy the equation $[\hat{a}, \hat{a}^\dagger] = 1$.

26. The method of claim 25, further comprising mapping $\{\Delta, K, \epsilon_1, \epsilon_2\}$ onto $\{m, k_1, k_2, k_4\}$ using the following mapping relations:

$$K = 4c^4k_4;$$

$$\epsilon_2 = \frac{\hbar^2+2c^4k_2m}{4c^2m};$$

$$\Delta = \frac{2c^4k_2m-\hbar^2-16c^6k_4m}{2c^2m}; \text{ and}$$

$$\epsilon_1 = \frac{ck_1}{\sqrt{2}}.$$

27. The method of claim 26, where c is selected to satisfy the following inequality:

$$\frac{\hbar^2}{mk_2c^4} \gg 1.$$

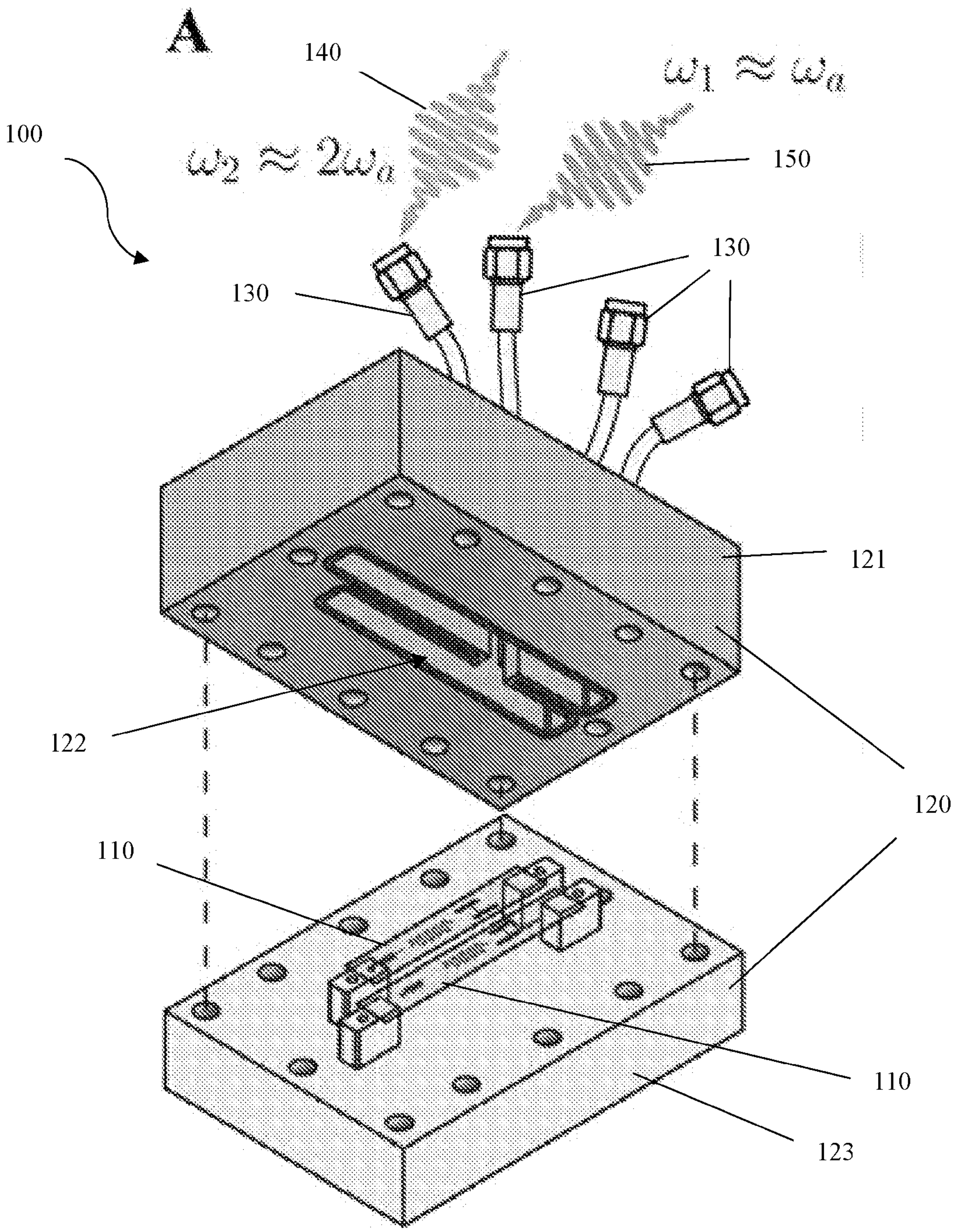
A
140
$\omega_1 \approx \omega_a$
100
$\omega_2 \approx 2\omega_a$
150
130
130
121
122
120
110
110
123

FIG. 1A

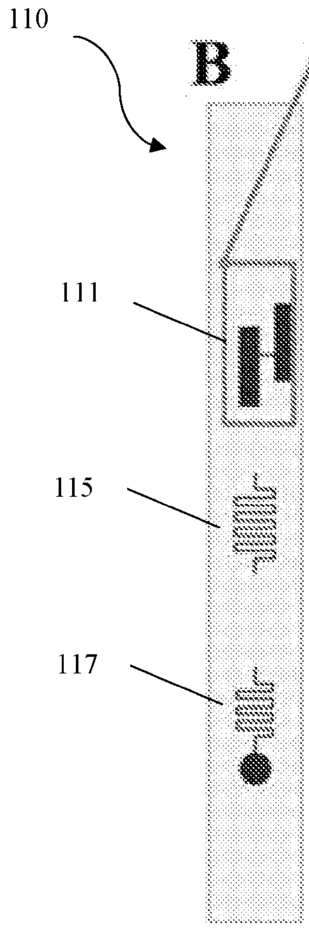

FIG. 1B

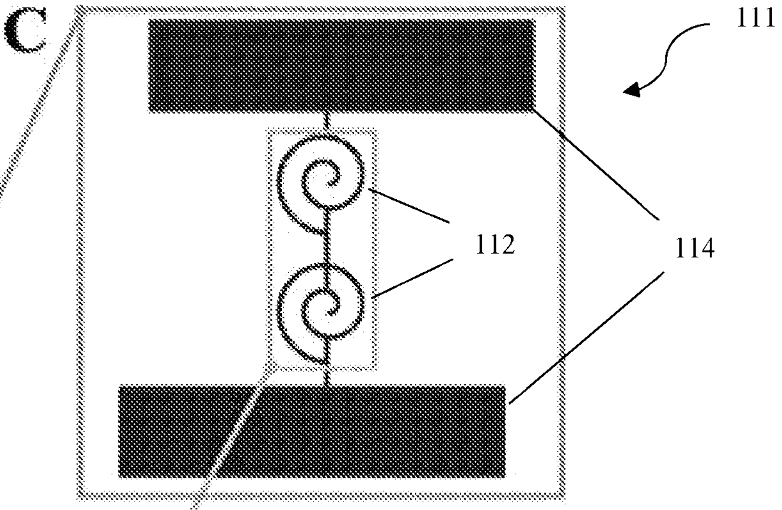

FIG. 1C

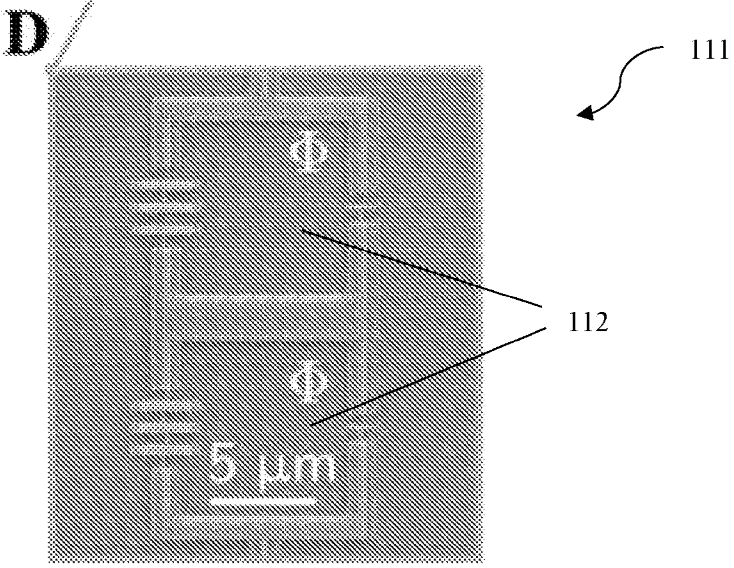

FIG. 1D

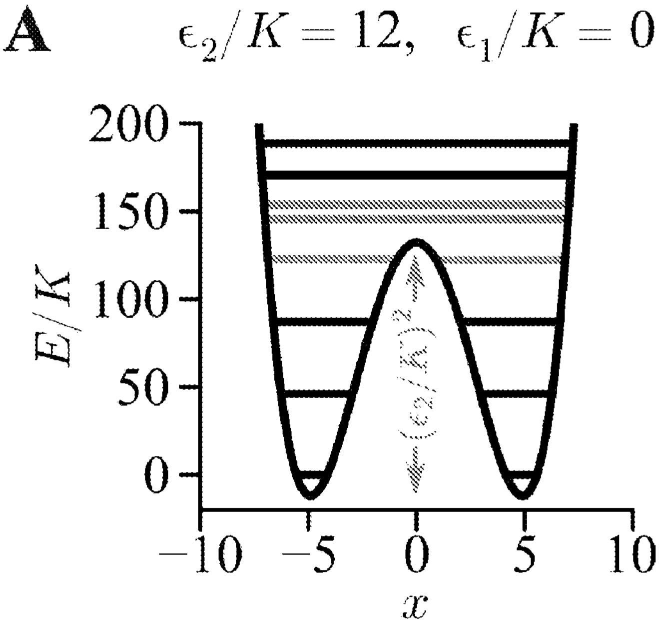
A
$\epsilon_2/K = 12, \quad \epsilon_1/K = 0$
200
150
100
50
0
E/K
$(\epsilon_2/K)^2$
−10
−5
0
5
10
x

FIG. 2A

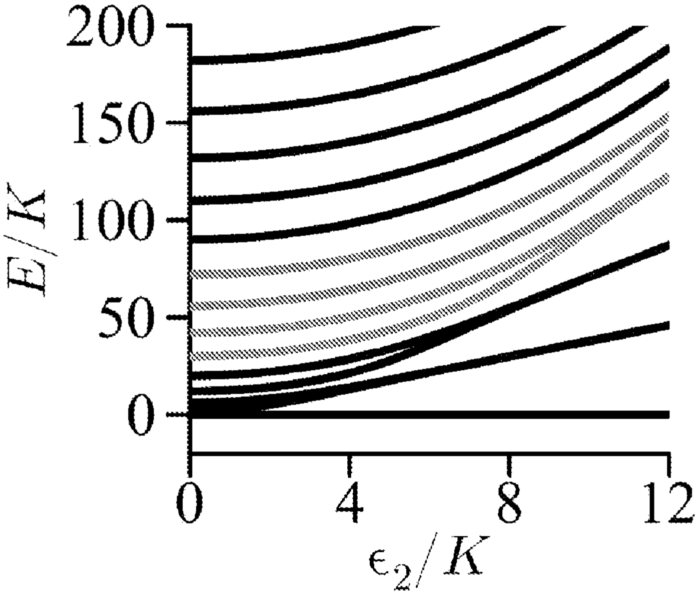
200
150
100
50
0
E/K
0
4
8
12
ϵ_2/K

FIG. 2B

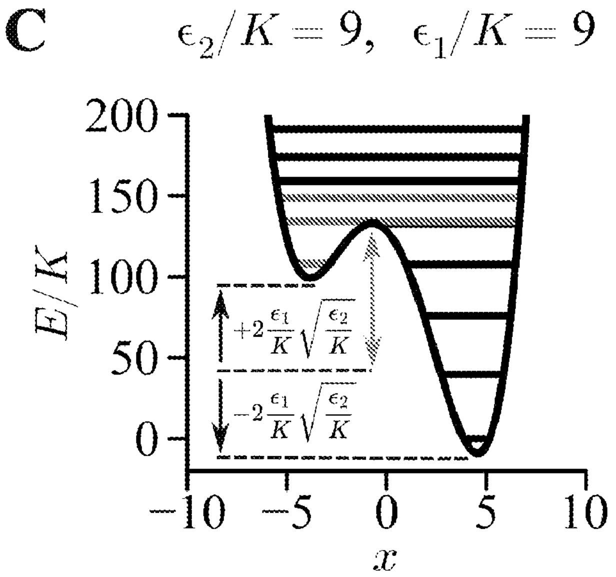
C
$\epsilon_2/K = 9,\ \ \epsilon_1/K = 9$
200
150
100
50
0
E/K
$+2\frac{\epsilon_1}{K}\sqrt{\frac{\epsilon_2}{K}}$
$-2\frac{\epsilon_1}{K}\sqrt{\frac{\epsilon_2}{K}}$
−10
−5
0
5
10
x

FIG. 2C

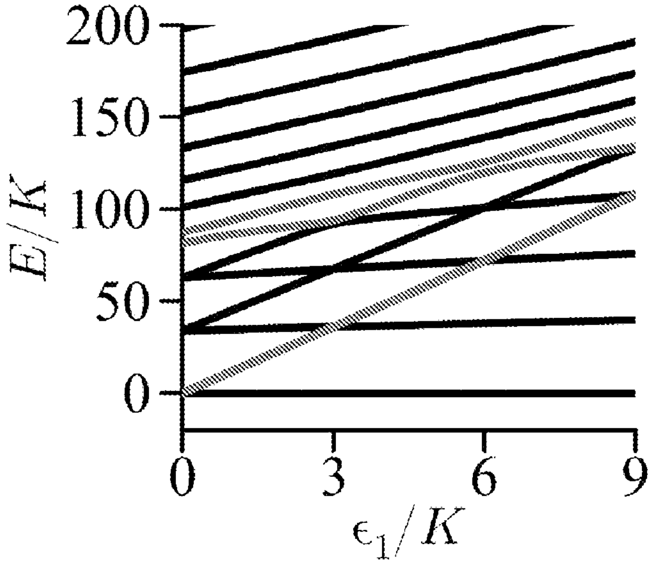
200
150
100
50
0
E/K
0
3
6
9
ϵ_1/K

FIG. 2D

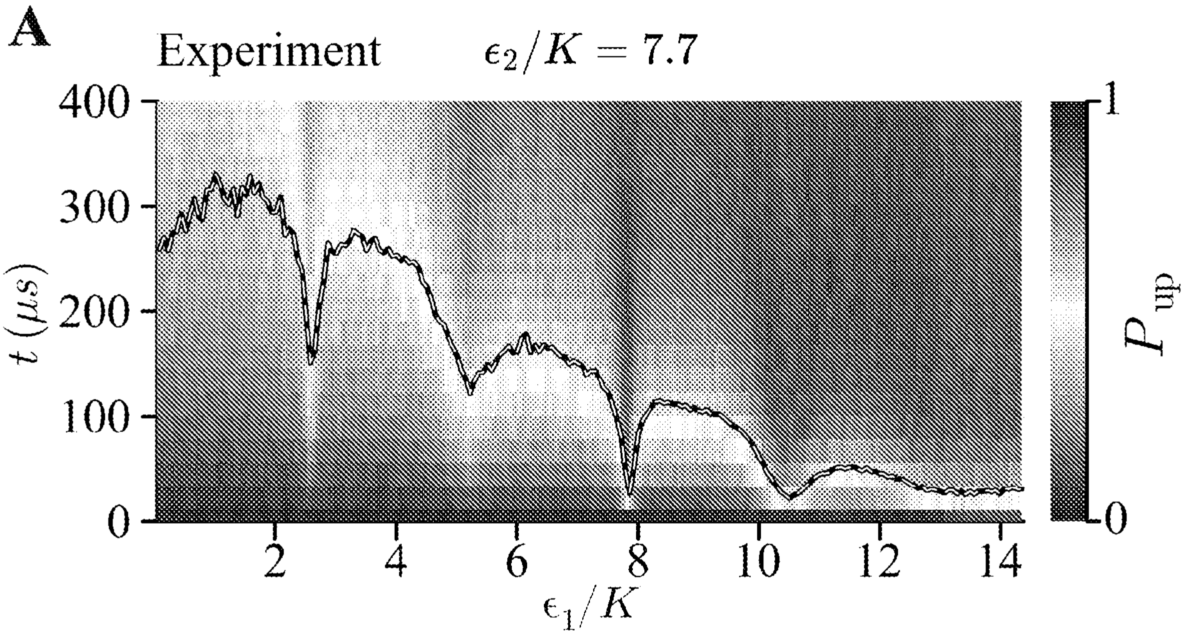
A
Experiment
$\epsilon_2/K = 7.7$
400
300
200
100
0
$t\,(\mu s)$
2
4
6
8
10
12
14
ϵ_1/K
1
0
P_{up}

FIG. 3A

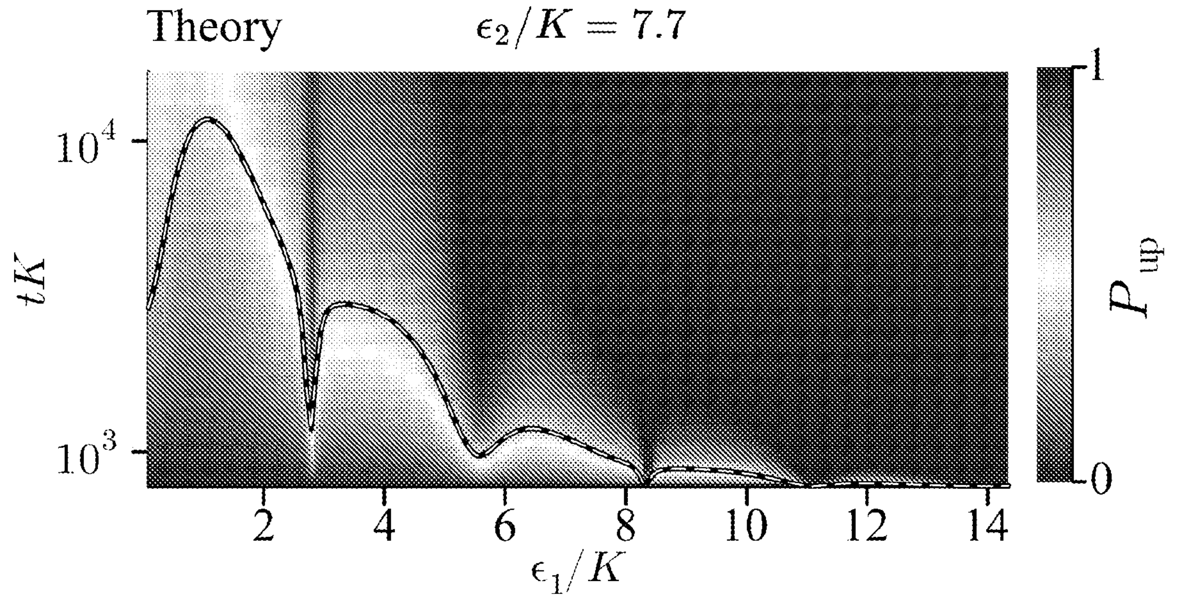
Theory
$\epsilon_2/K = 7.7$
10^4
10^3
tK
2
4
6
8
10
12
14
ϵ_1/K
1
0
P_{up}

FIG. 3B

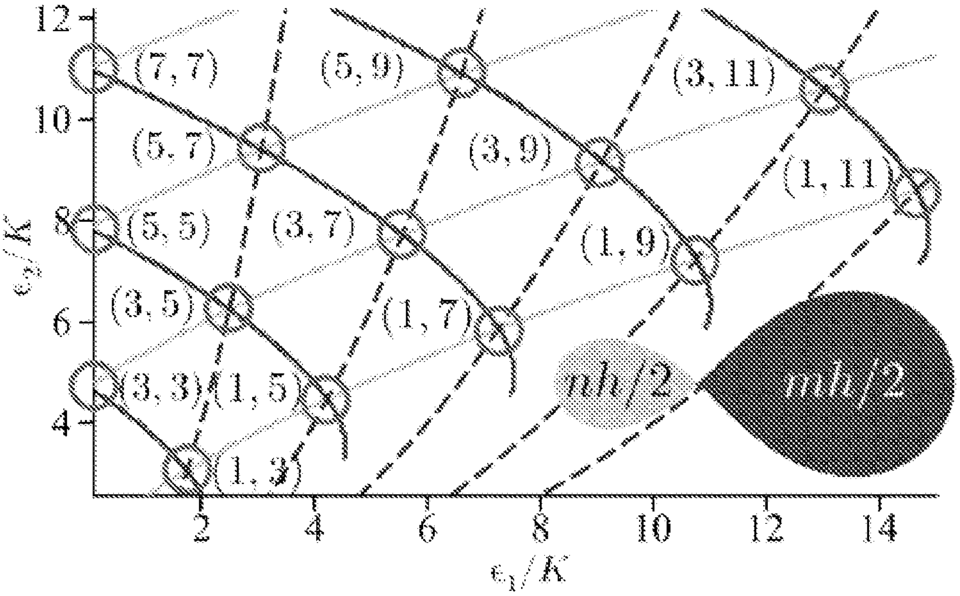
(7, 7)
(5, 9)
(3, 11)
(5, 7)
(3, 9)
(1, 11)
(5, 5)
(3, 7)
(1, 9)
(3, 5)
(1, 7)
(3, 3)
(1, 5)
(1, 3)
nh/2
mh/2
12
10
8
6
4
2
4
6
8
10
12
14
ϵ_2/K
ϵ_1/K

FIG. 4A

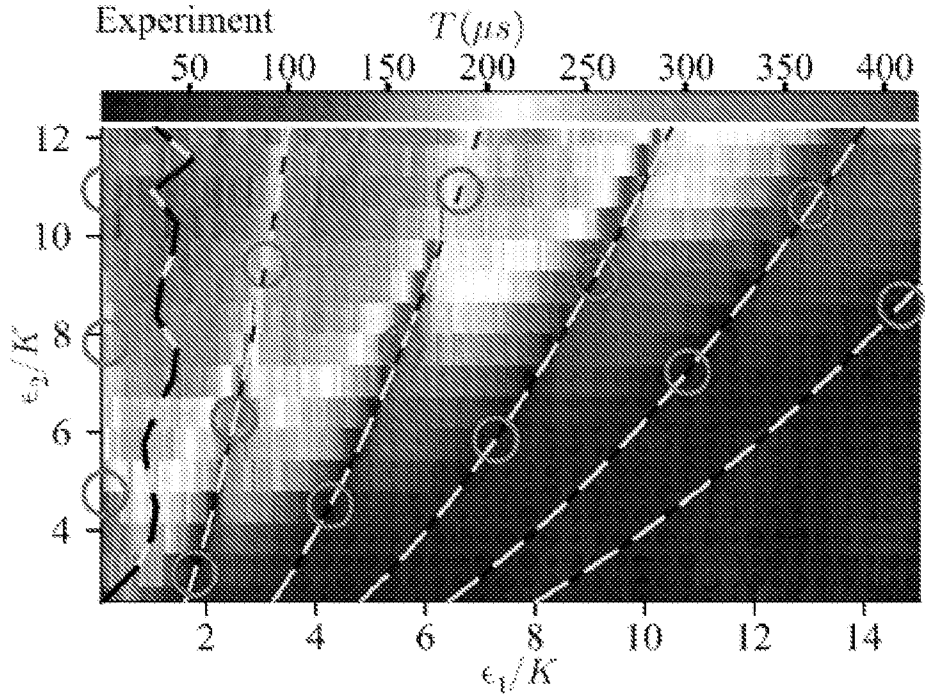
Experiment
$T(\mu s)$
50
100
150
200
250
300
350
400
12
10
8
6
4
2
4
6
8
10
12
14
ϵ_2/K
ϵ_1/K

FIG. 4B

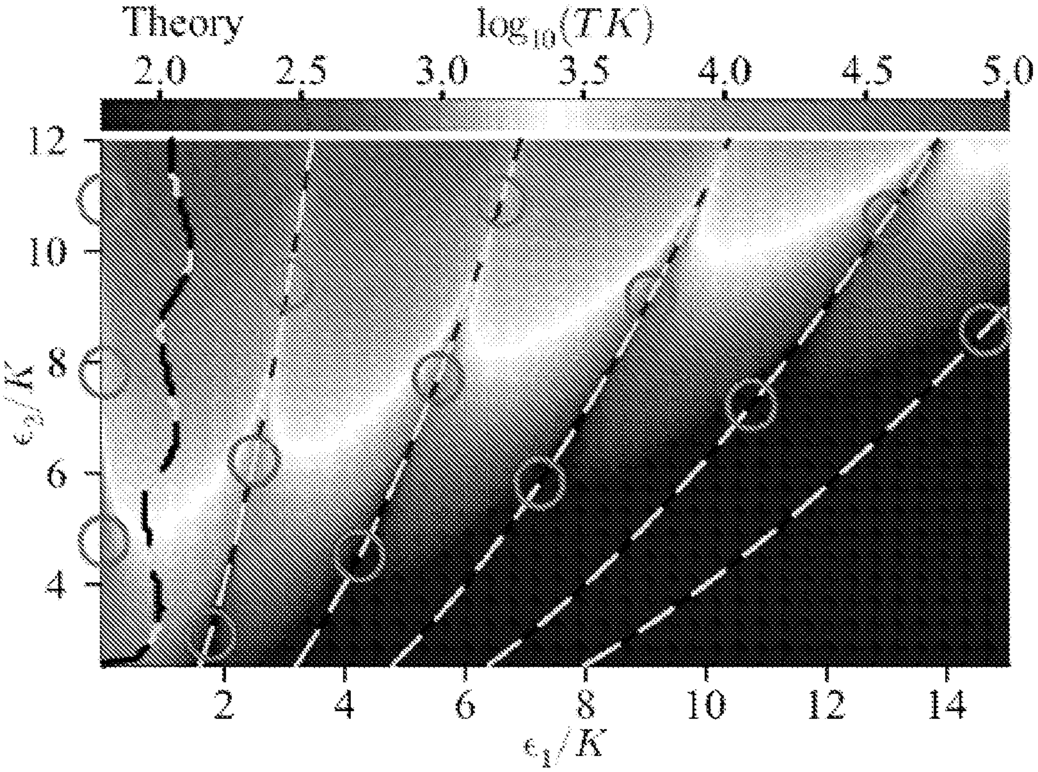
Theory
$\log_{10}(TK)$
2.0
2.5
3.0
3.5
4.0
4.5
5.0
12
10
8
6
4
ϵ_2/K
2
4
6
8
10
12
14
ϵ_1/K

FIG. 4C

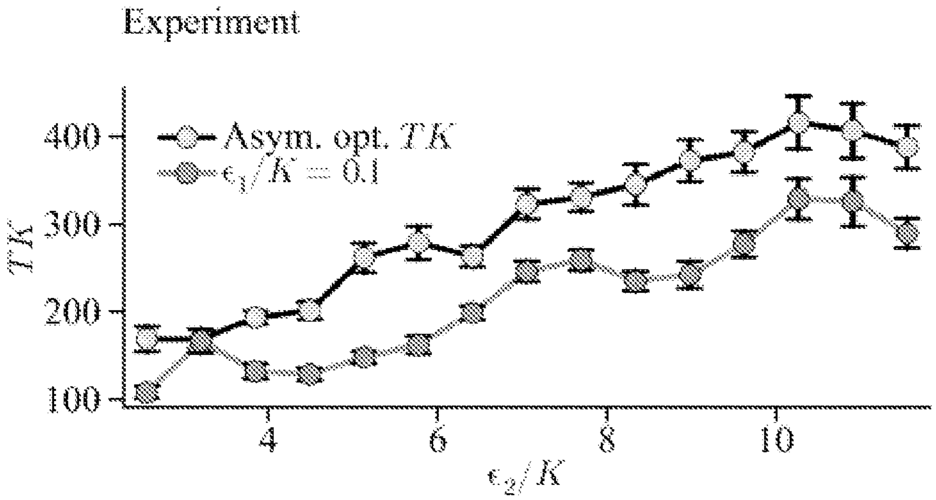
Experiment
Asym. opt. TK
$\epsilon_1/K = 0.1$
TK
100
200
300
400
4
6
8
10
ϵ_2/K

FIG. 5A

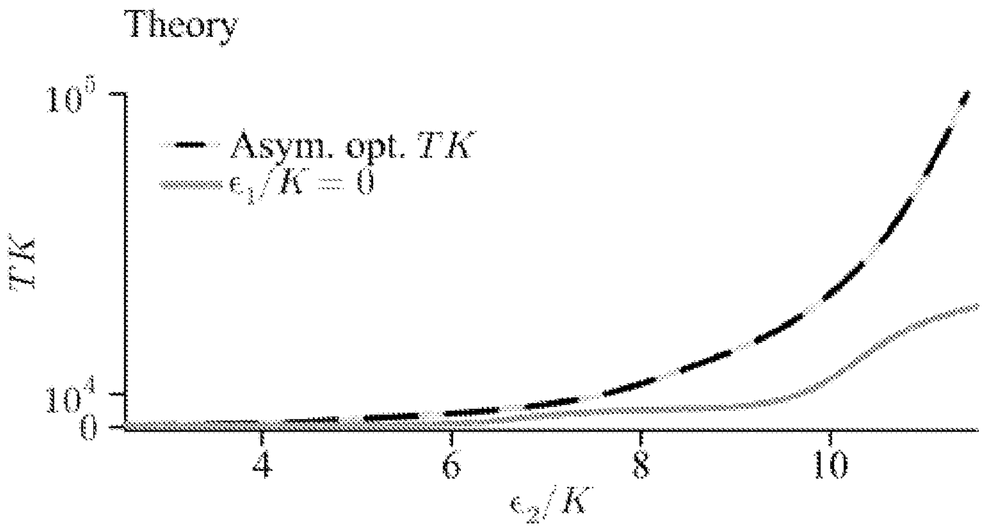
Theory
Asym. opt. TK
$\epsilon_1/K = 0$
TK
10^5
10^4
0
4
6
8
10
ϵ_2/K

FIG. 5B

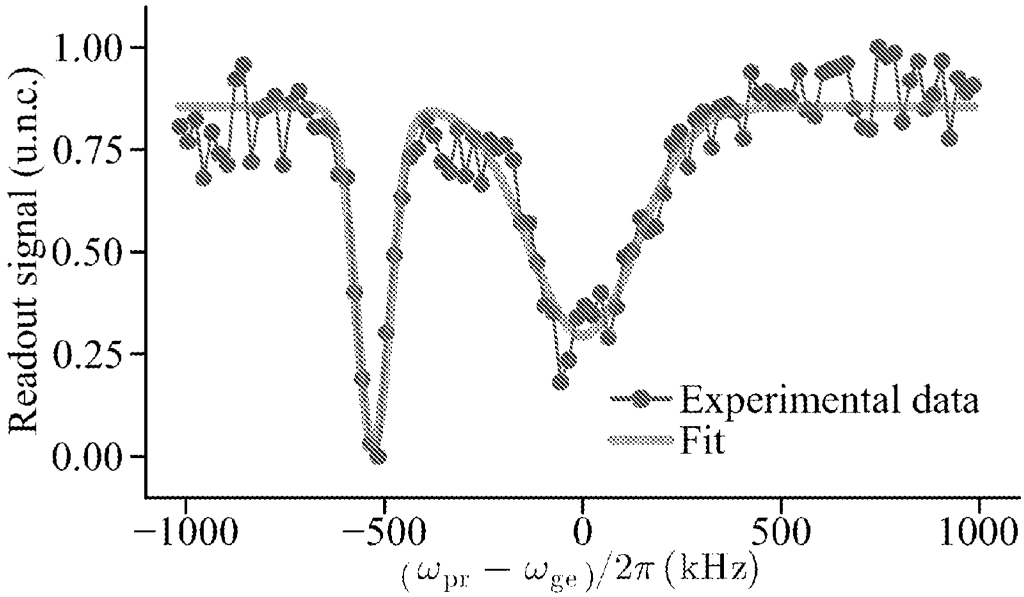
Readout signal (u.n.c.)
1.00
0.75
0.50
0.25
0.00
−1000
−500
0
500
1000
$(\omega_{\mathrm{pr}} - \omega_{\mathrm{ge}})/2\pi$ (kHz)
Experimental data
Fit

FIG. 6

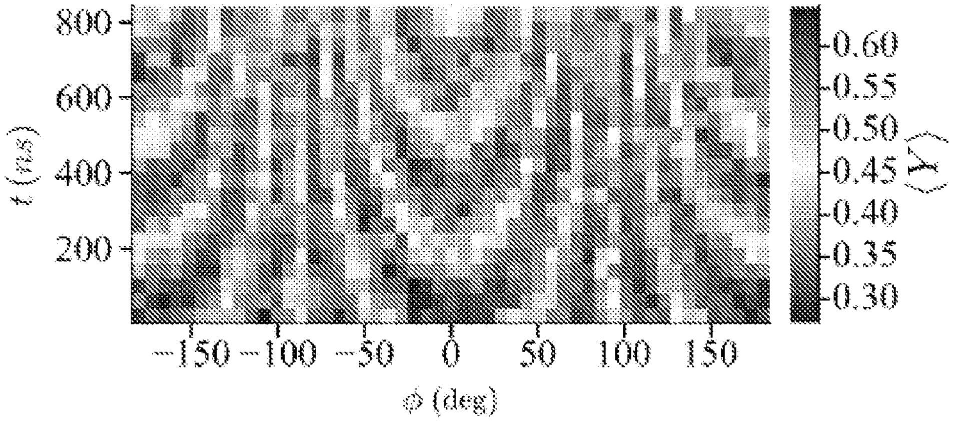

FIG. 7A

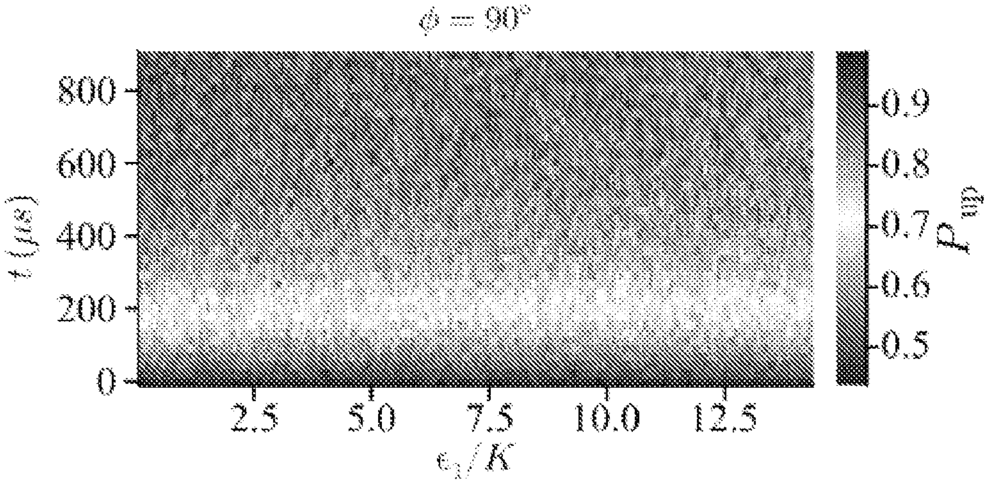

FIG. 7B

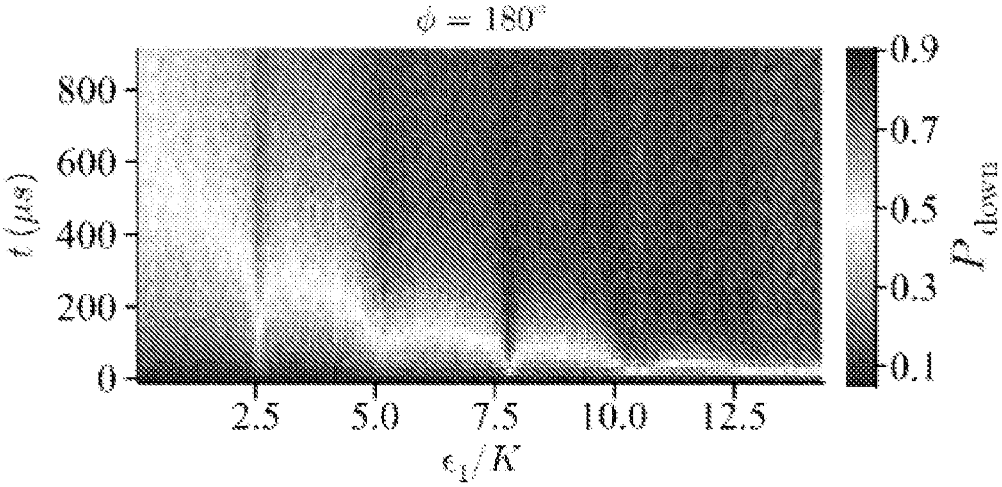

FIG. 7C

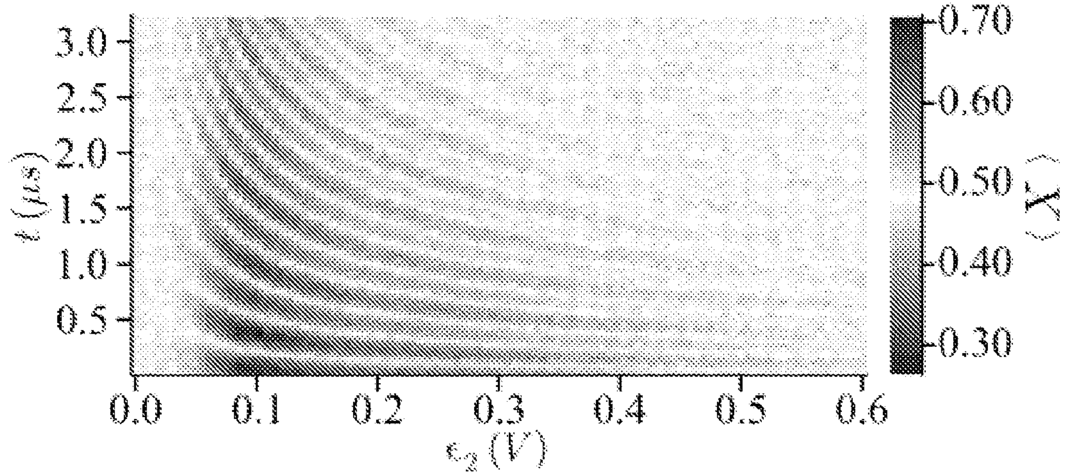
3.0
2.5
2.0
1.5
1.0
0.5
$t\ (\mu s)$
0.0
0.1
0.2
0.3
0.4
0.5
0.6
$\epsilon_2\ (V)$
0.70
0.60
0.50
0.40
0.30
$\langle X \rangle$

FIG. 8A

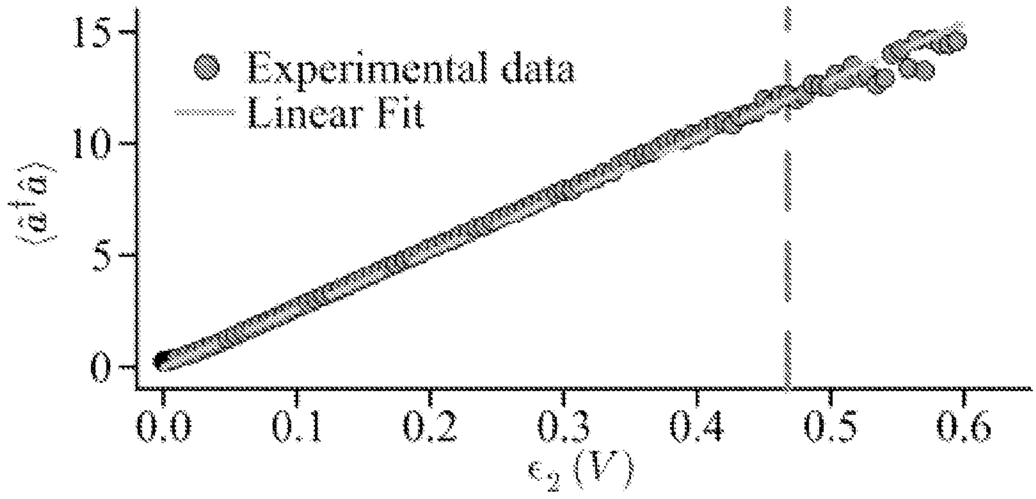
Experimental data
Linear Fit
15
10
5
0
$\langle \hat{a}^\dagger \hat{a} \rangle$
0.0
0.1
0.2
0.3
0.4
0.5
0.6
$\epsilon_2\ (V)$

FIG. 8B

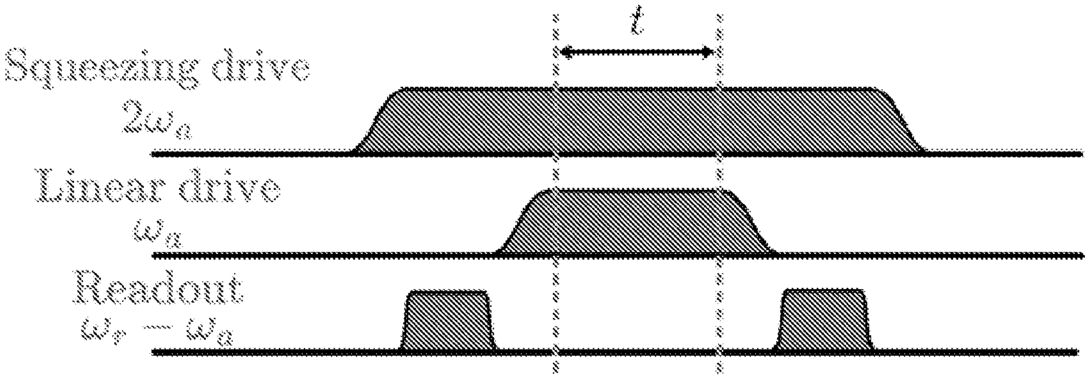
t
Squeezing drive
$2\omega_a$
Linear drive
ω_a
Readout
$\omega_r - \omega_a$

FIG. 9A

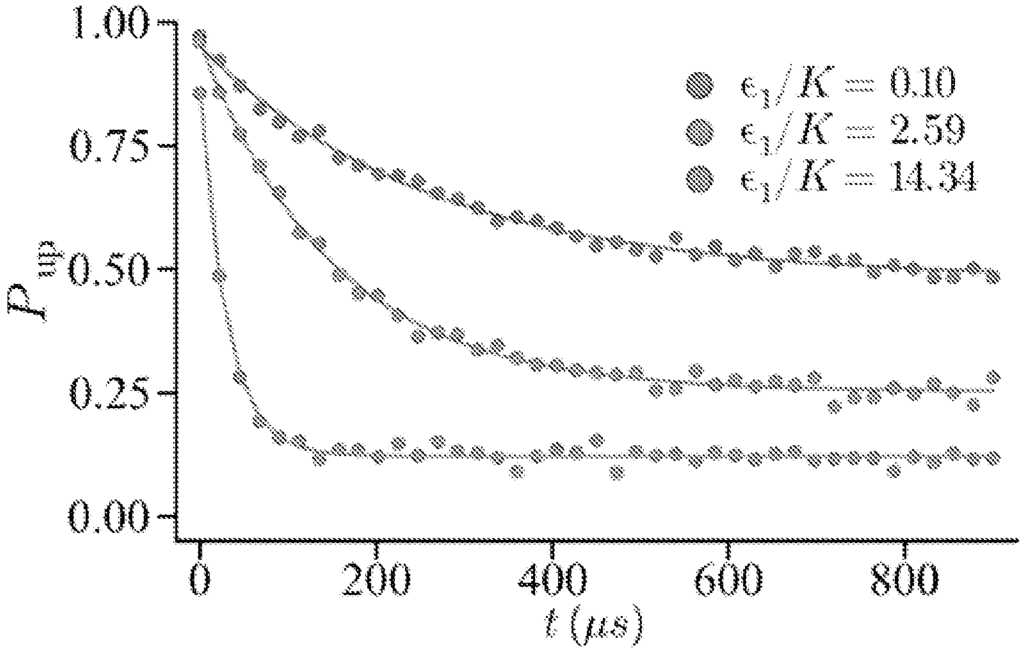
1.00
0.75
0.50
0.25
0.00
P_{up}
0
200
400
600
800
$t\ (\mu s)$
$\epsilon_1/K = 0.10$
$\epsilon_1/K = 2.59$
$\epsilon_1/K = 14.34$

FIG. 9B

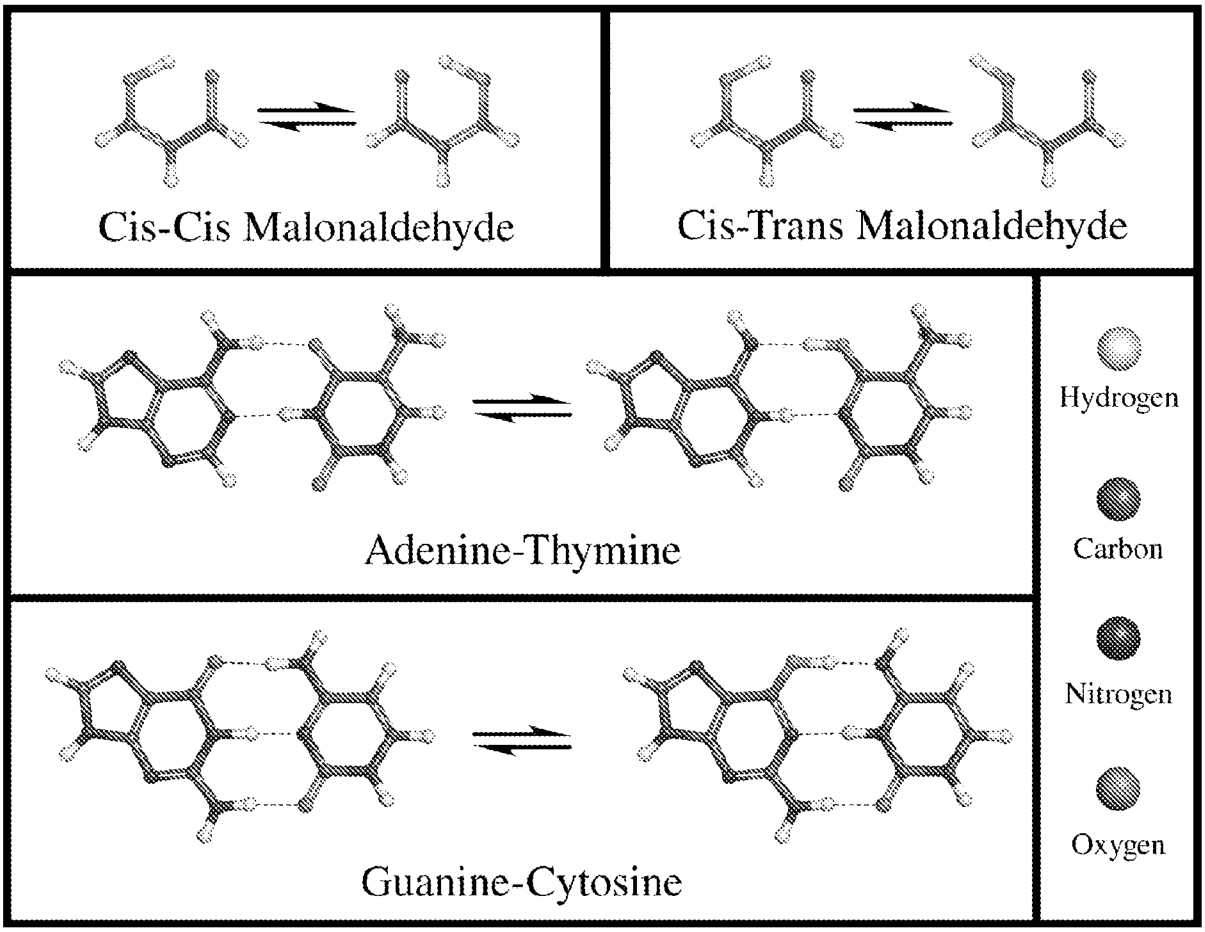
Cis-Cis Malonaldehyde
Cis-Trans Malonaldehyde
Adenine-Thymine
Guanine-Cytosine
Hydrogen
Carbon
Nitrogen
Oxygen

FIG. 10

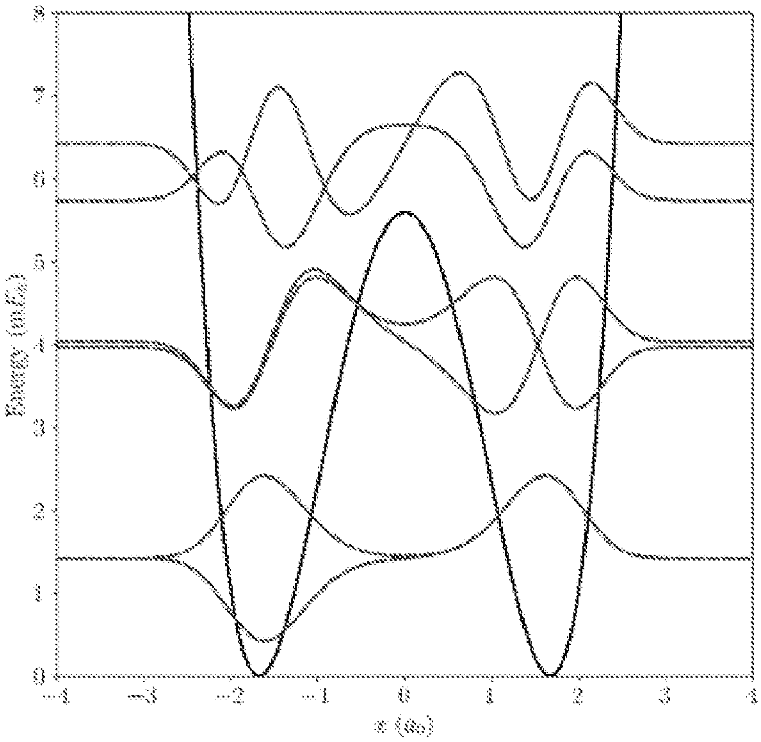

FIG. 11A

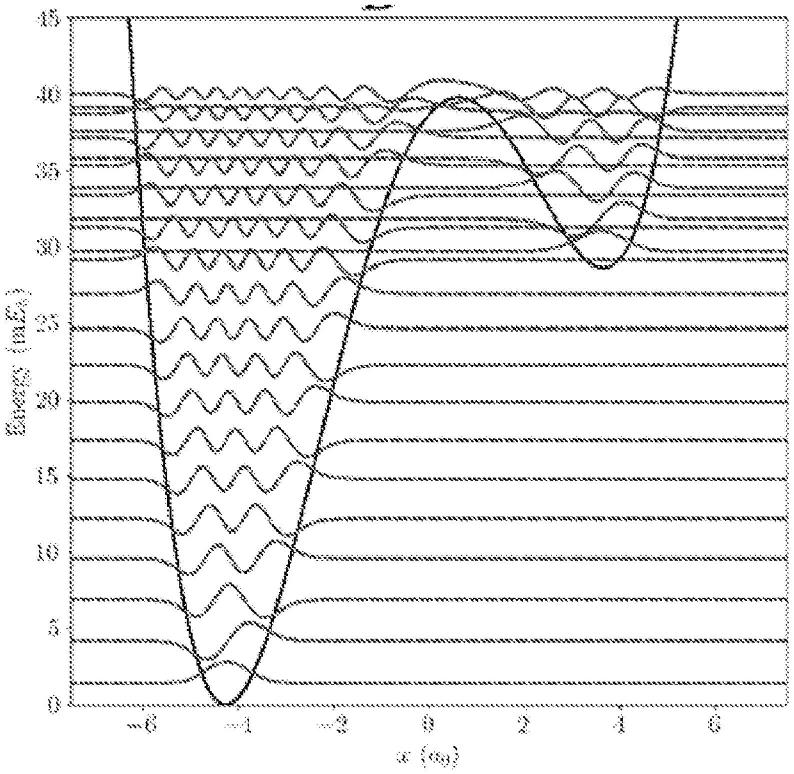

FIG. 11B

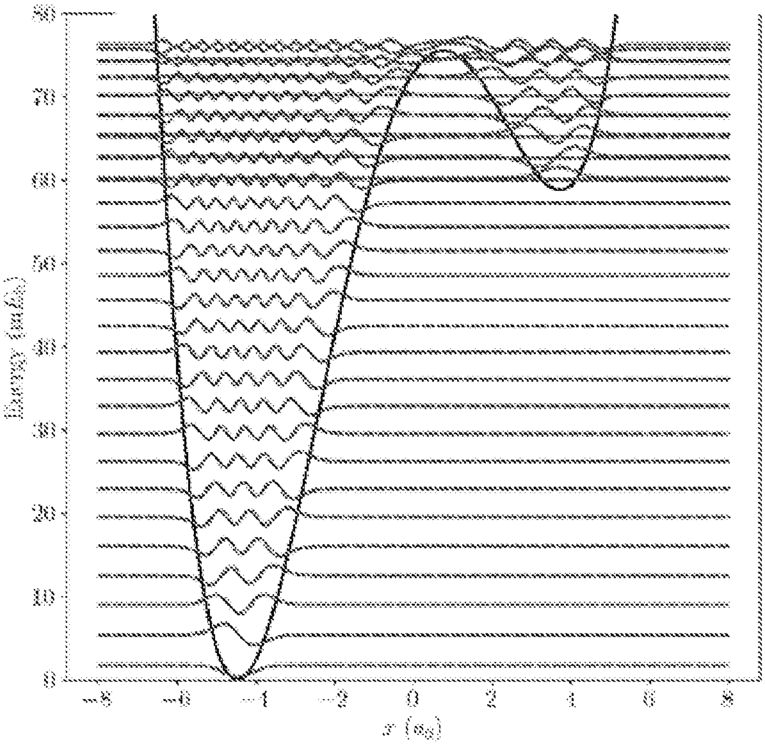

FIG. 11C

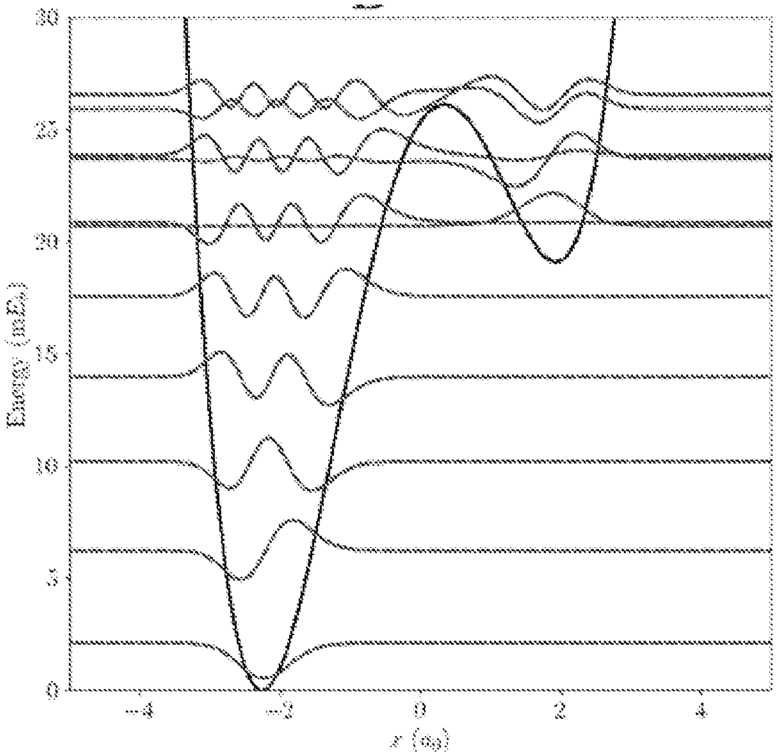

FIG. 11D

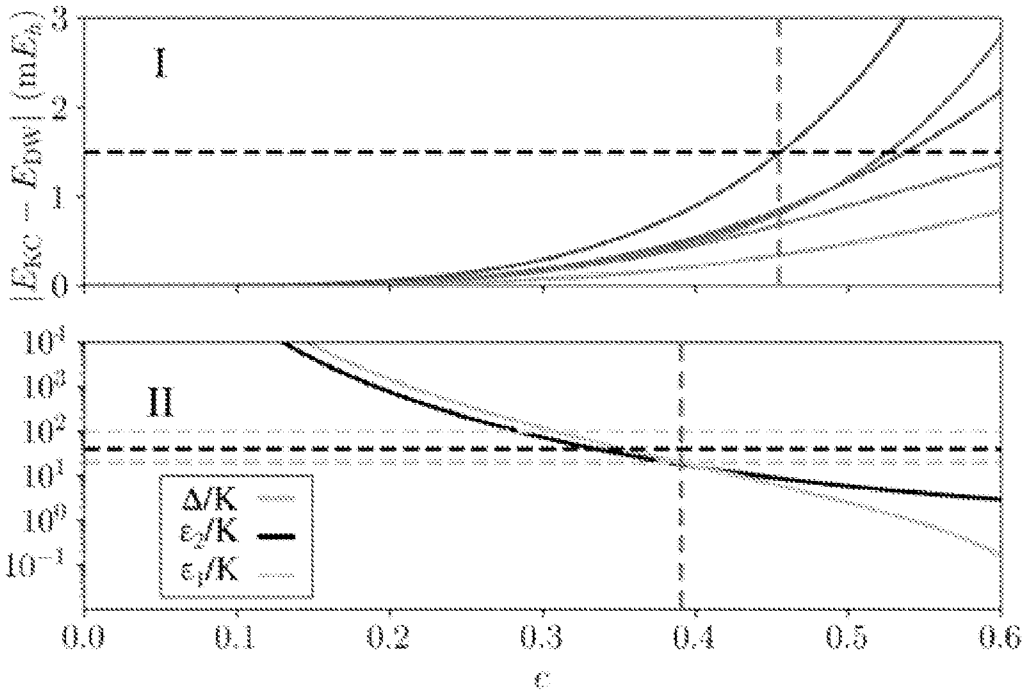

FIG. 12A

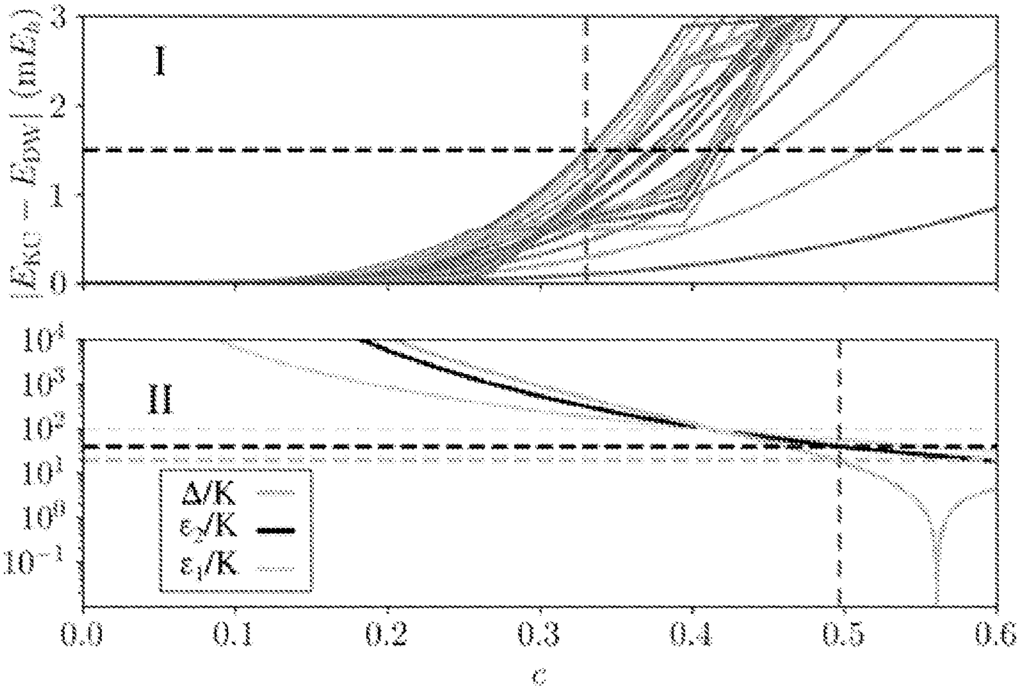

FIG. 12B

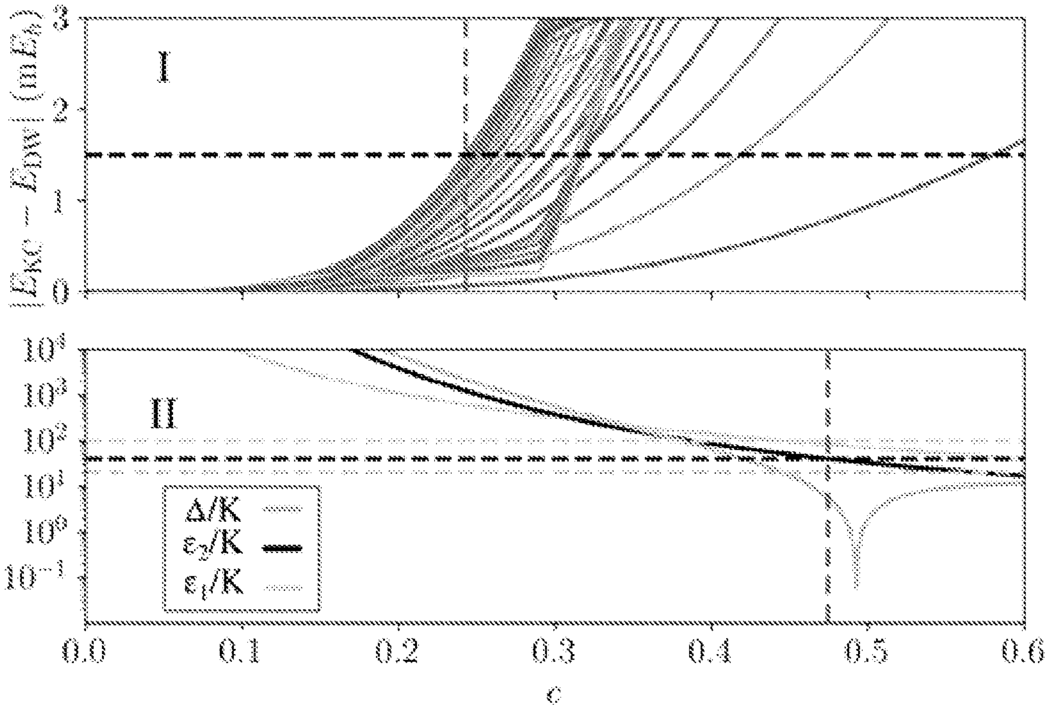

FIG. 12C

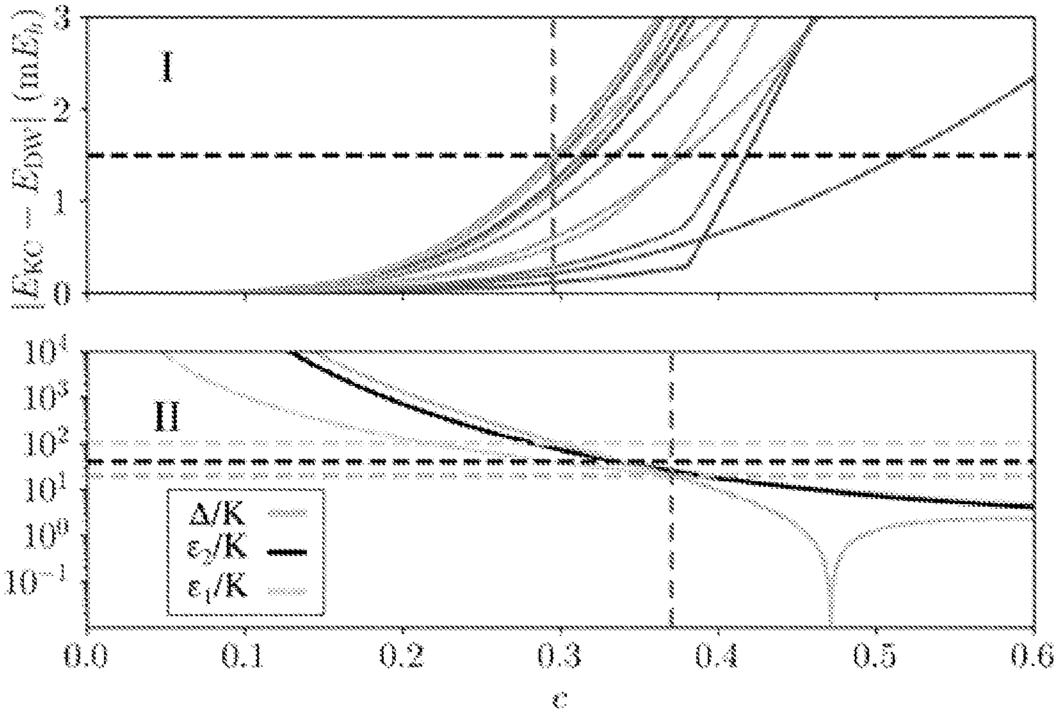

FIG. 12D

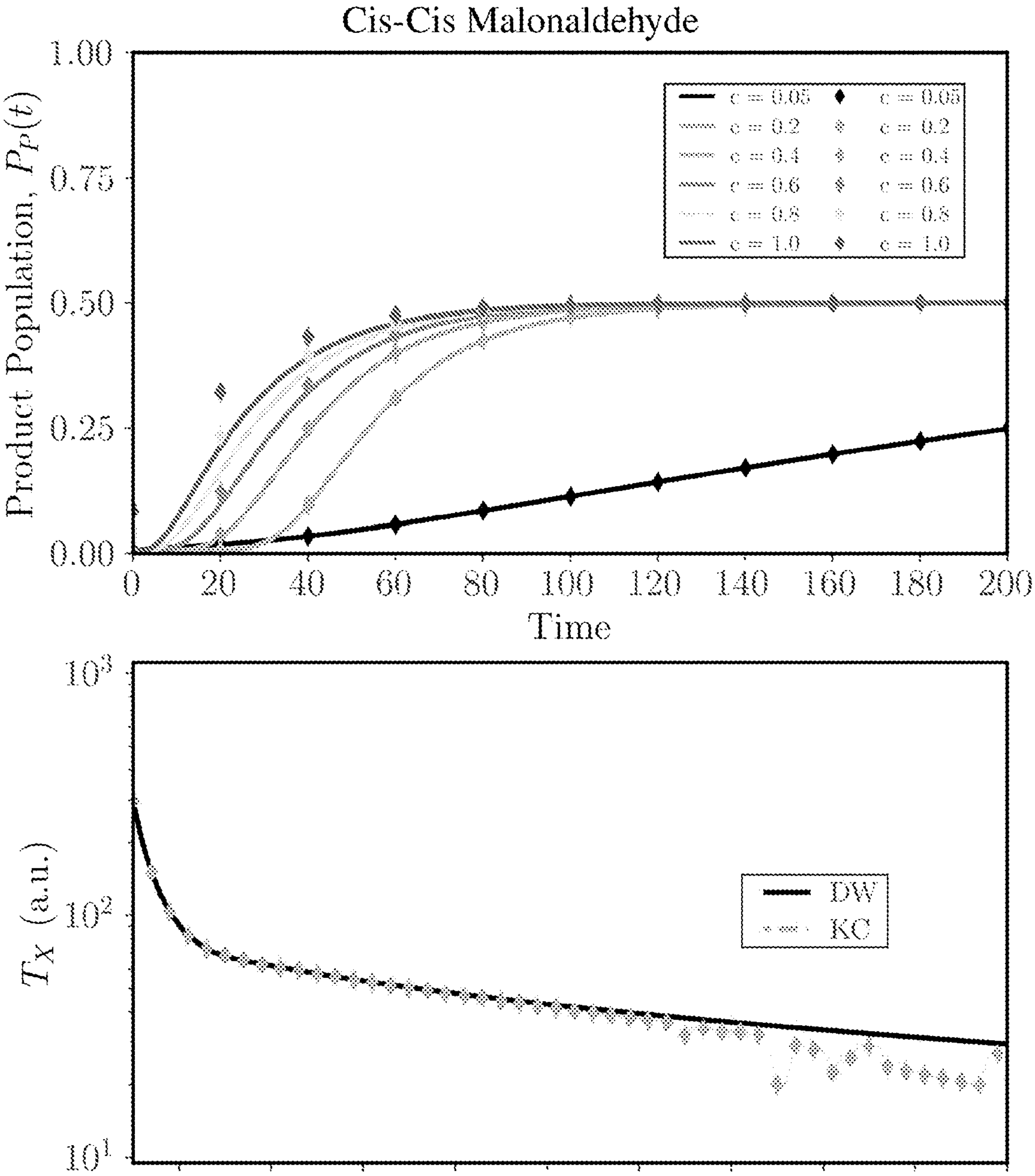
Cis-Cis Malonaldehyde
Product Population, $P_P(t)$
1.00
0.75
0.50
0.25
0.00
c = 0.05
c = 0.2
c = 0.4
c = 0.6
c = 0.8
c = 1.0
c = 0.05
c = 0.2
c = 0.4
c = 0.6
c = 0.8
c = 1.0
0
20
40
60
80
100
120
140
160
180
200
Time
T_X (a.u.)
10^3
10^2
10^1
DW
KC
0.1
0.2
0.3
0.4
0.5
0.6
0.7
0.8
0.9
1.0
c

FIG. 13A

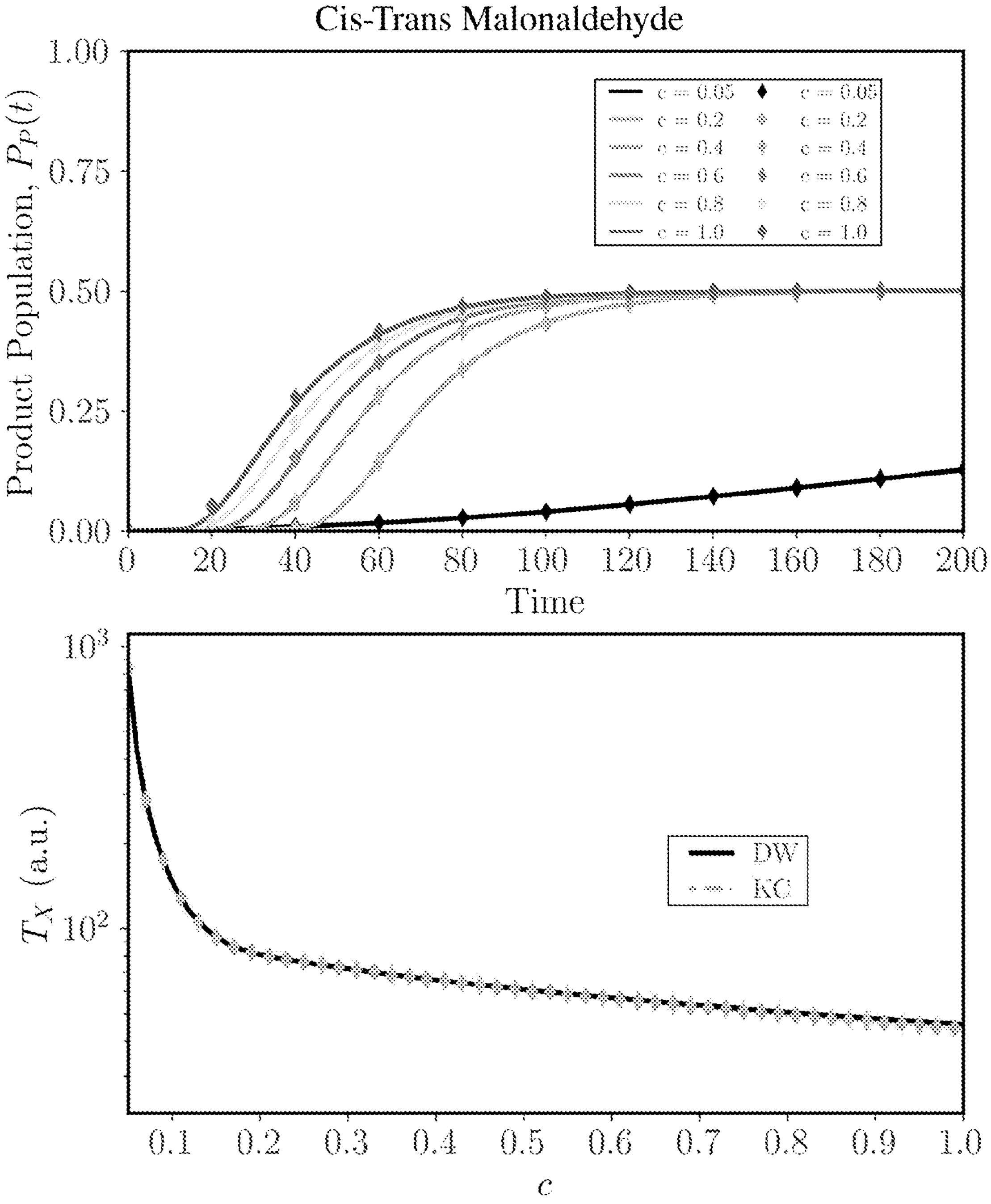
Cis-Trans Malonaldehyde
Product Population, $P_P(t)$
1.00
0.75
0.50
0.25
0.00
c = 0.05
c = 0.2
c = 0.4
c = 0.6
c = 0.8
c = 1.0
c = 0.05
c = 0.2
c = 0.4
c = 0.6
c = 0.8
c = 1.0
0
20
40
60
80
100
120
140
160
180
200
Time
T_X (a.u.)
10^3
10^2
DW
KC
0.1
0.2
0.3
0.4
0.5
0.6
0.7
0.8
0.9
1.0
c

FIG. 13B

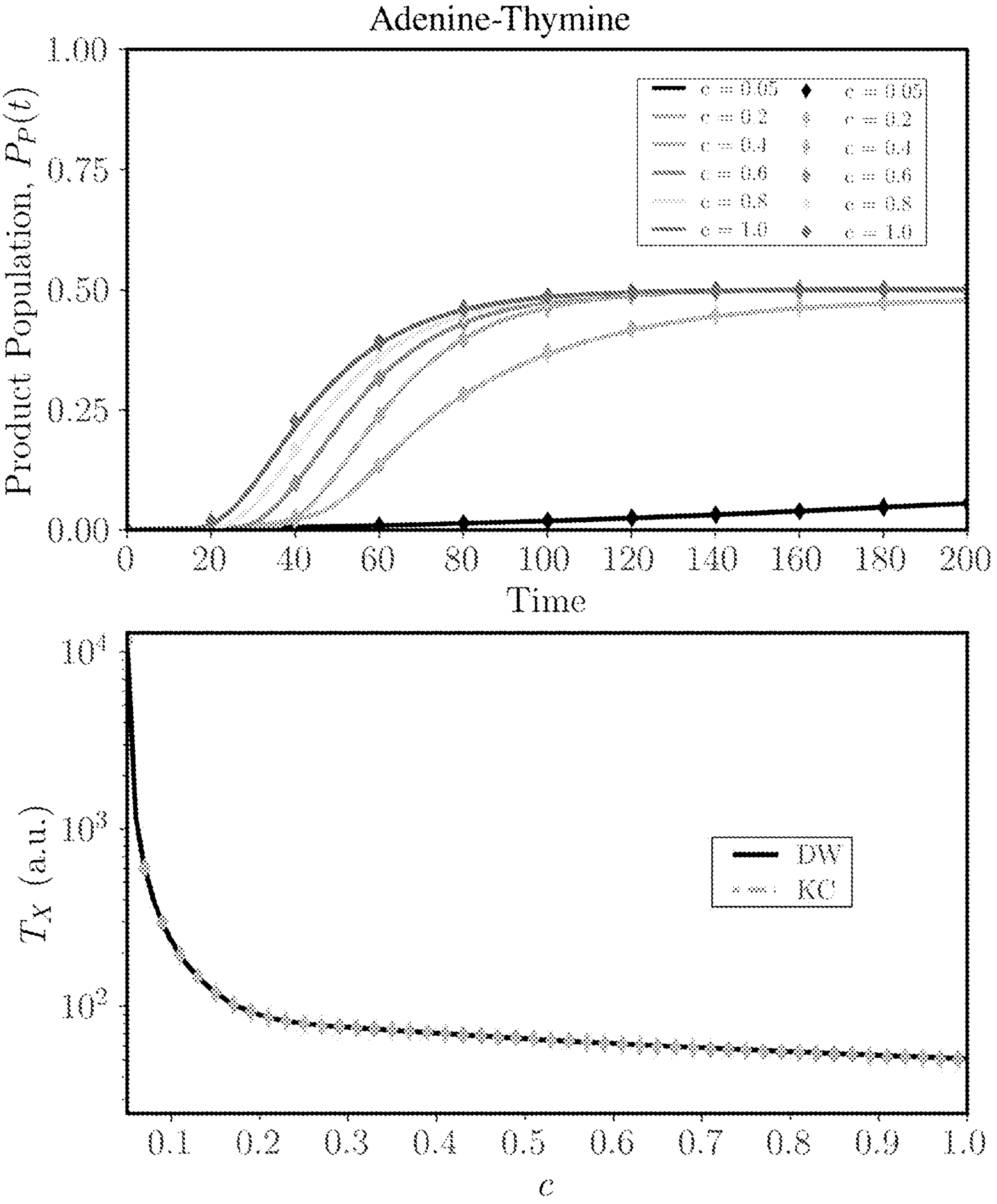
Adenine-Thymine
Product Population, $P_P(t)$
1.00
0.75
0.50
0.25
0.00
0
20
40
60
80
100
120
140
160
180
200
Time
c = 0.05
c = 0.2
c = 0.4
c = 0.6
c = 0.8
c = 1.0
c = 0.05
c = 0.2
c = 0.4
c = 0.6
c = 0.8
c = 1.0
T_X (a.u.)
10^4
10^3
10^2
0.1
0.2
0.3
0.4
0.5
0.6
0.7
0.8
0.9
1.0
c
DW
KC

FIG. 13C

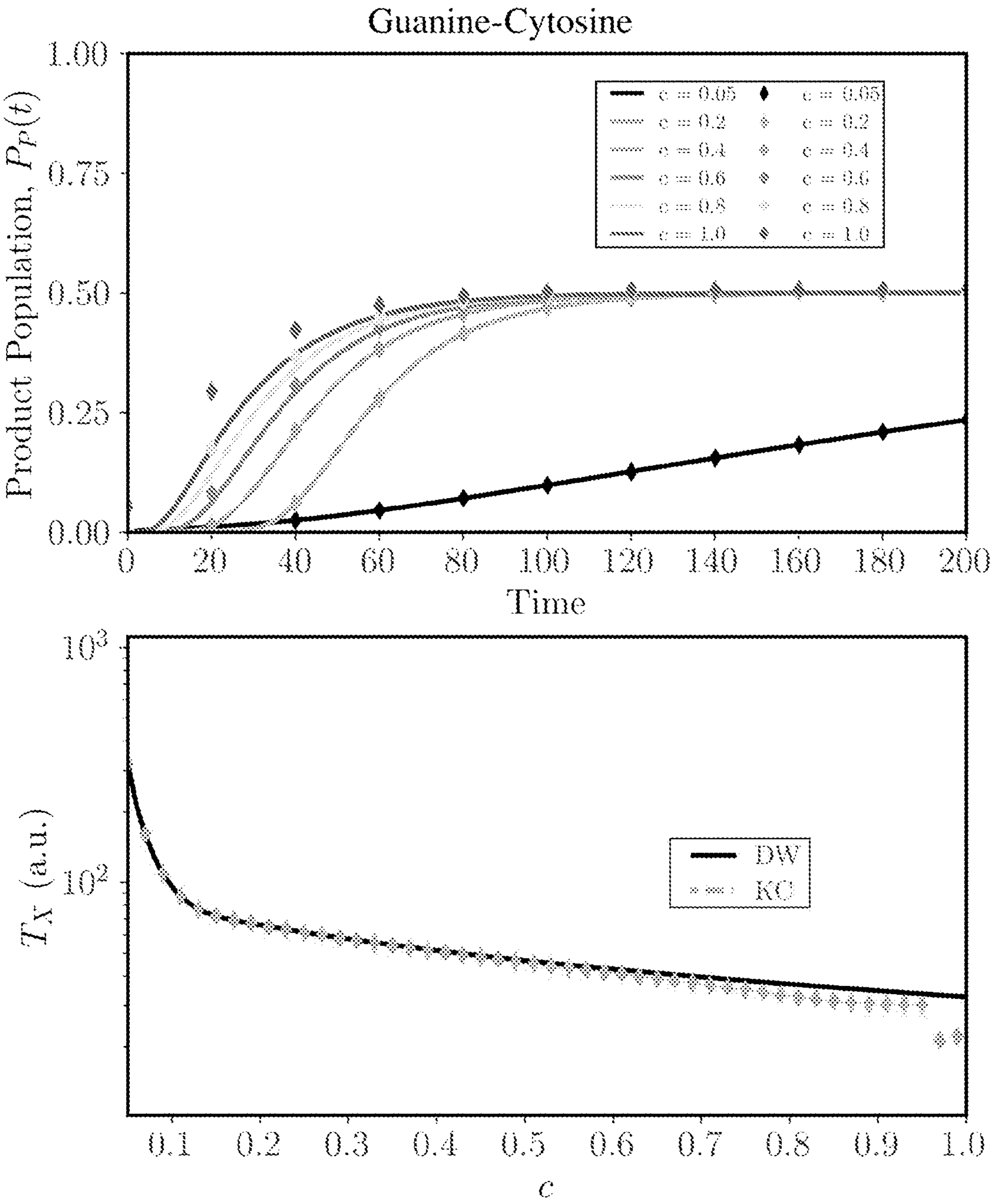
Guanine-Cytosine
Product Population, $P_P(t)$
1.00
0.75
0.50
0.25
0.00
c = 0.05
c = 0.2
c = 0.4
c = 0.6
c = 0.8
c = 1.0
c = 0.05
c = 0.2
c = 0.4
c = 0.6
c = 0.8
c = 1.0
0
20
40
60
80
100
120
140
160
180
200
Time
10^3
10^2
T_X (a.u.)
DW
KC
0.1
0.2
0.3
0.4
0.5
0.6
0.7
0.8
0.9
1.0
c

FIG. 13D

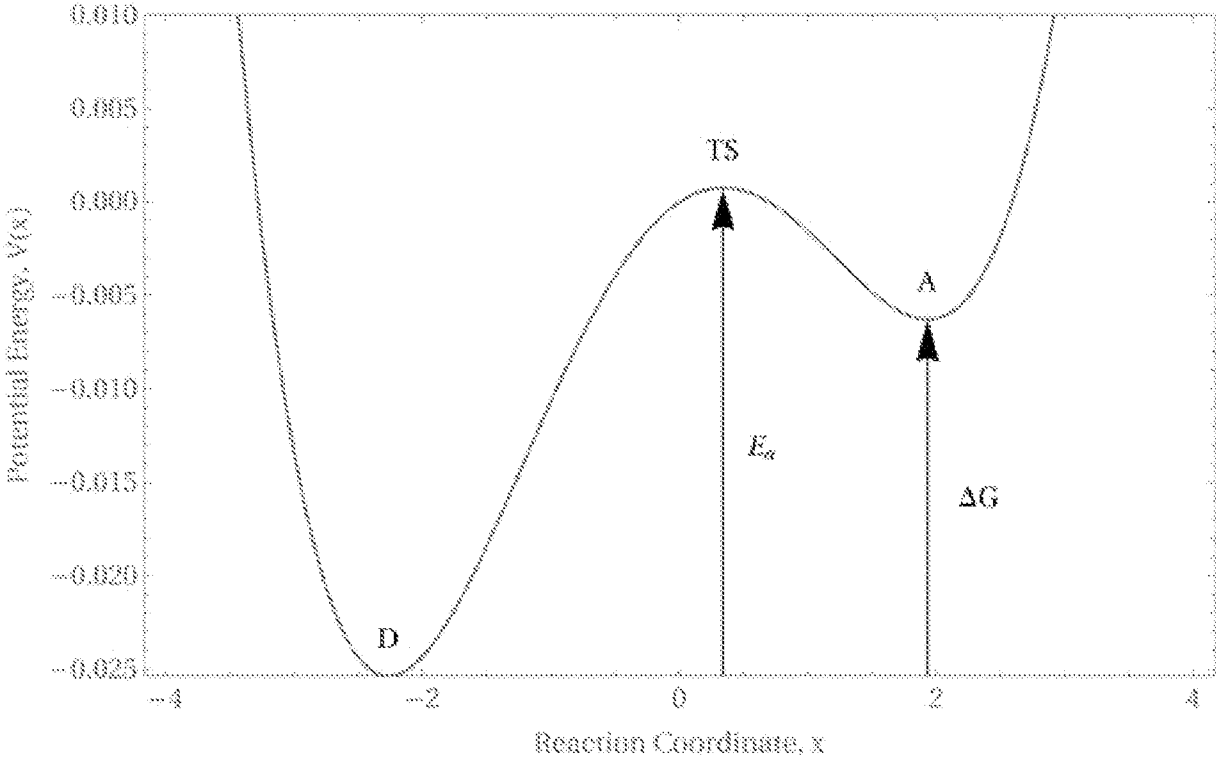
0.010
0.005
0.000
−0.005
−0.010
−0.015
−0.020
−0.025
Potential Energy, V(x)
TS
A
D
E_a
ΔG
−4
−2
0
2
4
Reaction Coordinate, x

FIG. 14

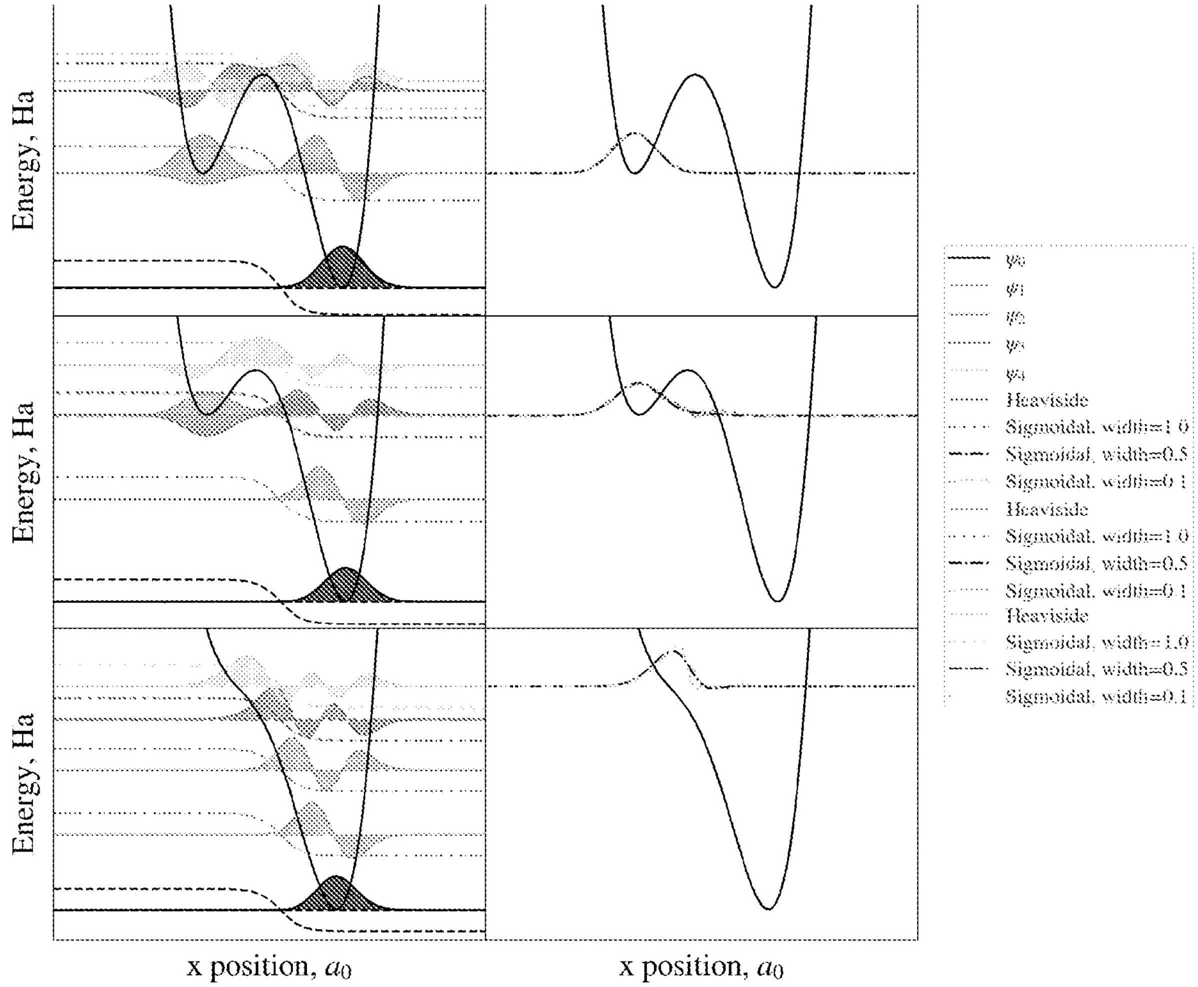
Energy, Ha
Energy, Ha
Energy, Ha
x position, a_0
x position, a_0
ψ_0
ψ_1
ψ_2
ψ_3
ψ_4
Heaviside
Sigmoidal, width=1.0
Sigmoidal, width=0.5
Sigmoidal, width=0.1
Heaviside
Sigmoidal, width=1.0
Sigmoidal, width=0.5
Sigmoidal, width=0.1
Heaviside
Sigmoidal, width=1.0
Sigmoidal, width=0.5
Sigmoidal, width=0.1

FIG. 15

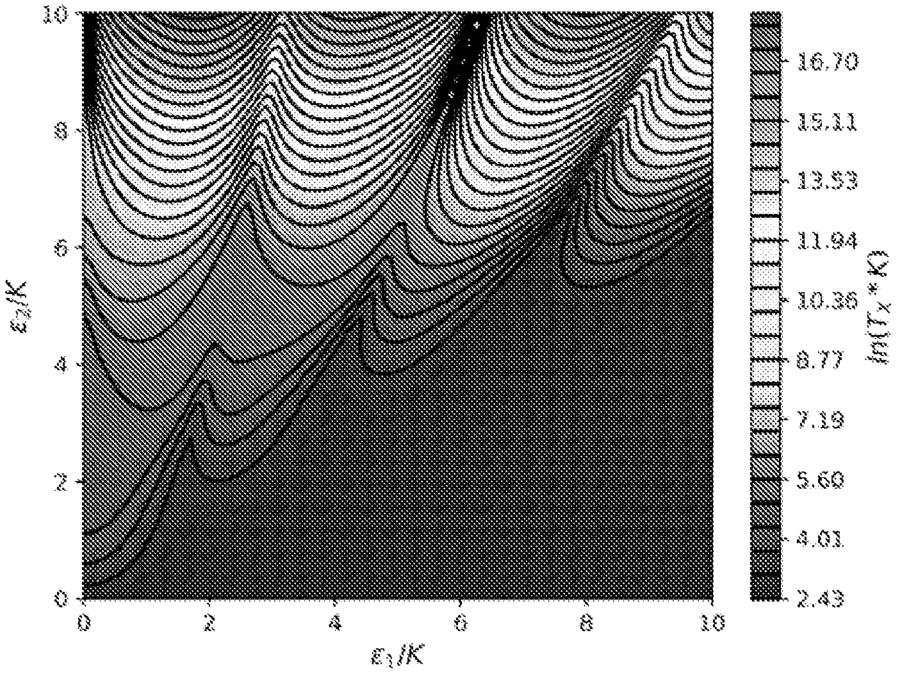

FIG. 16A

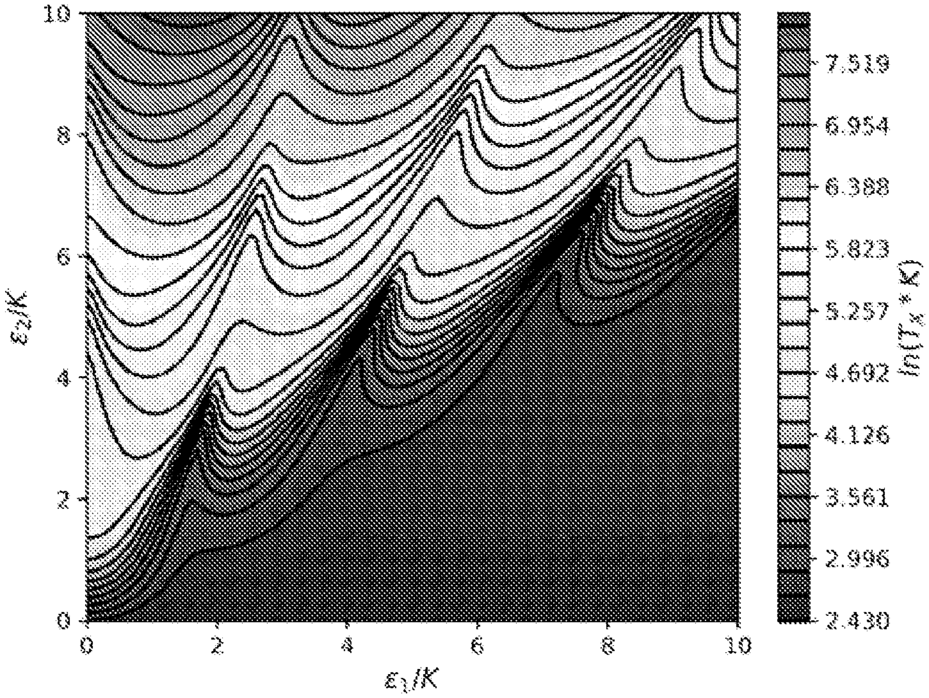

FIG. 16B

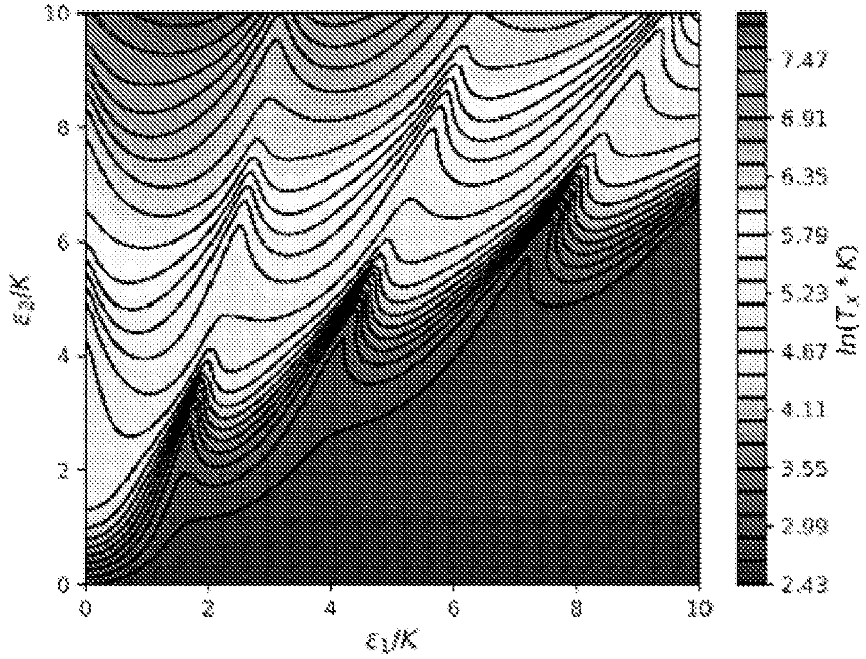

FIG. 16C

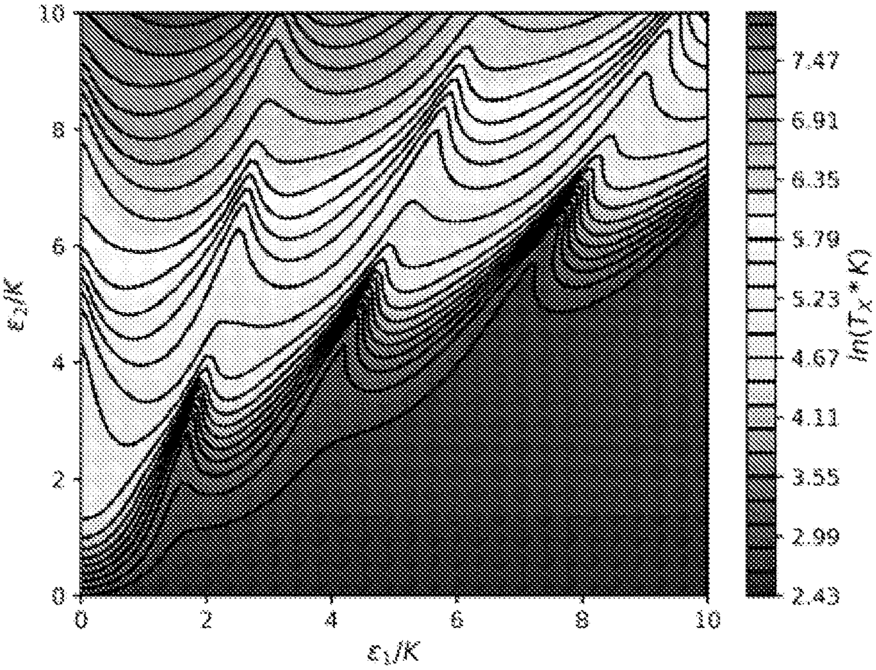

FIG. 16D

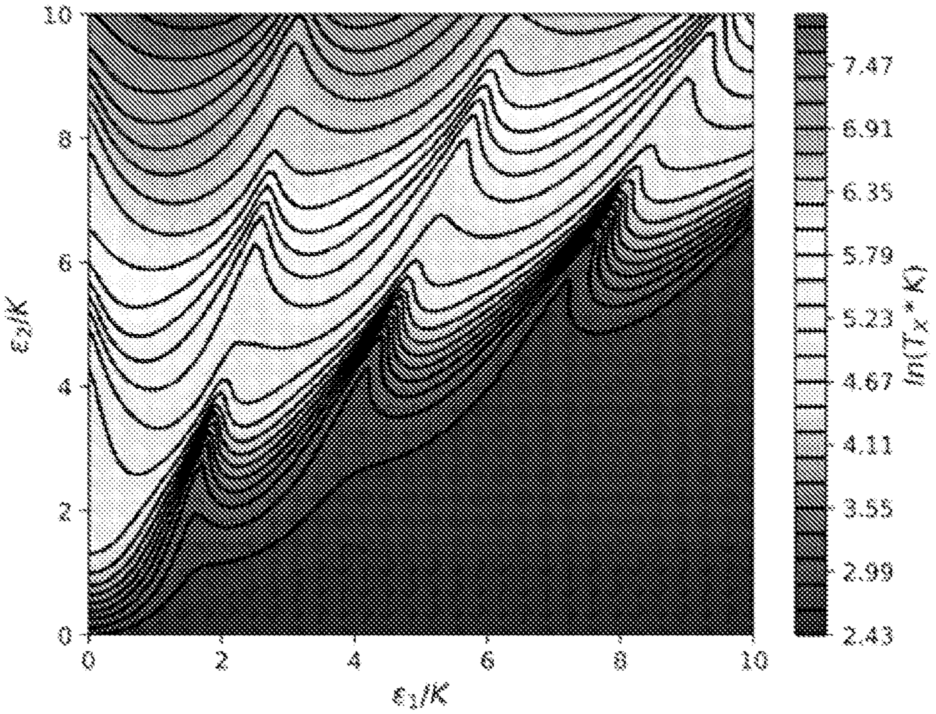

FIG. 17A

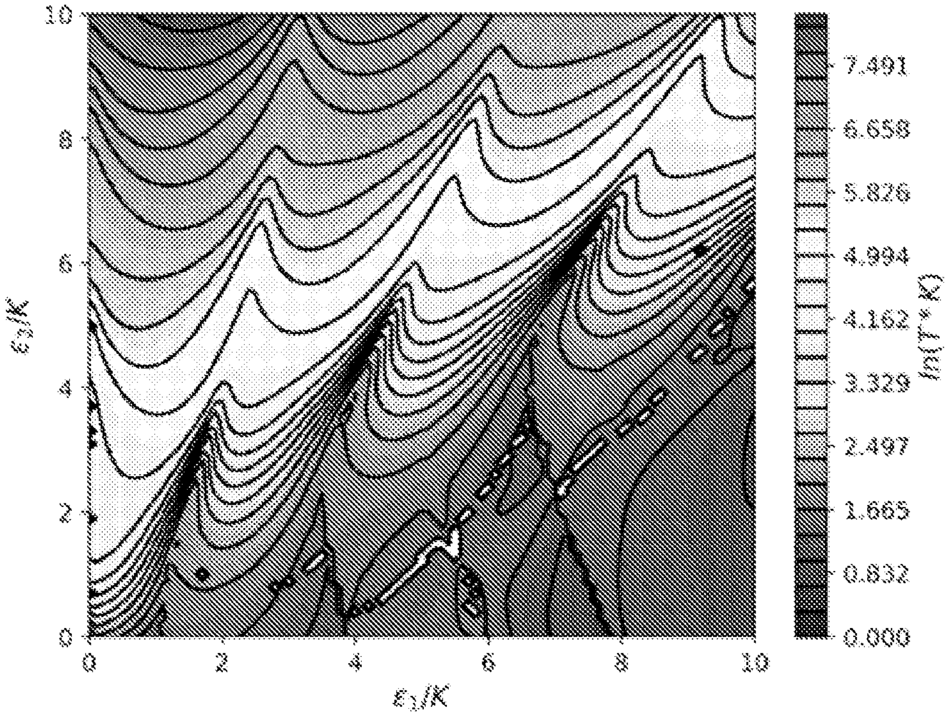

FIG. 17B

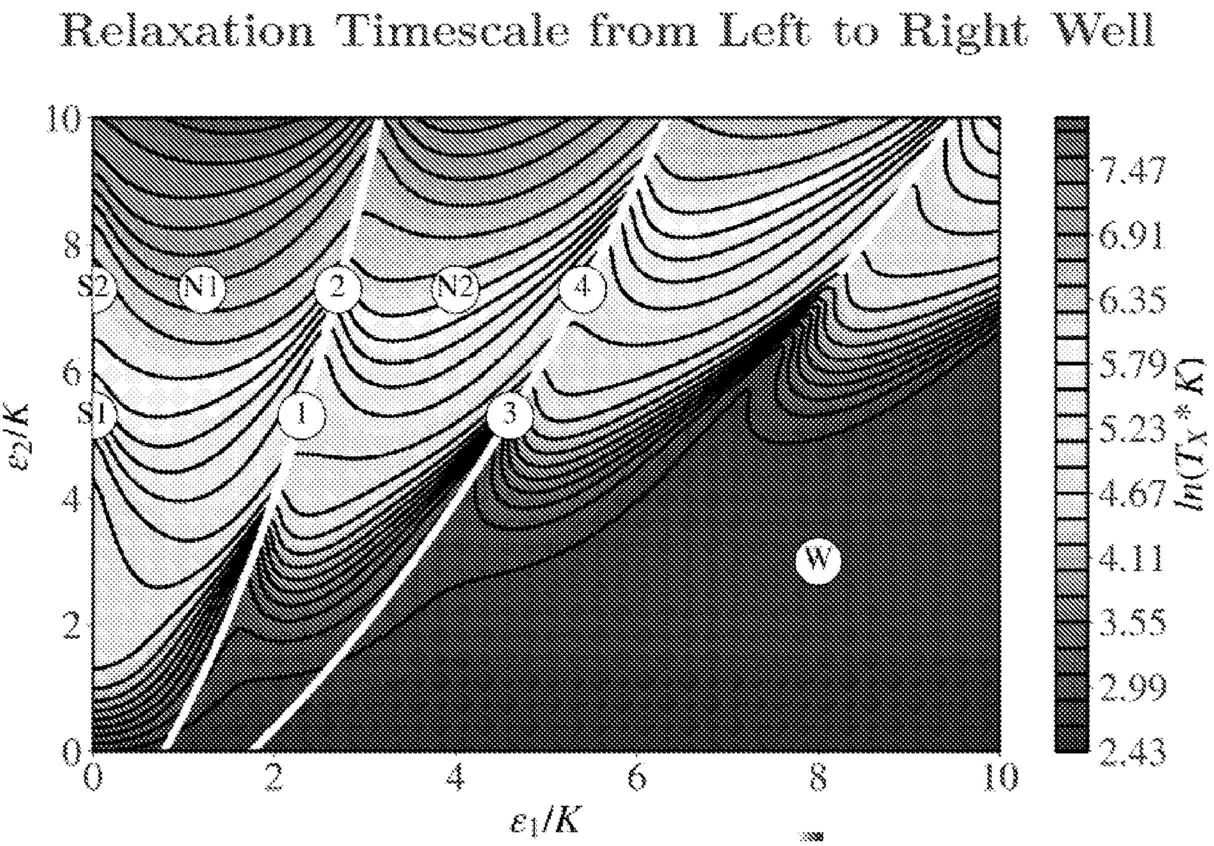
Relaxation Timescale from Left to Right Well
10
8
6
4
2
0
0
2
4
6
8
10
ε_2/K
ε_1/K
S2
N1
2
N2
4
S1
1
3
W
7.47
6.91
6.35
5.79
5.23
4.67
4.11
3.55
2.99
2.43
$ln(T_X * K)$

FIG. 18A

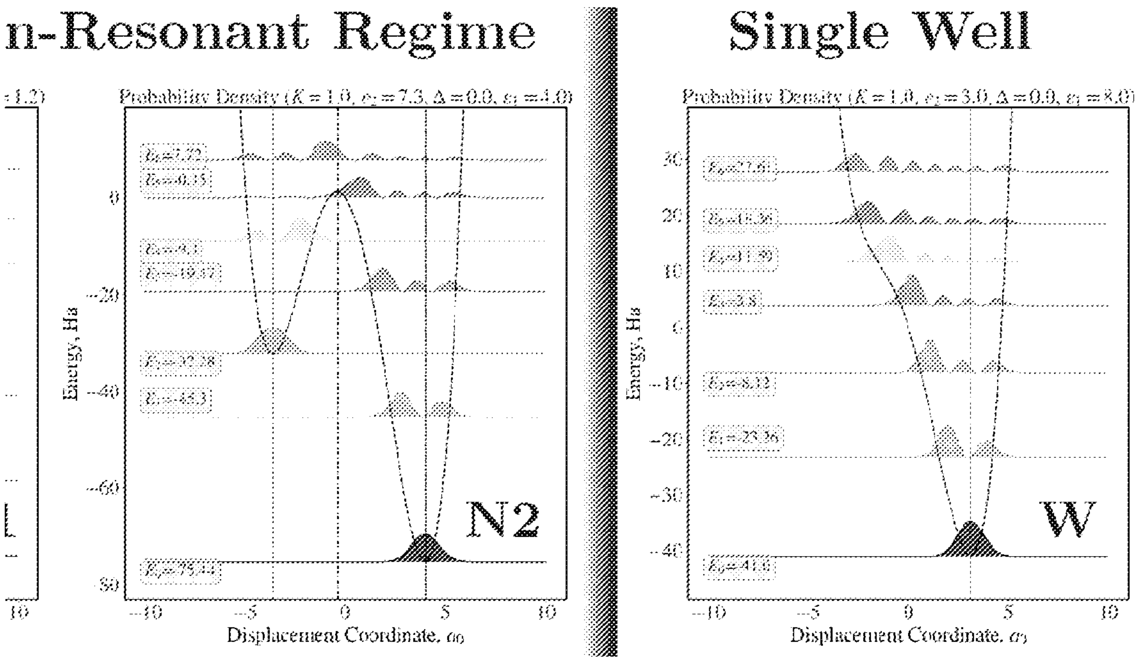
n-Resonant Regime
Single Well
Probability Density ($K = 1.0$, $e_2 = 7.3$, $\Delta = 0.0$, $s_1 = 4.0$)
Probability Density ($K = 1.0$, $e_2 = 3.0$, $\Delta = 0.0$, $s_1 = 8.0$)
$E=7.72$
$E=0.35$
$E=-8.1$
$E=-19.37$
$E=-32.28$
$E=-45.3$
$E=-75.44$
$E=27.6$
$E=18.36$
$E=11.59$
$E=3.8$
$E=-8.12$
$E_1=-23.26$
$E_0=-41.6$
N2
W
Energy, Ha
0
−20
−40
−60
−80
30
20
10
0
−10
−20
−30
−40
−10
−5
0
5
10
Displacement Coordinate, α_0
Displacement Coordinate, α_3

FIG. 18B

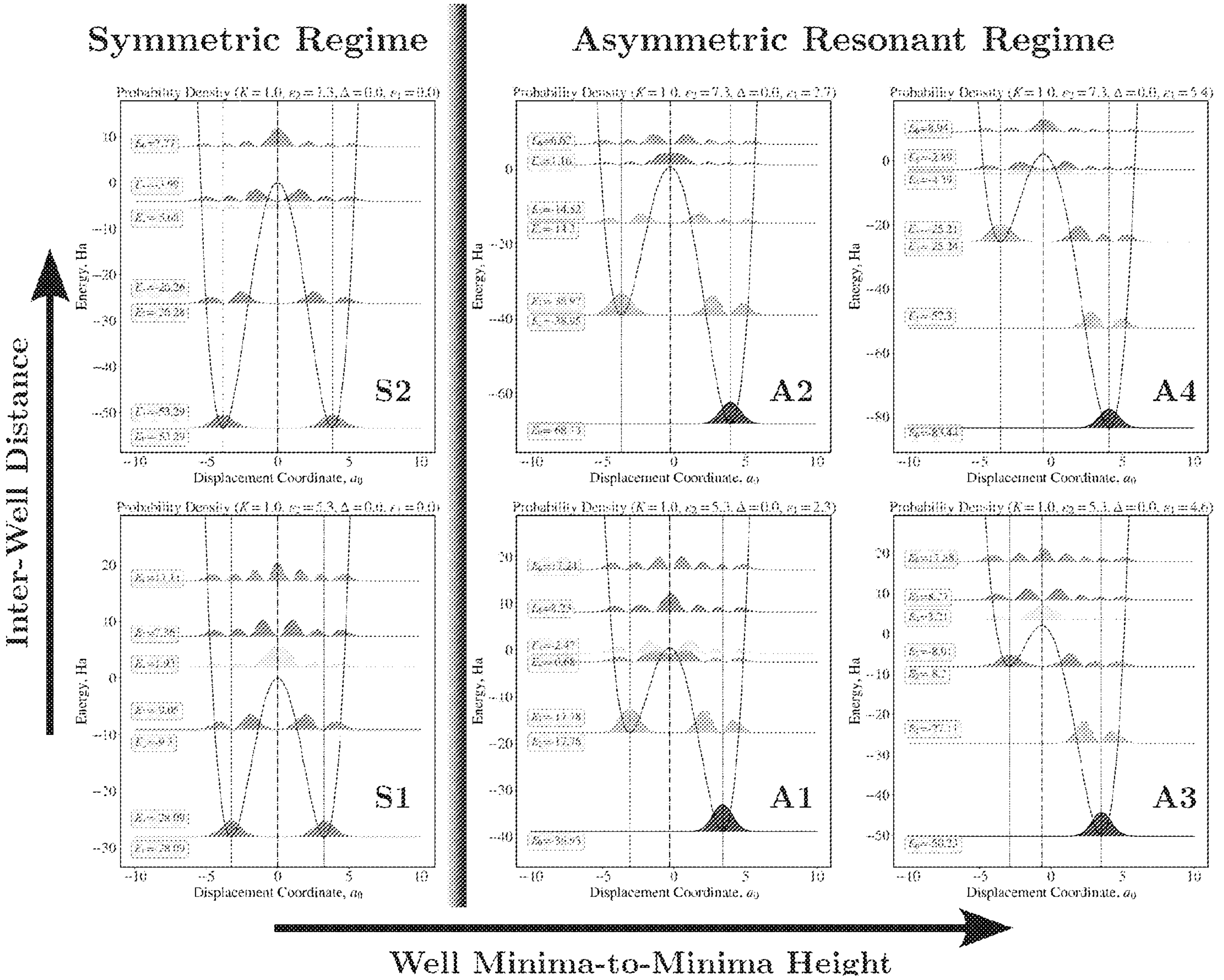
Symmetric Regime
Asymmetric Resonant Regime
Inter-Well Distance
Well Minima-to-Minima Height
Probability Density ($K = 1.0$, $\varepsilon_2 = 7.3$, $\Delta = 0.0$, $\varepsilon_1 = 0.0$)
S2
Probability Density ($K = 1.0$, $\varepsilon_2 = 7.3$, $\Delta = 0.0$, $\varepsilon_1 = 2.7$)
A2
Probability Density ($K = 1.0$, $\varepsilon_2 = 7.3$, $\Delta = 0.0$, $\varepsilon_1 = 5.4$)
A4
Probability Density ($K = 1.0$, $\varepsilon_2 = 5.3$, $\Delta = 0.0$, $\varepsilon_1 = 0.0$)
S1
Probability Density ($K = 1.0$, $\varepsilon_2 = 5.3$, $\Delta = 0.0$, $\varepsilon_1 = 2.3$)
A1
Probability Density ($K = 1.0$, $\varepsilon_2 = 5.3$, $\Delta = 0.0$, $\varepsilon_1 = 4.6$)
A3
Energy, Ha
Displacement Coordinate, a_0
-10
-5
0
5
10

FIG. 18C

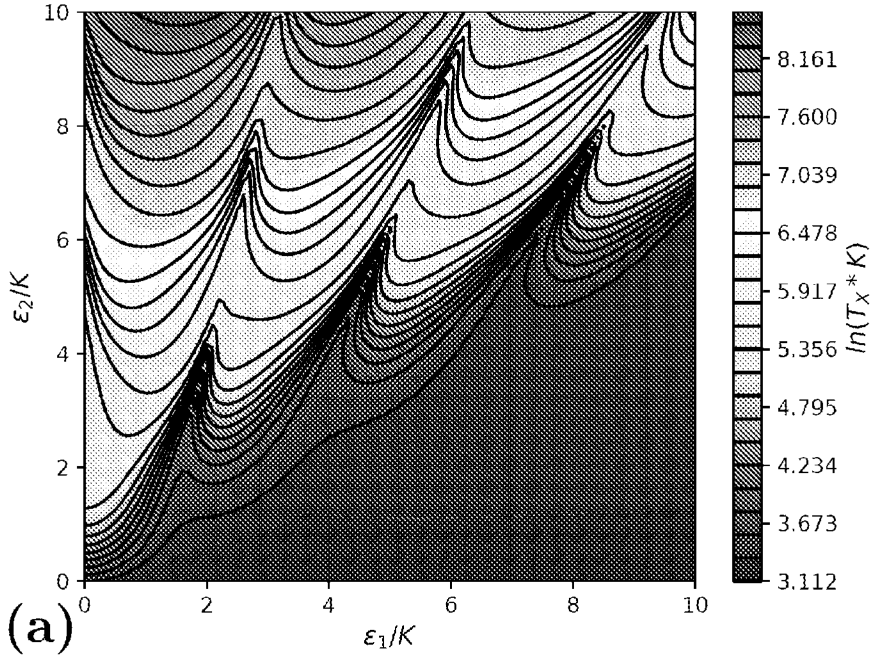

FIG. 19A

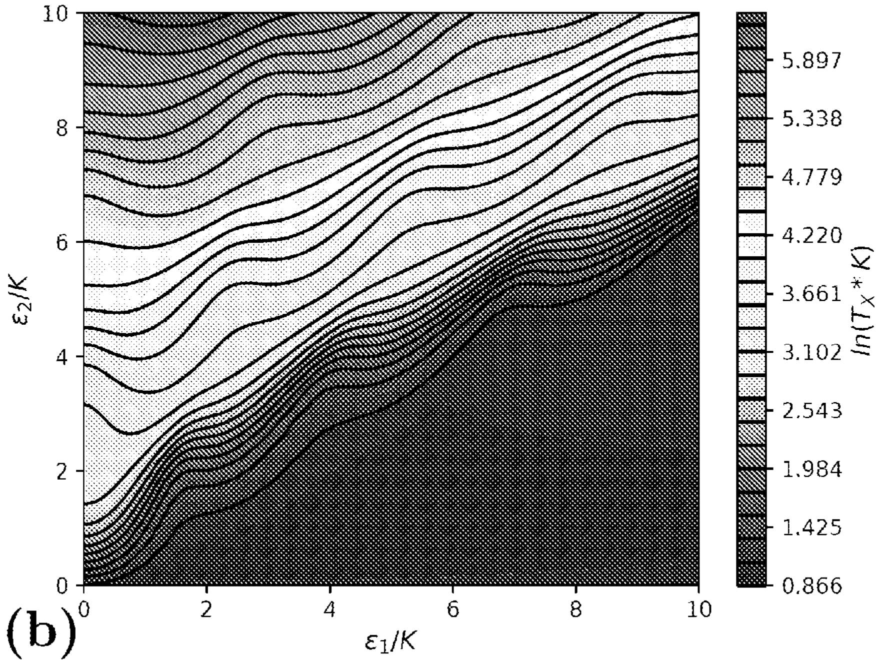

FIG. 19B

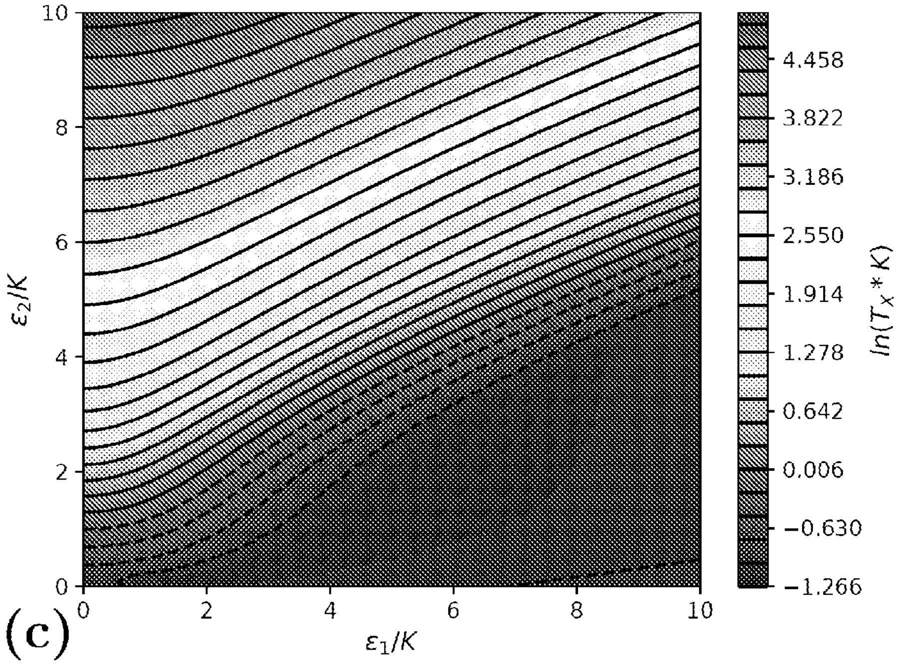
10
8
6
4
2
0
ε_2/K
0
2
4
6
8
10
ε_1/K
(c)
4.458
3.822
3.186
2.550
1.914
1.278
0.642
0.006
−0.630
−1.266
$ln(T_x * K)$

FIG. 19C

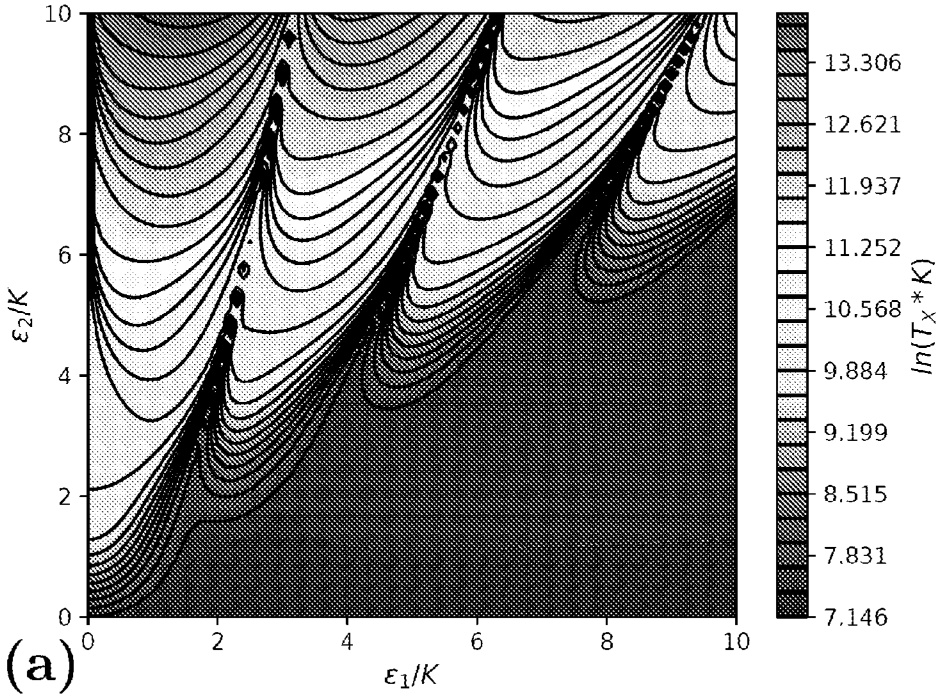

FIG. 20A

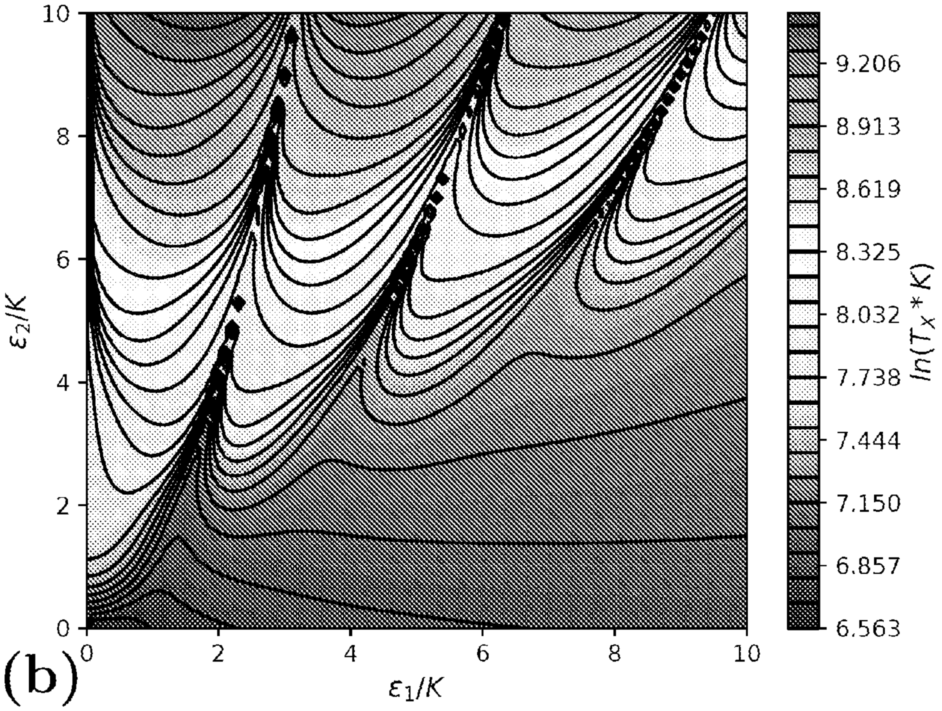

FIG. 20B

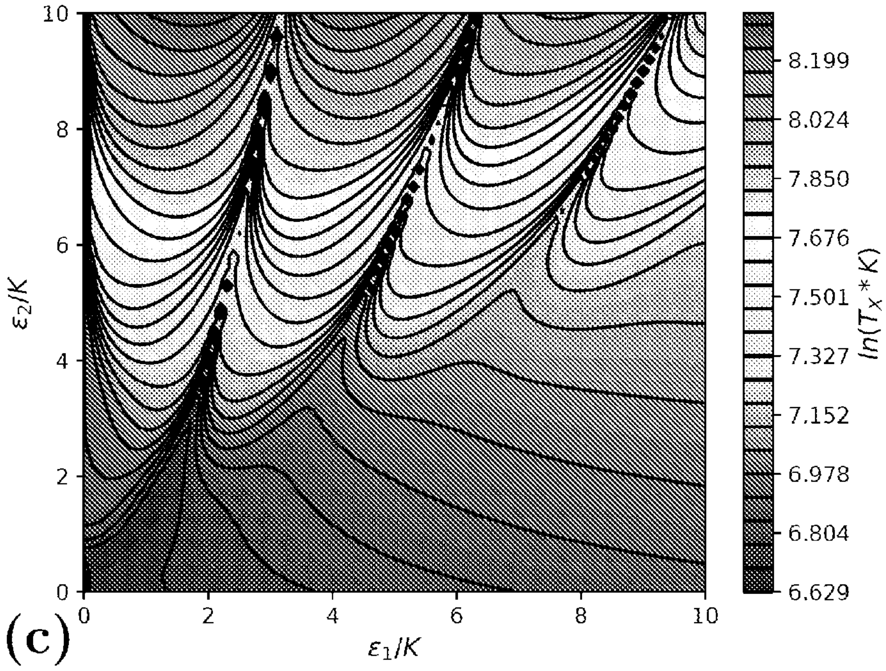
10
8
6
4
2
0
ε_2/K
0
2
4
6
8
10
ε_1/K
(c)
8.199
8.024
7.850
7.676
7.501
7.327
7.152
6.978
6.804
6.629
$ln(T_x * K)$

FIG. 20C

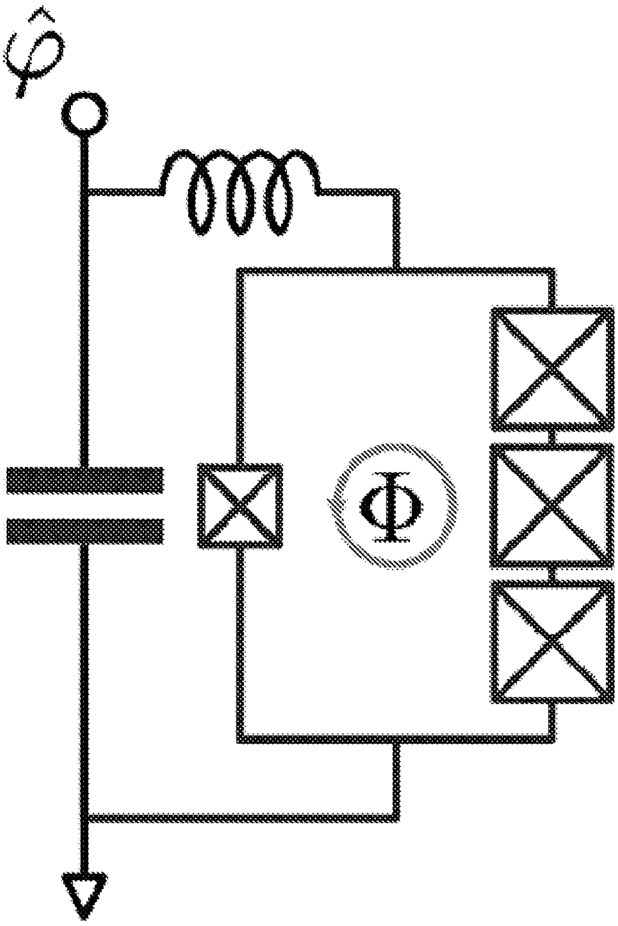

FIG. 21A

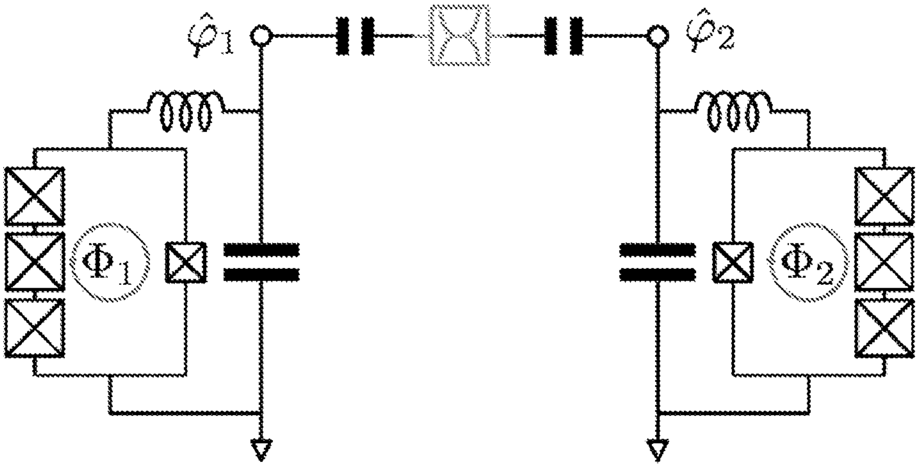

FIG. 21B

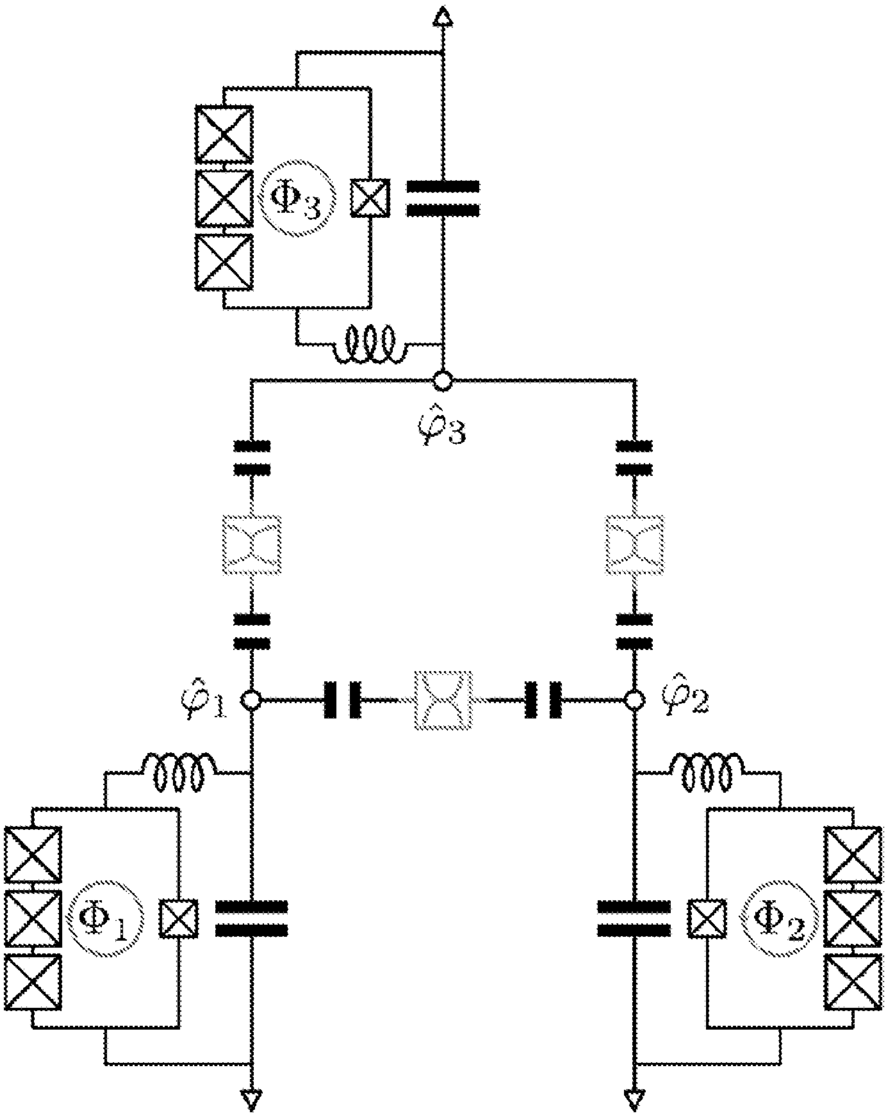

FIG. 21C

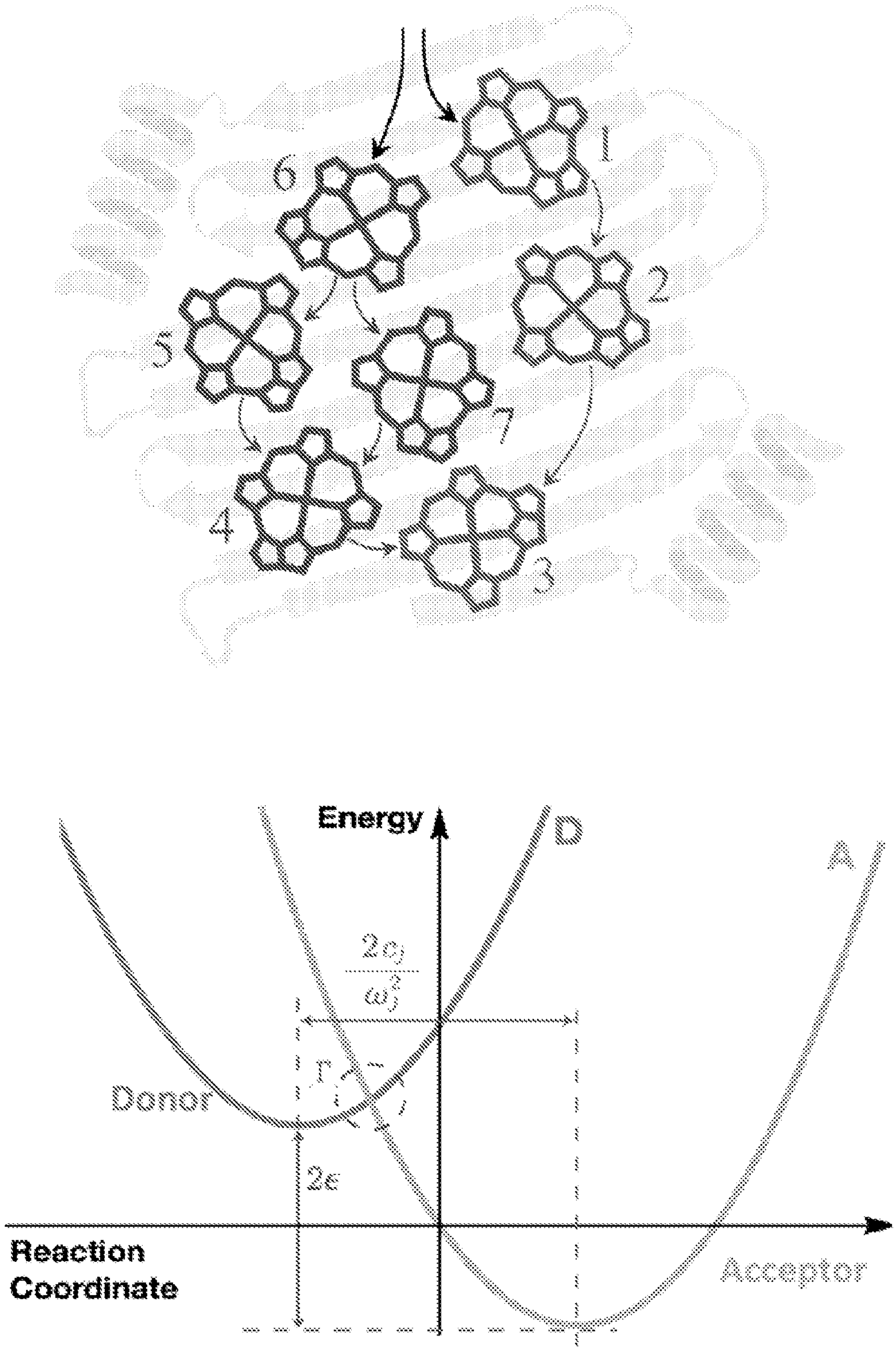
1
2
3
4
5
6
7
Energy
D
A
$\frac{2c_j}{\omega_j^2}$
Γ
Donor
2ε
Reaction Coordinate
Acceptor

FIG. 22

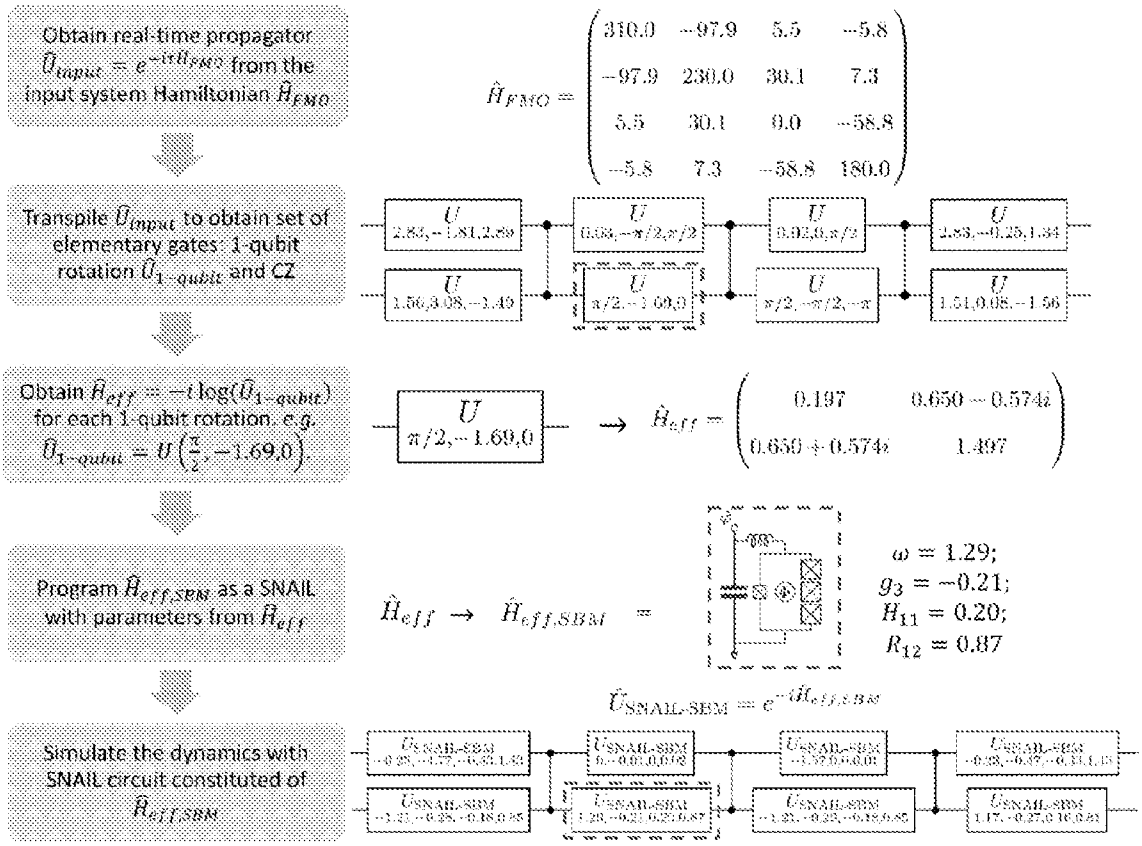
Obtain real-time propagator $\hat{U}_{input} = e^{-it\hat{H}_{FMO}}$ from the input system Hamiltonian $\hat{H}_{FMO}$
$\hat{H}_{FMO} = \begin{pmatrix} 310.0 & -97.9 & 5.5 & -5.8 \\ -97.9 & 230.0 & 30.1 & 7.3 \\ 5.5 & 30.1 & 0.0 & -58.8 \\ -5.8 & 7.3 & -58.8 & 180.0 \end{pmatrix}$
Transpile $\hat{U}_{input}$ to obtain set of elementary gates: 1-qubit rotation $\hat{U}_{1-qubit}$ and CZ
U 2.83, −1.81, 2.89
U 0.08, −π/2, π/2
U 0.02, 0, π/2
U 2.83, −0.25, 1.34
U 1.56, 3.08, −1.49
U π/2, −1.69, 0
U π/2, −π/2, −π
U 1.51, 0.08, −1.56
Obtain $\hat{H}_{eff} = -i\log(\hat{U}_{1-qubit})$ for each 1-qubit rotation, e.g. $\hat{U}_{1-qubit} = U\left(\frac{\pi}{2}, -1.69, 0\right)$.
U π/2, −1.69, 0
$\longrightarrow \hat{H}_{eff} = \begin{pmatrix} 0.197 & 0.650 - 0.574i \\ 0.650 + 0.574i & 1.497 \end{pmatrix}$
Program $\hat{H}_{eff,SBM}$ as a SNAIL with parameters from $\hat{H}_{eff}$
$\hat{H}_{eff} \rightarrow \hat{H}_{eff,SBM} =$
$\omega = 1.29;$
$g_3 = -0.21;$
$R_{11} = 0.20;$
$R_{12} = 0.87$
$\hat{U}_{\mathrm{SNAIL\text{-}SBM}} = e^{-i\hat{H}_{eff,SBM}}$
Simulate the dynamics with SNAIL circuit constituted of $\hat{H}_{eff,SBM}$
$U_{\mathrm{SNAIL\text{-}SBM}}$
$U_{\mathrm{SNAIL\text{-}SBM}}$
$U_{\mathrm{SNAIL\text{-}SBM}}$
$U_{\mathrm{SNAIL\text{-}SBM}}$
$U_{\mathrm{SNAIL\text{-}SBM}}$ −1.21, −0.28, −0.18, 0.85
$U_{\mathrm{SNAIL\text{-}SBM}}$
$U_{\mathrm{SNAIL\text{-}SBM}}$
$U_{\mathrm{SNAIL\text{-}SBM}}$ 1.17, −0.27, 0.16, 0.81

FIG. 23

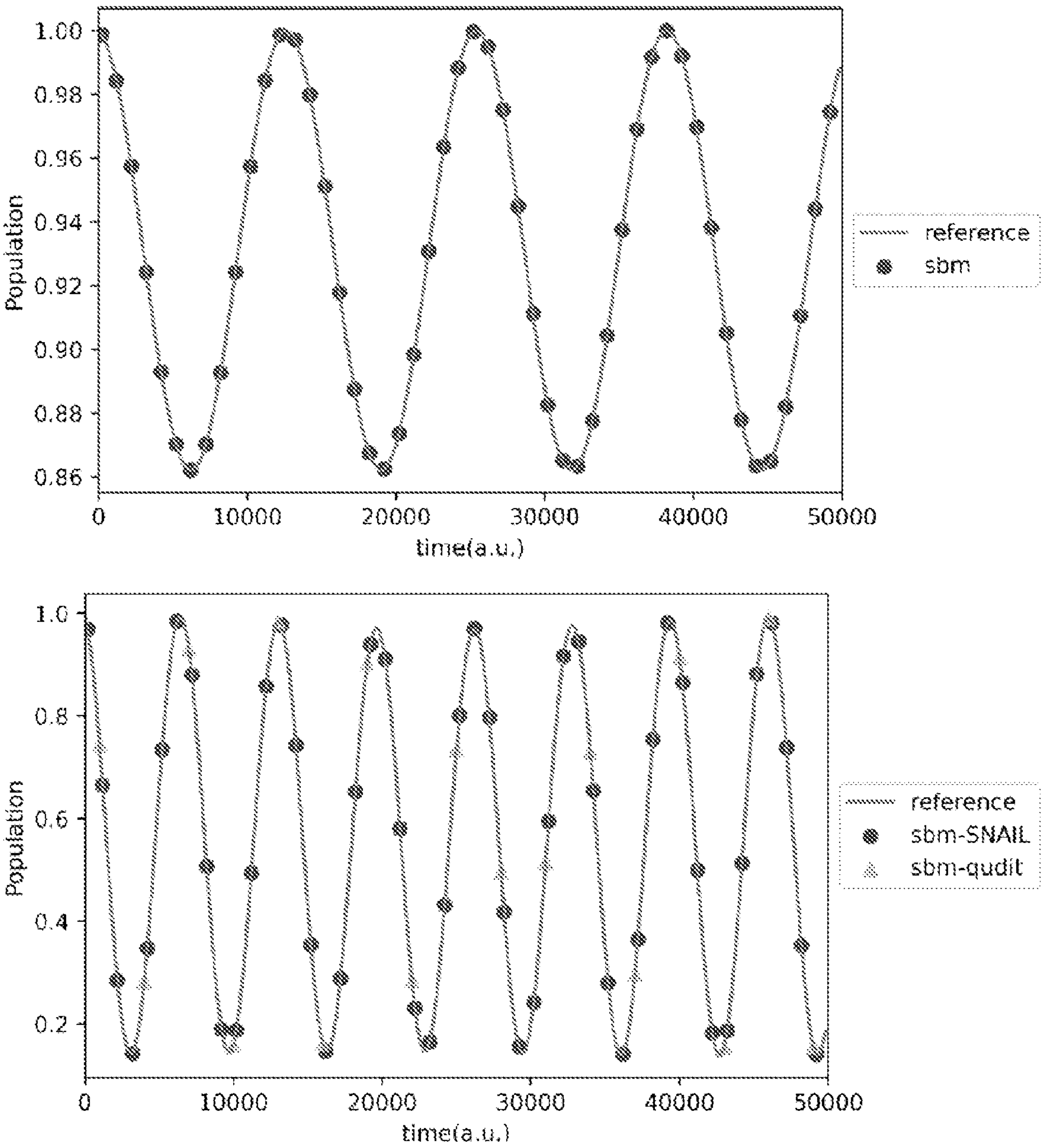
Population
1.00
0.98
0.96
0.94
0.92
0.90
0.88
0.86
0
10000
20000
30000
40000
50000
time(a.u.)
reference
sbm
Population
1.0
0.8
0.6
0.4
0.2
0
10000
20000
30000
40000
50000
time(a.u.)
reference
sbm-SNAIL
sbm-qudit

FIG. 24

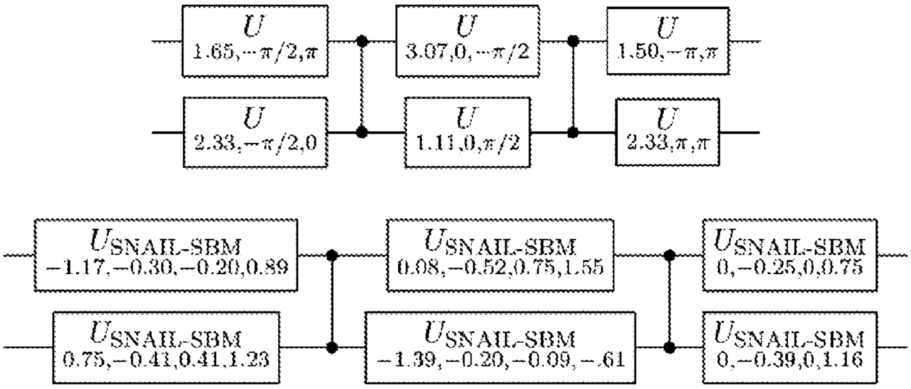
U 1.65, −π/2, π
U 3.07, 0, −π/2
U 1.50, −π, π
U 2.33, −π/2, 0
U 1.11, 0, π/2
U 2.33, π, π
$U_{\text{SNAIL-SBM}}$ −1.17, −0.30, −0.20, 0.89
$U_{\text{SNAIL-SBM}}$ 0.08, −0.52, 0.75, 1.55
$U_{\text{SNAIL-SBM}}$ 0, −0.25, 0, 0.75
$U_{\text{SNAIL-SBM}}$ 0.75, −0.41, 0.41, 1.23
$U_{\text{SNAIL-SBM}}$ −1.39, −0.20, −0.09, −.61
$U_{\text{SNAIL-SBM}}$ 0, −0.39, 0, 1.16

FIG. 25

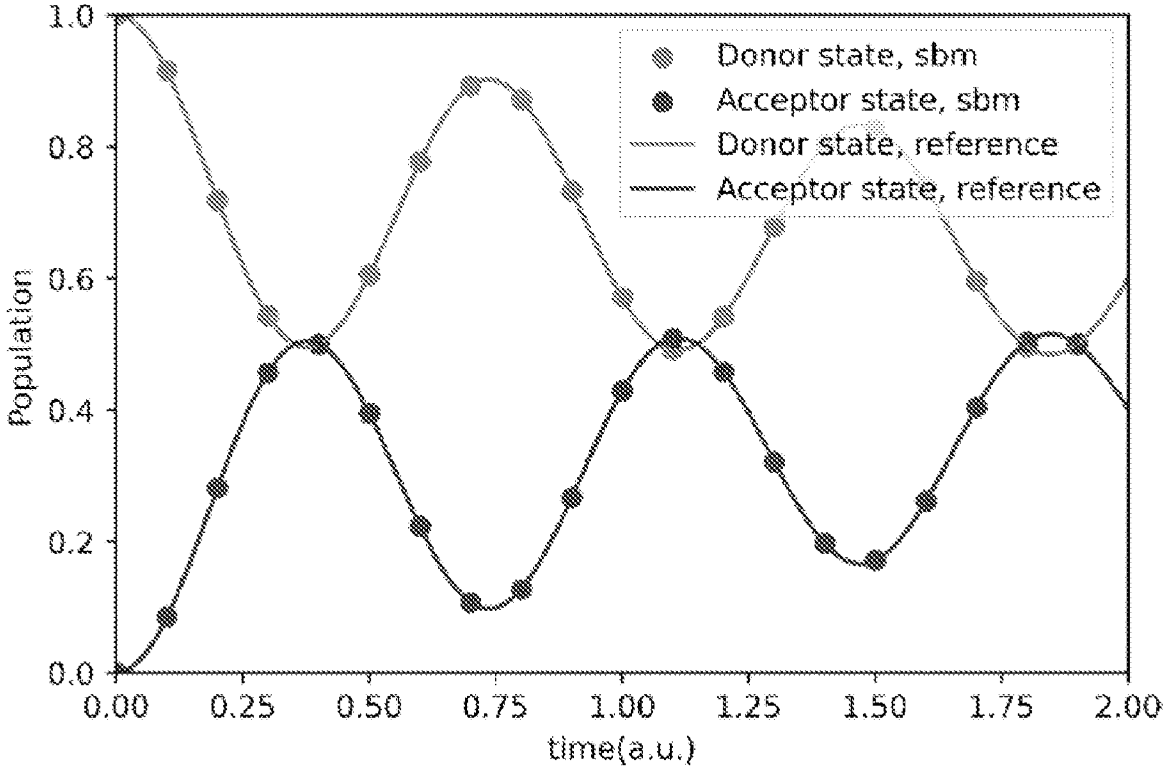
Donor state, sbm
Acceptor state, sbm
Donor state, reference
Acceptor state, reference
Population
1.0
0.8
0.6
0.4
0.2
0.0
0.00
0.25
0.50
0.75
1.00
1.25
1.50
1.75
2.00
time(a.u.)

FIG. 26

INTERNATIONAL SEARCH REPORT

International application No.
PCT/US2025/038342

A. CLASSIFICATION OF SUBJECT MATTER

IPC: ***G06N 10/40*** (2025.01); *B82Y 10/00* (2025.01); *G06N 10/20* (2025.01)
CPC: ***G06N 10/40;*** *B82Y 10/00; G06N 10/20*

According to International Patent Classification (IPC) or to both national classification and IPC

B. FIELDS SEARCHED

Minimum documentation searched (classification system followed by classification symbols)

See Search History Document

Documentation searched other than minimum documentation to the extent that such documents are included in the fields searched

See Search History Document

Electronic data base consulted during the international search (name of data base and, where practicable, search terms used)

See Search History Document

C. DOCUMENTS CONSIDERED TO BE RELEVANT

Category*	Citation of document, with indication, where appropriate, of the relevant passages	Relevant to claim No.
A	US 2004/0165454 A1 (AMIN et al.) 26 August 2004 (26.08.2004) Fig 2, 3, abstract, para [0079]-[0094]	1-27
A	WO 2023/175071 A1 (C12 QUANTUM ELECTRONICS) 21 September 2023 (21.09.2023) Fig 1-4, abstract	1-27
A	US 2017/0104493 A1 (KABUSHIKI KAISHA TOSHIBA) 13 April 2017 (13.04.2017) abstract	1-27
A	WO 2024/054272 A1 (YALE UNIVERSITY) 14 March 2024 (14.03.2024) abstract, para [0005], [0082]	1-27
X, P	CARRILLO DE ALBORNOZ, et al. Oscillatory dissipative tunneling in an asymmetric double-well potential. arXiv: 2409.13113v1 [quant-ph] [online], 19 September 2024 (19.09.2024) [retrieved on 2025-09-02]. Retrieved from the Internet: <URL: https://arxiv.org/abs/2409.13113> <DOI: 10.48550/arXiv.2409.13113>. Fig 1, 2, abstract	1-27

☐ Further documents are listed in the continuation of Box C. ☐ See patent family annex.

*	Special categories of cited documents:	"T"	later document published after the international filing date or priority date and not in conflict with the application but cited to understand the principle or theory underlying the invention
"A"	document defining the general state of the art which is not considered to be of particular relevance	"X"	document of particular relevance; the claimed invention cannot be considered novel or cannot be considered to involve an inventive step when the document is taken alone
"D"	document cited by the applicant in the international application	"Y"	document of particular relevance; the claimed invention cannot be considered to involve an inventive step when the document is combined with one or more other such documents, such combination being obvious to a person skilled in the art
"E"	earlier application or patent but published on or after the international filing date	"&"	document member of the same patent family
"L"	document which may throw doubts on priority claim(s) or which is cited to establish the publication date of another citation or other special reason (as specified)		
"O"	document referring to an oral disclosure, use, exhibition or other means		
"P"	document published prior to the international filing date but later than the priority date claimed		

Date of the actual completion of the international search **02 September 2025 (02.09.2025)**	Date of mailing of the international search report **10 September 2025 (10.09.2025)**
Name and mailing address of the ISA/US **COMMISSIONER FOR PATENTS** **MAIL STOP PCT, ATTN: ISA/US** **P.O. Box 1450** **Alexandria, VA 22313-1450** **UNITED STATES OF AMERICA** Facsimile No. **571-273-8300**	Authorized officer **HARRY KIM** Telephone No. **PCT Help Desk: 571-272-4300**